

# PE&RS

February 2020

Volume 86, Number 2

PHOTOGRAMMETRIC ENGINEERING & REMOTE SENSING The official journal for imaging and geospatial information science and technology



# GEO WEEK 2020

Washington, DC | March 23-25, 2020  
<http://conferences.asprs.org/geoweek-2020/>

## WORKSHOP ANNOUNCEMENT

March 23, 2019

### **Streamlined Photorealistic Textured Mesh and True Orthophoto Generation from Aerial Imagery**

*Thomas Widmer, Trimble and Mohsen Miri, Trimble*

Highly accurate 3D meshes provide virtual navigation of real-world environments in desktop and web platforms. These products are used in city modeling, construction and simulation purposes. Modeling of 3D surfaces with sharp edges and high quality textured meshes can be performed in a modern and precise methods. These meshes can be used to produce true orthophotos, simplifying planimetric mapping and the overlay of other GIS data, especially in urban mapping applications. This workshop will explore the methods used to create these products using Trimble INPHO MATCH-3DX software.

### **Digital Aerial Triangulation using Imagery from Multi-Head Systems**

*Mohsen Miri, Trimble and Thomas Widmer, Trimble*

Current aerial mapping technologies lead to capturing a large number of images, not only at nadir but also in oblique viewing directions. The number and variety of multi-head oblique platforms available on the market is continuously growing. This workshop presents a stable and simplified workflow for the complex multi-head imagery for higher production efficiencies. This workshop will explore the workflow and the matching strategies for such systems using Trimble INPHO MATCH-AT software.

### **Best Practices for Managing, Editing, Visualizing, and Sharing Lidar in 2D and 3D**

*Nicholas Giner, Esri and Lindsay Weitz, Esri*

Although lidar data has been collected and processed for over 20 years, the global lidar market continues to rapidly expand as demand for 3D imagery in consumer, commercial, and government applications increases. Federal, state, and local government agencies are acquiring lidar data for use in applications such as floodplain mapping, urban planning and design, resource and environmental management, law enforcement, natural resource exploration, archeology, and emergency response. This session will teach best practices for working with Light Detection and Ranging (lidar) data. Attendees of this session will learn lidar basics and fundamentals, as well as the best practices for managing, editing, visualizing, and sharing it in 2D and 3D. Attendees will also learn several workflows for deriving useful information products from lidar data, as well as performing 2D and 3D analysis on lidar-derived products.

### **Using USGS/ASPRS Data Quality Measure (DM) Software for Validation of Airborne Lidar Point Clouds**

*Barry Miller, USGS and Ajit Sampath, USGS*

This workshop provides an in-depth look at the USGS/ASPRS Data Quality Measure (DQM) software. DQM provides an ability to determine the relative accuracy, or geometric quality, of overlapping swaths of lidar point clouds using a point-to-plane measurement technique. DQM calculates vertical and horizontal differences between swaths in a point cloud tile, which allows better analysis of the quality of a lidar project. Attendees will see a demonstration on how to use the tool and interpret the results with several real-world examples. The workshop will also show how to obtain the software, which is a government-furnished freeware for public use.

### **UAS Lidar for Precision Mapping**

*Mohamed Mostafa, Microdrones Canada Inc.*

Professional grade lidar systems are currently being used onboard unmanned aerial systems for high precision mapping applications. This workshop is intended for the unmanned airborne lidar user community including mapping professionals, land surveyors, managers, and decision makers to understand the underlying concepts of lidar from the technical and business perspective, in the form of theory and practice, using real data sets from around the world.

### **Fundamentals of Image Analysis in Google Earth Engine**

*Ge (Jeff) Pu, SUNY-ESF*

Cloud-based image processing platforms like the Google Earth Engine (GEE) bring unprecedented possibilities for education, research, and outreach. This workshop will focus on an interactive exploration of GEE capabilities, the repository of all of publicly available aerial and satellite data, and user upload of imagery for analysis. The workshop will begin with a presentation of examples of GEE projects with a focus on education, undergraduate research, and outreach followed by hands-activities.

### **Preparation for ASPRS Certification – Lidar**

*Karen Schuckman, Penn State University*

This workshop provides an in-depth review of content contained in the ASPRS Airborne Topographic Lidar Manual. It is valuable for those planning to take the examination for ASPRS Certified Mapping Scientist-Lidar, Certified Technologist-Lidar, or Intern. Workshop participants will answer practice questions and discuss answers in an interactive session. The workshop is also valuable for practitioners wishing to further their mastery of the theory and practice of topographic mapping with lidar.

### **Practical Approach to Using the ASPRS Positional Accuracy Standards for Digital Geospatial Data**

*Qassim Abdullah, Woolpert, Inc. and*

*Claire Kiedrowski, Cornerstone Energy Services, Inc.*

This workshop provides an in-depth look at the ASPRS Positional Accuracy Standards to categorize positional accuracy of products derived from digital aerial cameras, manned and unmanned aerial systems, and all types of lidar including terrestrial, mobile, and airborne. The workshop will explain the basis for each accuracy measure adopted in the standards. Instructors will demonstrate practical application of these standards. Attendees will apply these standards to real-world examples.

## Object Based Image Analysis Made Easy and Flexible

*Keith Peterson, Trimble, and*

*Jarlath O'Neil-Dunne, University of Vermont*

This workshop will provide an informative introduction to the fundamental concepts and technologies in object-based image analysis and its combination with computer vision methods, machine-learning and pixel-based operations. Attendees will use eCognition Developer to employ a comprehensive range of analysis tools utilizing diverse data sources, from medium to high resolution satellite data, very high-resolution aerial and UAV imagery, GIS, lidar, radar, and even hyperspectral data.

## Combining Deep Learning with Object Based Image Analysis (OBIA)

*Keith Peterson, Trimble, and Christian Weise, Trimble*

Recently, deep learning (DL) has become the fastest growing trend in data analysis and has been widely and successfully applied to various feature extraction tasks. In the context of remote sensing the combination of DL with OBIA (object-based image analysis) offers the flexibility to select the optimal working method inside the complete feature extraction workflow. This workshop will explore the accelerated usage of deep learning with object-based image analysis using Trimble eCognition Developer software.

## Spreadsheet Demonstration of Analytical Photogrammetry

*Paul Pope, Global Geoinformatics Inc.*

Photogrammetry is often explained by describing the collinearity condition and showing examples of final products. The intermediate steps are rarely illustrated in detail. This workshop aims to make analytical photogrammetry accessible to the layperson by using spreadsheet calculations to 1) solve for the exterior orientation parameters of a framing camera, and 2) determine the dimensions of an object using stereo imagery.

## Generic Sensor Models for Photogrammetric Applications

*Henry Theiss, Integrity Applications Incorporated*

The workshop conveys the importance of rigorous sensor modeling, data adjustment, and covariance propagation in meeting the absolute geolocation, relative mensuration, and multi-sensor fusion objectives of the end-user. It proceeds with an overview of the Community Sensor Model (CSM) Application Programming Interface (API) which facilitates integration of multi-modality imagery and point-cloud products into geospatial exploitation tools. It provides an overview of generic sensor models for frame-sequences, linear-array scanners, SAR, and lidar.”

## Total Propagated Uncertainty (TPU) and Absolute Accuracy Assessment of 3D Lidar Point Cloud

*Minsu Kim, USGS*

Total Propagated Uncertainty (TPU) is the statistical estimate of lidar positional uncertainty for each lidar point. Theoretical details of the TPU and its application to the airborne lidar data will be presented. Assessment of the 3D absolute accuracy of the lidar point cloud is an important priority in USGS 3DEP program. TPU is an important factor that affects the absolute accuracy of the lidar point cloud data. Techniques for the 3D absolute accuracy assessment using various geometric features and its inherent relationship with TPU will be discussed in the workshop.

## Machine and Deep Learning Image Classification

*Amr Abd-Elrahman, University of Florida*

This workshop teaches participants how to (1) conduct pixel- and object-based image classification using traditional (Support Vector Machine and Random Forests) machine learning algorithms; (2) build models for data preparation and experiment with different classification parameters; (3) use the deeplab deep learning architecture for image segmentation (classification). Participants will be briefly introduced to necessary theoretical background information as well as practical implementation using ArcGIS Pro. Real world examples of wetland land cover classification will be used in the demonstration.

## Preparation for ASPRS Certification

### - General Knowledge

*Robert Burtch, Ferris State University*

This workshop covers the common knowledge areas comprising a large portion of exam content for ASPRS Certification. It is valuable preparation for those who have never taken an ASPRS exam, as well as for those who have expertise in a particular specialty, such as lidar or UAS, but feel less prepared for the general knowledge component of the exam. This workshop will also explain the certification application process and the importance of certification in career development.

## Aerial Triangulation and Data Processing for the Unmanned Aerial System (UAS)

*Qassim A Abdullah, Woolpert, Inc. and*

*Riadh Munjy, CSU Fresno*

This workshop teaches participants to successfully design, plan and execute an aerial mission using unmanned aerial systems (UAS) and GPS-based aerial triangulation, including flight planning, ground control placement, camera calibration, and product generation. Participants will be introduced to mathematical basis of simultaneous bundle block adjustment. Practical examples will be presented.

## REGISTER FOR WORKSHOPS ON THE CONFERENCE REGISTRATION SITE!

If you have already registered for the conference and wish to add a workshop, call 508-743-8501.

If you wish to register for a workshop without registering for the conference, call 508-743-8501.

For additional information, see

<http://conferences.asprs.org/geoweek-2020/> or contact [programs@asprs.org](mailto:programs@asprs.org)



To have your press release published in *PE&RS*, contact Rae Kelley, [rkelly@asprs.org](mailto:rkelly@asprs.org).

## ANNOUNCEMENT

Dewberry has been selected by the Louisiana Department of Transportation & Development (DOTD) to provide consulting services related to the acquisition and processing of lidar and photogrammetric data to support the development of a statewide geospatial database for topographic mapping.

Dewberry will assist with collecting, processing, management, and distribution of lidar and photogrammetric data acquired with DOTD's aircraft, digital camera, and lidar sensor. An on-site Dewberry team will provide continuous training and technical support for acquisition planning, sensor operation, GIS data processing, lidar classification, and lidar-derived products for all elements under the contract.

Dewberry will also assist with updates to the Master Program Management Plan to provide DOTD with the ability to:

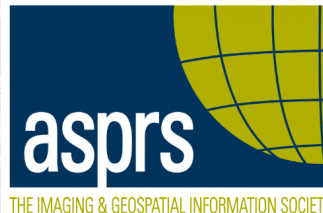
- Develop and maintain a statewide geospatial database for topographic mapping with the assistance of other state agencies and departments
- Address the creation, structuring, and manipulation of a functional database
- Adopt a plan for the management and distribution of data to other local, state, and federal agencies as well as private entities

The geospatial data will be used for the management of resources and operations throughout the state. Dewberry will also create quality assurance/quality control protocols for future collection and processing; and assist in the planning and implementation of data storage, backup, archiving, and maintenance on a server or through a cloud service.

## CALENDAR

- 16-18 March, **RSCy2020**, Paphos, Cyprus. For more information, visit: [www.cyprusremotesensing.com/rscy2020/](http://www.cyprusremotesensing.com/rscy2020/)
- 23-25 March, **Geo Week**, Washington, DC. For more information, visit <https://www.lidarmap.org/geoweek/>.
- 7-9 May, **GISTAM 2020—6th International Conference on Geographical Information Systems Theory, Applications and Management**, Prague, Czech Republic. For more information, visit: [www.gistam.org/](http://www.gistam.org/).
- 20-22 May, **AutoCarto 2020**, Redlands, California. For more information, visit <https://cartogis.org/autocarto/>.
- 15-22 August, **43<sup>rd</sup> COSPAR Scientific Assembly**, Sydney, Australia. For more information, visit [www.cospar-assembly.org/](http://www.cospar-assembly.org/).

[HTTP://DPAC.ASPRS.ORG](http://dpac.asprs.org)



*“The ASPRS Aerial Data Catalog is a tool allowing owners of aerial photography to list details and contact information about individual collections. By providing this free and open metadata catalog with no commercial interests, the Data Preservation and Archiving Committee (DPAC) aims to provide a definitive metadata resource for all users in the geospatial community to locate previously unknown imagery.”*

# ASPRS AERIAL DATA CATALOG

“THE SOURCE FOR FINDING AERIAL COLLECTIONS”

**1**  
**USE**

Use the catalog to browse over 5,000 entries from all 50 states and many countries. Millions of frames from as early as 1924!

**2**  
**SUPPLY**

Caretakers of collections with, or without metadata, should contact DPAC to add their datasets to the catalog for free!

**3**  
**TELL**

Spread the word about the catalog! New users and data collections are key to making this a useful tool for the community!

## For More Details Contact:

David Ruiz  
[druiz@quantumspatial.com](mailto:druiz@quantumspatial.com)  
510-834-2001

David Day  
[dday@kasurveys.com](mailto:dday@kasurveys.com)  
215-677-3119



## 73 In Interview—Corey Ochsman, ASPRS Rising Star Program Benefactor

### PEER-REVIEWED ARTICLES

#### 91 Using Ranked Probability Skill Score (RPSS) as Nonlocal Root-Mean-Square Errors (RMSEs) for Mitigating Wet Bias of Soil Moisture Ocean Salinity (SMOS) Soil Moisture

Ju Hyoung Lee

To mitigate instantaneously evolving biases in satellite retrievals, a stochastic approach is applied over West Africa. This stochastic approach independently self-corrects Soil Moisture Ocean Salinity (SMOS) wet biases.

#### 99 Economy Estimation of Mainland China at County-Level Based on Landsat Images and Multi-Task Deep Learning Framework

Bo Yu, Ying Dong, Fang Chen, and Yu Wang

The social-economic statistics collected from local governments are the main access for the central government to achieve national economic circumstance, especially for China. However, the statistics of almost 10% of national counties are missing or inconsistent due to the statistical caliber change in the wave of urbanization during economic development. In this paper, the publicly available daytime Landsat images are used to estimate economic statistics.

#### 107 Multi-Spatial Resolution Satellite and sUAS Imagery for Precision Agriculture on Smallholder Farms in Malawi

Brad G. Peter, Joseph P. Messina, Jon W. Carroll, Junjun Zhi, Vimbayi Chimonyo, Shengpan Lin, and Sieglinde S. Snapp

A collection of spectral indices, derived from a range of remote sensing imagery spatial resolutions, are compared to on-farm measurements of maize chlorophyll content and yield at two trial farms in central Malawi to evaluate what spatial resolutions are most effective for relating multispectral images with crop status.

Wuyong Tao, Xianghong Hua, Ruisheng Wang, and Dong Xu

Owing to poor descriptiveness, weak robustness, and high computation complexity of local shape descriptors (LSDs), point-cloud registration in the case of partial overlap and object recognition in a cluttered environment are still challenging tasks. For this purpose, an LSD is developed in this article by proposing a new local reference frame (LRF) method and designing a novel feature representation.



## 81 Preview of the *Manual of Remote Sensing 4<sup>th</sup> Ed.*

### COLUMNS

- 75 GIS Tips & Tricks
- 77 Book Review – *Signals and Images: Advances and Results in Speech, Estimation, Compression, Recognition, Filtering, and Processing*

### ANNOUNCEMENTS

- 69 Geo Week 2020 — ASPRS Workshops Announced
- 78 Certification
- 79 Headquarters News
- 80 New ASPRS Members  
Join us in welcoming our newest members to ASPRS.
- 98 *PE&RS* Call for Submissions— Optical Polarization Remote Sensing & Photogrammetry

### DEPARTMENTS

- 70 Industry News
- 70 Calendar
- 106 Who's Who in ASPRS
- 120 ASPRS Sustaining Members

See the Cover Description on Page 72

# COVER DESCRIPTION



On January 9, 2020, the Operational Land Imager (OLI) on Landsat 8 acquired natural-color observations of burned land and thick smoke covering Australia's Kangaroo Island. According to news reports, at least 156,000 hectares (600 square miles, nearly one-third of the land area) have burned and 50 homes have been destroyed on the island of 4,700 people.

To view the full image, visit <https://landsat.visibleearth.nasa.gov/view.php?id=146132>.

NASA Earth Observatory images by Lauren Dauphin, using Landsat data from the U.S. Geological Survey. Caption by Mike Carlowicz.

## Be a part of ASPRS Social Media:

 [facebook.com/ASPRS.org](https://facebook.com/ASPRS.org)

 [linkedin.com/groups/2745128/profile](https://linkedin.com/groups/2745128/profile)

 [twitter.com/ASPRSorg](https://twitter.com/ASPRSorg)

 [youtube.com/user/ASPRS](https://youtube.com/user/ASPRS)



THE IMAGING  
& GEOSPATIAL  
INFORMATION  
SOCIETY

## PHOTOGRAMMETRIC ENGINEERING & REMOTE SENSING

### JOURNAL STAFF

Publisher ASPRS  
Editor-In-Chief Alper Yilmaz  
Assistant Editor Jie Shan  
Assistant Director — Publications Rae Kelley  
Electronic Publications Manager/Graphic Artist  
Matthew Austin

*Photogrammetric Engineering & Remote Sensing* is the official journal of the American Society for Photogrammetry and Remote Sensing. It is devoted to the exchange of ideas and information about the applications of photogrammetry, remote sensing, and geographic information systems. The technical activities of the Society are conducted through the following Technical Divisions: Geographic Information Systems, Photogrammetric Applications, Lidar, Primary Data Acquisition, Professional Practice, and Remote Sensing Applications. Additional information on the functioning of the Technical Divisions and the Society can be found in the Yearbook issue of *PE&RS*.

Correspondence relating to all business and editorial matters pertaining to this and other Society publications should be directed to the American Society for Photogrammetry and Remote Sensing, 425 Barlow Place, Suite 210, Bethesda, Maryland 20814-2144, including inquiries, memberships, back issues, changes in address, manuscripts for publication, advertising, subscription, and publications. The telephone number of the Society Headquarters is 301-493-0290; the fax number is 225-408-4422; web address is [www.asprs.org](http://www.asprs.org).

**PE&RS.** *PE&RS* (ISSN0099-1112) is published monthly by the American Society for Photogrammetry and Remote Sensing, 425 Barlow Place, Suite 210, Bethesda, Maryland 20814-2144. Periodicals postage paid at Bethesda, Maryland and at additional mailing offices.

**SUBSCRIPTION.** For the 2020 subscription year, ASPRS is offering two options to our *PE&RS* subscribers — an e-Subscription and the print edition. E-subscribers can plus-up their subscriptions with printed copies for a small additional charge. Print and Electronic subscriptions are on a calendar-year basis that runs from January through December. We recommend that customers who choose both e-Subscription and print (e-Subscription + Print) renew on a calendar-year basis.

The rate of the e-Subscription (digital) Site License Only for USA and Non-USA is \$1000.00 USD. e-Subscription (digital) Site License Only for Canada\* is \$1049.00 USD. e-Subscription (digital) Plus Print for USA is \$1365.00 USD. e-Subscription (digital) Plus Print for Canada\* is \$1424.00 USD. e-Subscription (digital) Plus Print for Non-USA is \$1395.00 USD. Printed-Subscription Only for USA is \$1065.00 USD. Printed-Subscription Only for Canada\* is \$1124.00 USD. Printed-Subscription Only for Non-USA is \$1195.00 USD. \*Note: e-Subscription/Printed-Subscription Only/e-Subscription Plus Print for Canada include 5% of the total amount for Canada's Goods and Services Tax (GST #135123065). **PLEASE NOTE: All Subscription Agencies receive a 20.00 USD discount.**

**POSTMASTER.** Send address changes to *PE&RS*, ASPRS Headquarters, 425 Barlow Place, Suite 210, Bethesda, Maryland 20814-2144. CDN CPM #40020812

**MEMBERSHIP.** Membership is open to any person actively engaged in the practice of photogrammetry, photointerpretation, remote sensing and geographic information systems; or who by means of education or profession is interested in the application or development of these arts and sciences. Membership is for one year, with renewal based on the anniversary date of the month joined. Membership Dues include a 12-month electronic subscription to *PE&RS*. Or you can receive the print copy of *PE&RS* Journal which is available to all member types for an additional fee of \$60.00 USD for shipping USA, \$65.00 USD for Canada, or \$75.00 USD for international shipping. Dues for ASPRS Members outside of the U.S. will now be the same as for members residing in the U.S. Annual dues for Regular members (Active Member) is \$150.00 USD; for Student members \$50.00 USD for USA and Canada \$58.00 USD; \$60.00 USD for Other Foreign members. A tax of 5% for Canada's Goods and Service Tax (GST #135123065) is applied to all members residing in Canada.

**COPYRIGHT 2020.** Copyright by the American Society for Photogrammetry and Remote Sensing. Reproduction of this issue or any part thereof (except short quotations for use in preparing technical and scientific papers) may be made only after obtaining the specific approval of the Managing Editor. The Society is not responsible for any statements made or opinions expressed in technical papers, advertisements, or other portions of this publication. Printed in the United States of America.

**PERMISSION TO PHOTOCOPY.** The appearance of the code at the bottom of the first page of an article in this journal indicates the copyright owner's consent that copies of the article may be made for personal or internal use or for the personal or internal use of specific clients. This consent is given on the condition, however, that the copier pay the stated per copy fee of 3.00 USD through the Copyright Clearance Center, Inc., 222 Rosewood Drive, Danvers, Massachusetts 01923, for copying beyond that permitted by Sections 107 or 108 of the U.S. Copyright Law. This consent does not extend to other kinds of copying, such as copying for general distribution, for advertising or promotional purposes, for creating new collective works, or for resale.

# COREY OCHSMAN



*Corey Ochsman is a benefactor of the ASPRS' Rising Star Program. He has an unique perspective on where archaeology of the past meets geospatial technologies of the future. He studied geography and art history at George Mason University and later earned a Masters in Classical Archaeology from Leiden University in the Netherlands. His focus on geospatial technology in archaeology brought him to work several seasons as the GIS manager at the excavations of the Villa di Massenzio in Rome. Since then, he has continued to work in a variety of positions at the cross section of the geospatial industry. In 2011, Corey began working with lidar and started deploying to Afghanistan with the USACE Buckeye Program. He transitioned to the Buckeye UAS platform in Jordan and worked there for several years before bringing his breadth of knowledge to Woolpert. Corey currently lives in Colorado and he spends his free time traveling, climbing mountains, and BASE jumping.*

## **Tell us about your educational background including your doctoral research, if applicable.**

I was not the best student in high school as I preferred to be outside on my dirt bike or playing baseball rather than studying. I attended George Mason University and I began my education aspiring to be a chemical engineer because I was enamored with AP Chemistry. But higher level calculus and computer science classes halted my progress and I sought a subject that would, in my mind, allow me some breathing room. I began studying geography at GMU and the major required a minor. My new-found interest in art history pushed me to minor in that subject, something a sane person would rarely do. But that is how I learned to love education and I dove head first into art history and archaeology. I discovered remote sensing just before graduating and realized that I could combine the two fields. My parents pushed graduate school on me and, as a rebellious move, I found a program in Classical Archaeology in Leiden, The Netherlands and zipped off to Europe in the summer of 2006. Living and studying abroad was one of the best experiences in my life. I look back on those years with extremely fond memories and although I was never a brain, I do miss how school made me feel empowered. I wrote my Masters thesis on early Greek and Phoenician colonization philosophies in the Mediterranean. Although my career utilizes my Geography degree, the skills I learned obtaining my Masters had undoubtedly prepared me for what was to come.

## **Do you have a particular teacher or professor who inspired your love of science? Why?**

I am thankful for Barry Haack of GMU, who instructed my first remote sensing class. He inspired me to explore the world through travel for work. Additionally, Chris Greg of GMU instructed the majority of my Greek and Roman art and archaeology classes and inspired me to enjoy learning, guided me on my first archaeological excavations, and gave me insight on life in academia.

## **What is the focus of your current research?**

My current research is focused on improving and innovating Lidar workflows. I am fortunate enough to have brilliant minds around me who are able to produce huge amounts of quality Lidar data for a multitude of customers, but there is always room for improvement. As a Team Leader, I need to always be looking forward and researching new ways for my group to improve quality and efficiency.

## **Tell us about something we might see in our daily lives that directly correlates to your work.**

Although it may not be obvious while watching news of the latest disaster relief, or the next large wildfire sweeping across Colorado, USGS 3DEP data is used for planning and mitigation purposes. According to the agency, "A core mission of the USGS is to provide information that leads to reduced loss of life and damage to property and infrastructure from hazards like landslides, earthquakes, floods, hurricanes and wildfires." My Lidar team at Woolpert processes tens of thousands of square miles of Lidar data annually that will be used in USGS's core mission.

## **Give us an example of how multi-disciplinary research directly contributed to your work.**

The production, and exploitation, of Lidar data isn't a simple process. The Lidar department alongside flight crews plan the flights based on point density and the accuracies required. Survey teams collect, control, and maintain checkpoints based on customer and project needs. At Woolpert we have select people who specialize in calibrating Lidar data. We have specialists who digitize breaklines, edit LAS file formatted information to produce accurate digital elevation models or DEMs, produce our final products, extract building footprints, generate metadata, and more. It takes a diverse team with a variety of backgrounds to make a successful project.

## When you're not working on your research, what do you do in your free time?

I firmly believe in the “work hard, play hard” motto. I take my hobbies very seriously because it is my way of decompressing from the stresses of everyday life. They allow me to think critically, problem solve and assess risk – all important life skills that can apply to work. My wife and I enjoy climbing mountains in Colorado. We have climbed all 58 of the 14,000+ foot mountains (14ers) in the state and I am currently ticking off the centennials, the highest hundred peaks. I enjoy ski mountaineering which is generally a miserable experience but emphasizes perseverance and strengthens my determination. I am a well-rounded rock climber and I focus on multi-pitch trad climbing. I do a fair bit of aid climbing as well and have climbed all of the Fisher Towers outside of Moab, Utah – a personal goal that took years to accomplish. I have been skydiving for roughly 13 years and BASE jumping (or parachuting from fixed objects) for over 10 years. That sport has its ups and downs but has taught me much about life, risk, and perspective. My typical summertime post-work decompression starts with a light dog walk and then some moderate rock climbing in one of many canyons on the front range of Colorado; and then, if the winds feel light, I might hike up the backside of a cliff and throw myself off of it.

## What advice would you give a young researcher just starting out in your field?

The only advice that I can realistically give anyone is just to enjoy life. Do what makes you happy. Have dreams. Want something bigger. Do what makes you feel good!

## What has been your most fulfilling accomplishment as a scientist / engineer? Why?

I do not know if I have a “most fulfilling” accomplishment thus far in my career, but I do have one instance of feeling like I made a difference. I worked as a cartographic technician many years ago and for months I was working on a JOG (Joint Operations Graphic) covering a portion of Pakistan. A couple months after the work was complete, and delivered to NGA, I realized the significance of a small BUA (built-up area) tint in the south east corner of the map labeled as Abbottabad.

## What do you think are the most pressing needs to be met in science in the coming years?

I believe that we need to reintroduce the scientific method to the population at large. We need to teach younger people to think critically and test their ideas before forming conclusions.



## How has being a part of the ASPRS Rising Stars Program benefited you?

Participating in the Rising Stars Program has helped integrate me into the larger geospatial industry. I've attended events and conferences during which I have met other professionals and I have gained insight on technology, operations, and issues that other firms grapple with. It has also allowed me to collaborate with other young geospatial professionals who, I believe, will be guiding the industry in just a few years. I am excited to hear their ideas and I look forward to the possibilities that will present themselves. Overall, the program has pushed my personal and professional motivation to contribute more to the industry and to be a leader.

## What books are you currently reading for pleasure?

My favorite books are non-fiction and science-based. I have read a lot of psychology and sociology books over the years because I am fascinated by the predictability of human behavior. I also love books about complex astrophysics and thus the last book I read was Neil deGrasse Tyson's *Astrophysics for People in a Hurry*. Now most of the “books” I read are project scopes. But, if I am enjoying a day at the beach, I might just crack open the USGS Lidar Base Specification.

## No Mouse needed: Keyboard Shortcuts

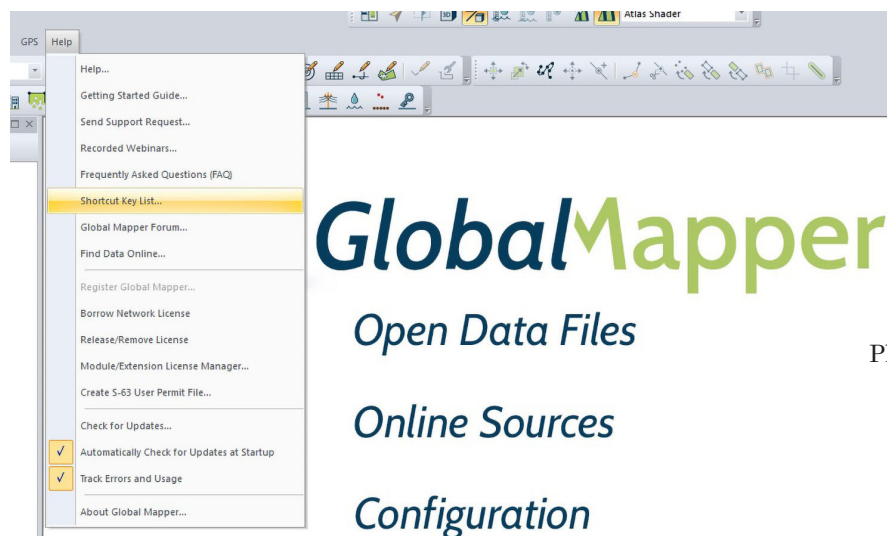
For many of us, it is hard to recall the days of desktop micro-computers before the mouse, Graphic User Interfaces, and “the Ribbon”. But now, there is now an entire generation of GIS-users who have never used a command-line interface to GIS software. However, as many of the currently used GIS packages have their roots in those pre-Windows/GUI days, many of those ancient lines of code remain in the software programs. Among the most useful tips for most GIS software packages is that many “keyboard” shortcuts are still available, if you just know where to look for them.

Prior to the ribbon, in the Microsoft™ Windows environment, some shortcuts were advertised every time you use a drop-down menu. For example, from the FILE dropdown, you could use the combination of the Control Key + the “S” key (Ctrl+S) to save your file. Similarly, from the EDIT dropdown, if you select an area on the screen and then use the Ctrl + C to COPY the selection, you can paste it elsewhere with the Ctrl+V combination. Then, of course, if you want to “undo” an edit, the Ctrl+Z combination does that. By the way, the Ctrl+Z combination still works in many programs.

The Keyboard shortcuts in GIS programs are not as obviously advertised, and sometimes difficult to find, so here are some tips.

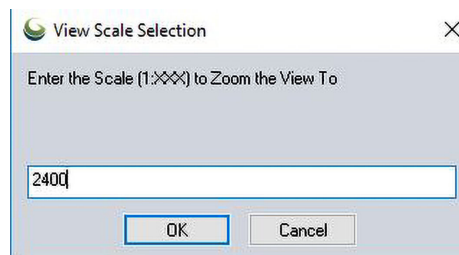
In GlobalMapper™ (v19 and above), some of the keyboard shortcuts are advertised as in pre-Ribbon Microsoft and a full list can be retrieved from the HELP dropdown.

We have three favorite GlobalMapper™ shortcuts that we use routinely when looking through Lidar data.



**Pan and Zoom**—Using the Pan and Zoom tools from the navigation toolbar or from the TOOLS dropdown always works, but these locations are sometimes inconvenient especially when you are panning around and also want to zoom-in to get a better look at a feature. The keyboard shortcuts Alt+Z (Zoom) and Alt+G (Grab and Drop) toggle between the tools. Then, if you want to return to the entire extent, just use the HOME key.

**Map Scale**—For several workflows, we will want to pan to some area of a map and then zoom to a specific map scale to uniformly evaluate features. While you could use the Zoom-in and Zoom-out tools on the Navigation Toolbar while keeping watch on the numeric display of the map scale, it is faster to zoom to the area-of-interest and use the keyboard shortcut Shift+Z to bring up a dialog box:



Type in the absolute scale you require and press <OK> to zoom to that map scale.

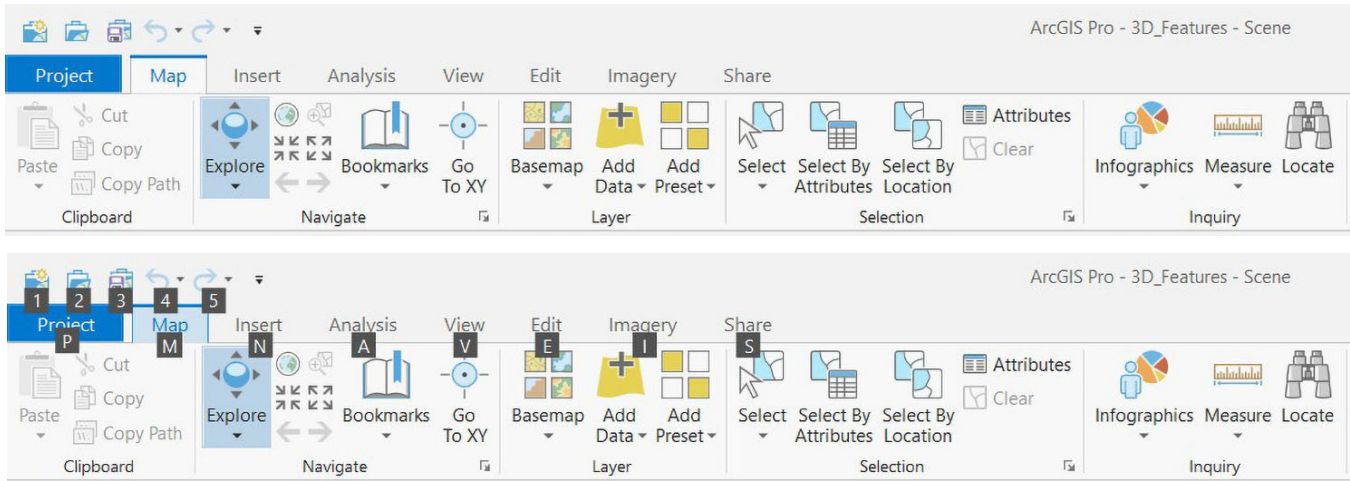
**File Management**—As with most all Microsoft™ Windows programs, the Ctrl+S will save your file (the current workspace), and Ctrl+O will open a new data file (invoke a File Explorer for you to use for navigation). However, with GlobalMapper™, the combination of Ctrl+W will open a GlobalMapper™ Workspace, and Ctrl+U will UNLOAD all loaded data files in a current map and let you start building a new workspace.

Photogrammetric Engineering & Remote Sensing  
Vol. 86, No. 2, February 2020, pp. 75–76.  
0099-1112/20/75–76

© 2020 American Society for Photogrammetry  
and Remote Sensing  
doi: 10.14358/PERS.86.2.75

Along with the “standard” Microsoft™ File Management keyboard shortcuts described above; Save File, Open Project, Copy, and Paste, Esri™ ArcGIS-Pro offers its own keyboard shortcuts. Here are a few of our favorites. You can also download a complete list of ArcGIS Pro shortcuts from <http://links.esri.com/arcgis-pro-shortcuts>.

**Toggle between windows**—For users who have fairly complex ArcGIS Pro Projects with many tabs, using the Ctrl + Tab keys together will allow you quickly toggle between all of the maps, scenes and reports in the project file. This combination of keys will also allow you to toggle between additional tabs like the Catalog, or Geoprocessing tabs.



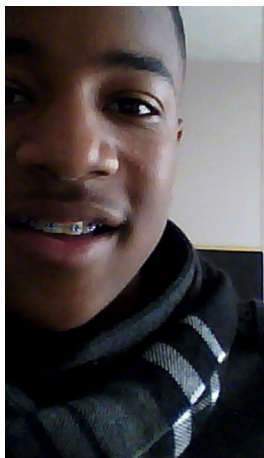
**Enable Access Keys and show the KeyTips**—As many of us start to; or continue to, make the transition from ArcMap to ArcGIS Pro, it can take a bit of time to remember exactly which hotkeys are which. The nice thing about ArcGIS Pro is that you can activate the KeyTips which will show you exactly what hotkey to use for a particular button within the ribbon. All you have to do is press ALT and you will see the KeyTip display in the ribbon just above each of the buttons.

*Al Karlin, Ph.D., CMS-L, GISP and Siddharth Pandey, CSM are with Dewberry's Geospatial and Technology Services group in Tampa, FL and Fairfax VA. As a Senior GIS Professional, Al works with all aspects of Lidar, remote sensing, photogrammetry, and GIS-related projects. Sid is a Dewberry Associate who works with all aspects of GIS development.*



The Rising Star program is focused on mentorship of tomorrow's leaders within ASPRS and the geospatial and remote sensing community. Geospatial companies, agencies, and ASPRS regions can all benefit by participation in the program through the advancement and professional development of their employees or associates through the process of sponsorship.

For more information go to [www.asprs.org/rising-star-program](http://www.asprs.org/rising-star-program).



**Too young to drive the car? Perhaps!  
But not too young to be curious about geospatial sciences.**

The ASPRS Foundation was established to advance the understanding and use of spatial data for the betterment of humankind. The Foundation provides grants, scholarships, loans and other forms of aid to individuals or organizations pursuing knowledge of imaging and geospatial information science and technology, and their applications across the scientific, governmental, and commercial sectors.

**Support the Foundation, because when he is ready so will we.**

**[asprsfoundation.org/donate](http://asprsfoundation.org/donate)**



# Bing!

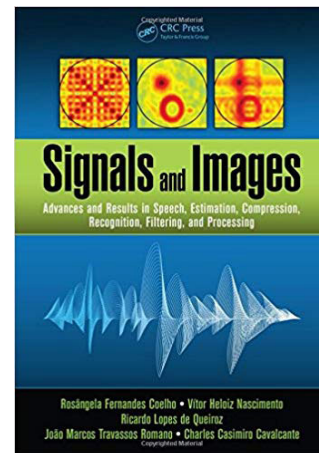
An email from my point of contact at CRC Press just arrived in my mailbox.

*“Dear Melissa, We have these titles ... your journal might be interested in reviewing... Kind Regards,  
Hard-working CRC Press Employee”*

[A confession: at times, I have judged a book by its cover or title] – I consented to have the journal review “Signals and Images” without much thought, so much of what we do in Remote Sensing is the manipulation of the encoded signal displayed as images. Every image is signal, every bit of image processing is statistical or model-driven manipulations of encoded signal, this should be a straightforward review. A reviewer had been chosen, the review lined up and the book sent but then all that fell apart and the book languished on my desk for nearly 2 years.

The book, “*Signals and Images*”, consists of five parts: Part 1—Theory and Methods; Part 2—Acoustic Signal Processing; Part 3—Image Processing; Part 4—Signal Processing in Communications; Part 5—Selected Topics in Signal Processing. The review was never supposed to tackle the entire broad spectrum of signal processing addressed by the book’s many contributors to this 598 page edited volume. The review for the journal was to be much more manageable, only concerning itself with Part 1—Theory and Methods and Part 3—Image Processing.

Enough languishing, I thought, sitting at my desk, a review must be written. Thinking about an image interpretation undergraduate classroom, I sat in many years ago. Seeing the “checklist” our professor had given us which included as many boxes about “bits<sup>1</sup>” and “brooms<sup>2</sup>” to check as it did “season” and “sun-angel<sup>3</sup>” – the words echoing in my head time and again to remember to ask, where the image came from [i.e., how the signal was captured/encoded] and what has happened to the signal since then, [i.e., how has it been processed since encoding]. This reviewer endeavors to plunge into signals headfirst, hoping to find friendly sensors and algorithms. A small aside, our image interpretation professor was as much



## Signals and Images: Advances and Results in Speech, Estimation, Compression, Recognition, Filtering, and Processing

Rosângela Fernandes Coelho, Vitor Heloiz Nascimento, Ricardo Lopes de Queiroz, João Marcos Travassos Romano, Charles Casimiro Cavalcante

CRC Press, 2017. ISBN 9781138893016 - CAT# K32817

Review by Melissa J. Rura-Porterfield, Ph.D.

concerned with the technical underpinnings of how an image was captured as what one might discern by looking at the output of the capture.

**Part 1—Theory and Models** which includes Chapter 1 on blind source separation [independent component separation]; Chapter 2 on kernel-based non-linear signal processing; Chapter 3 on arithmetic transformed methods for trigonometric discrete transforms and finally Chapter 4 on agent modeling. Coming from a perspective in Remote Sensing, used to texts like *Remote Sensing: The Quantitative Approach* among others [4, 5, 6, 7, 8] that tend to emphasize signal processing for geometric correction, signal variance under atmospheric conditions, or signal encoding for specific sensor platforms, particularly for moving or orbiting platforms, this section sort of left this

- 1 Quantization levels [from the check list including: IFOV at nadir; Data Rate; Quantization levels; Earth coverage; Altitude; Swath Width; Inclination]
- 2 Sensor Technology [Frame, Push Broom; Whiskbroom...]
- 3 Remote Sensing and Image Interpretation, 7th Edition by Thomas Lillesand, Ralph W. Kiefer, Jonathan Chipman
- 4 Introductory Digital Image Processing by John R. Jensen
- 5 Pattern Classification by Richard O. Duda, Peter E. Hart, David G. Stork
- 6 Remote Sensing: The Image Chain Approach by John R. Schott
- 7 Introduction to Modern Photogrammetry by Edward M Mikhail, James Bethel, Chris McGlone
- 8 Remote Sensing: The Quantitative Approach by P. H. Swain (Editor), Shirley M. Davis (Editor)

Photogrammetric Engineering & Remote Sensing  
Vol. 86, No. 2, February 2020, pp. 77–78.

0099-1112/20/77–78

© 2020 American Society for Photogrammetry  
and Remote Sensing  
doi: 10.14358/PERS.86.2.77

reader wanting. Part 1's perspective seemed singular for such a broad text. Although the preface billed the text possibly suitable as a textbook for undergraduate or graduate students this reviewer feels that the preface was more correct in encouraging this to be a supplement to a textbook or as a reference book for researchers.

**Part 3—Image Processing** includes Chapter 9 on energy-aware video compression; Chapter 10 on rotation and scale-invariant template matchings and Chapter 11 on 3D-TV. As I read this sitting at my desk thinking about the image chain,<sup>6</sup> my heart dropped and my disappointment became clear and proved my folly in cover/title judging. There was nothing about image capture at all, nor was encoding or atmosphere or even transmission to be read here. Although the authors do from a perspective address a type of image processing, I was left wondering about how Remote Sensing got forgotten in the discussion. But, just like my British friends like to tell me, "Melissa, the America Revolution only got one paragraph in our 8th-grade history book, I don't remember much about it..." In the broadness of the topic "*Signals and Images*" the perspectives that come out of Remote Sensing and Photogrammetry were overlooked or did not register as of much importance to these authors. Probably, the book review editor at the time, myself, misjudged the book's audience and should have paid closer attention to the Table of Contents.

There is much we in Remote Sensing can learn about signal capture, signal encoding, signal processing, and signal transmission, first and foremost is to remind ourselves regularly that every image is a signal encoded for our viewing pleasure and secondly there is a whole branch of knowledge devoted to understanding that better. Although, I learned much from this book and do recommend it, probably the most important takeaway today is to encourage our readership to not lose sight of their image chain. Asking questions like 1) "How / When / Where / Why was this image captured?" 2) "How / When / Where / Why has this image been processed?" 3) "How does that effect my intentioned uses of the image?"

We must stand firm in the collection and maintenance of metadata. Remembering that time way back when, when your professor gave you that checklist and you knew that your "bits" and "bytes," and "brooms" had better be in order and if you had band interleave, band sequential was not going to load for your viewing pleasure, so pay attention. No matter how far away we get from those checklists do not forget to remember your professor asking you, time and again, how was this image captured and what has happened to it since then?

## STAND OUT FROM THE REST

## EARN ASPRS CERTIFICATION

ASPRS congratulates these recently Certified and Re-certified individuals:

### CERTIFIED PHOTOGRAMMETRIST

**James Powers, Certification #1648**

Effective November 26, 2019, expires November 26, 2024

### RECERTIFIED PHOTOGRAMMETRISTS

**Robert Lafica, Certification #R1241**

Effective August 26, 2019, expires August 26, 2024

**Marlin R. Zook, Certification #R920**

Effective May 21, 2019, expires May 21, 2024

**Douglass Ward, Certification #R1242**

Effective September 8, 2019, expires September 8, 2024

**Amar Nayegandhi, Certification #R1569**

Effective July 21, 2019, expires July 21, 2024

**Mitchell Jay Long, Certification #R1411**

Effective July 23, 2019, expires July 23, 2024

### RECERTIFIED PHOTOGRAMMETRIC TECHNOLOGIST

**Sean Harrison, Certification #R1607PT**

Effective November 30, 2019, expires November 30, 2022

ASPRS Certification validates your professional practice and experience. It differentiates you from others in the profession. For more information on the ASPRS Certification program: contact [certification@asprs.org](mailto:certification@asprs.org), visit <https://www.asprs.org/general/asprs-certification-program.html>



## JOURNAL STAFF

### Editor-In-Chief

Alper Yilmaz, Ph.D., PERSeditor@asprs.org

### Associate Editors

Rongjun Qin, Ph.D., qin.324@osu.edu

Michael Yang, Ph.D., michael.yang@utwente.nl

Petra Helmholtz, Ph.D., Petra.Helmholtz@curtin.edu.au

Bo Wu, Ph.D., bo.wu@polyu.edu.hk

Clement Mallet, Ph.D., clemallet@gmail.com

Vasit Sagan, Ph.D., Vasit.Sagan@slu.edu

Jose M. Pena, Ph.D., jmpena@ica.csic.es

Prasad Thenkabail, Ph.D., pthenkabail@usgs.gov

Ruisheng Wang, Ph.D., ruiswang@ucalgary.ca

Desheng Liu, Ph.D., liu.738@osu.edu

Valérie Gouet-Brunet, Ph.D., valerie.gouet@ign.fr

Dorota Iwaszczuk, Ph.D., dorota.iwaszczuk@tum.de

Qunming Wang, Ph.D., wqm11111@126.com

Filiz Sunar, Ph.D., fsunar@itu.edu.tr

Norbert Pfeifer, Ph.D., np@ipf.tuwien.ac.at

Jan Dirk Wegner, Ph.D., jan.wegner@geod.baug.ethz.ch

Hongyan Zhang, Ph.D., zhanghongyan@whu.edu.cn

Zhenfeng Shao, Ph.D., shaozhenfeng@whu.edu.cn

Dongdong Wang, Ph.D., ddwang@umd.edu

### Assistant Editor

Jie Shan, Ph.D., jshan@ecn.purdue.edu

### Contributing Editors

#### Grids & Datums Column

Clifford J. Mugnier, C.P., C.M.S., cjmce@lsu.edu

#### Book Reviews

Sagar Deshpande, Ph.D., bookreview@asprs.org

#### Mapping Matters Column

Qassim Abdullah, Ph.D., Mapping\_Matters@asprs.org

#### Sector Insight

Lucia Lovison-Golob, Ph.D., lucia.lovison@sat-drones.com

Bob Ryerson, Ph.D., FASPRS, bryerson@kingeomatics.com

#### GIS Tips & Tricks

Alvan Karlin, Ph.D., CMS-L, GISP akarlin@Dewberry.com

### ASPRS Staff

#### Assistant Director — Publications

Rae Kelley, rkelley@asprs.org

#### Electronic Publications Manager/Graphic Artist

Matthew Austin, maustin@asprs.org

#### Advertising Sales Representative

Bill Spilman, bill@innovativemediasolutions.com

# ASPRS NAMES 2020 LIFE-TIME ACHIEVEMENT AWARD RECIPIENT

## Marguerite Madden to receive the 2020 ASPRS Life-Time Achievement Award.



Dr. Marguerite Madden, is a Professor in the University of Georgia (UGA) Department of Geography and Director of the Center for Geospatial Research (CGR). She holds Bachelor and Master of Arts degrees in Biology from the State University of New York and Ph.D. in Ecology from the University of Georgia. Since the late 1970s, she has conducted research combining geospatial data and analyses with landscape ecology, particularly focused on human-animal-environment interactions. Joining the UGA-CGR in 1985, she and her colleagues developed and analyzed numerous multi-temporal and detailed vegetation databases for local, state

and national conservation lands, including over 20 National Park units located throughout the Southeastern United States. Dr. Madden's current research interests include remote sensing, geographic information systems (GIS), spatio-temporal analysis, geovisualization and geographic object-based image analysis, as applied to landscape-scale biological/physical processes and human-impacts on the environment. Prioritizing the involvement of students in her research, she has served as major advisor to 21 Ph.D. and 19 M.S./M.A. students since joining the UGA faculty in 2005. Professor Madden is a Past President of ASPRS, Editor of the 2009 ASPRS Manual of GIS and the current co-chair of the ASPRS Education and Professional Development Committee. She served as the International Society for Photogrammetry and Remote Sensing (ISPRS) Commission IV, "Digital Mapping and Geodatabases" Technical President (2008-2012), ISPRS Council Second Vice President (2012-2016) and Treasurer of The ISPRS Foundation (2010 to present). She is the lead Science Advisor of the Georgia node of the NASA DEVELOP National Program (2014 to present) and the recipient of the ISPRS Willem Schermerhorn Award (2004), ASPRS Fellow Award (2010), ASPRS SAIC Estes Memorial Teaching Award (2011) and NASA Silver Achievement Medal (2018).

The ASPRS Life-Time Achievement Award, originally established in 1937 as the Honorary Member Award, is the Society's highest honor and was designed to showcase those who contributed to the science and technology and the Society throughout one's lifetime.

The Award recognizes lifetime achievements of an individual who has attained distinction in photogrammetry, remote sensing, geospatial sciences, or related fields, at the highest levels.

The total number of living Lifetime Achievement Awardees may not exceed twenty-five at any given time, and no more than two will be elected in one year.

## NEW ASPRS MEMBERS

ASPRS would like to welcome the following new members!

### At Large

Sudarshan Koti, Jr.  
Dr. Jun Ma  
Wenxiu Teng

### Columbia River

Dr. Alex Malek

### Eastern Great Lakes

Huijun Chen  
Brendan Welsh

### Florida

Thomas Blythe  
Zoey Holden  
Kaitlyn Noelle Maynard

### Heartland

Yuyu Zhou

### Intermountain

Keith Peterson

### Mid South

Alfred H. N. Mfondoum  
Prasanth Ramachandran  
Lynn Abdouni  
Bidemi Saheed Adejumo  
Brian J. Mayfield, CP

### Pacific Southwest

Jocelyn L. Correa

### Potomac

Jake Aytes  
Bethany Bashor  
Terra McKee  
Rachael Taylor

### Puget Sound

Novica Janicijevic

### Rocky Mountain

Adam Collins

### Western Great Lakes

Shuang Song

FOR MORE INFORMATION ON  
ASPRS MEMBERSHIP, VISIT

[HTTP://WWW.ASPRS.ORG/JOIN-NOW](http://www.asprs.org/join-now)

*Your Path To Success  
In The Geospatial Community*

## ASPRS ANNOUNCES AWARDS RECIPIENTS

**A**wards to be presented at the ASPRS Annual Conference as part of Geo Week and in conjunction with the 2020 ILMF Conference

### 2020 Photogrammetric Fairchild Award Recipient

Jie Shan, Professor

*Purdue University- School of Civil Engineering*

The purpose of the Award is to stimulate the development of the art of aerial photogrammetry in the United States.

### 2020 Fellow Award Recipients

John S. Iames, Jr., Research Scientist

*Environmental Protection Agency*

Riadh A. Munjy, Professor

*California State Univ., Fresno, Lyles College of Engineering*

Tim Warner, Professor

*West Virginia University, Dept of Geology and Geography*

Qihao Weng, Director

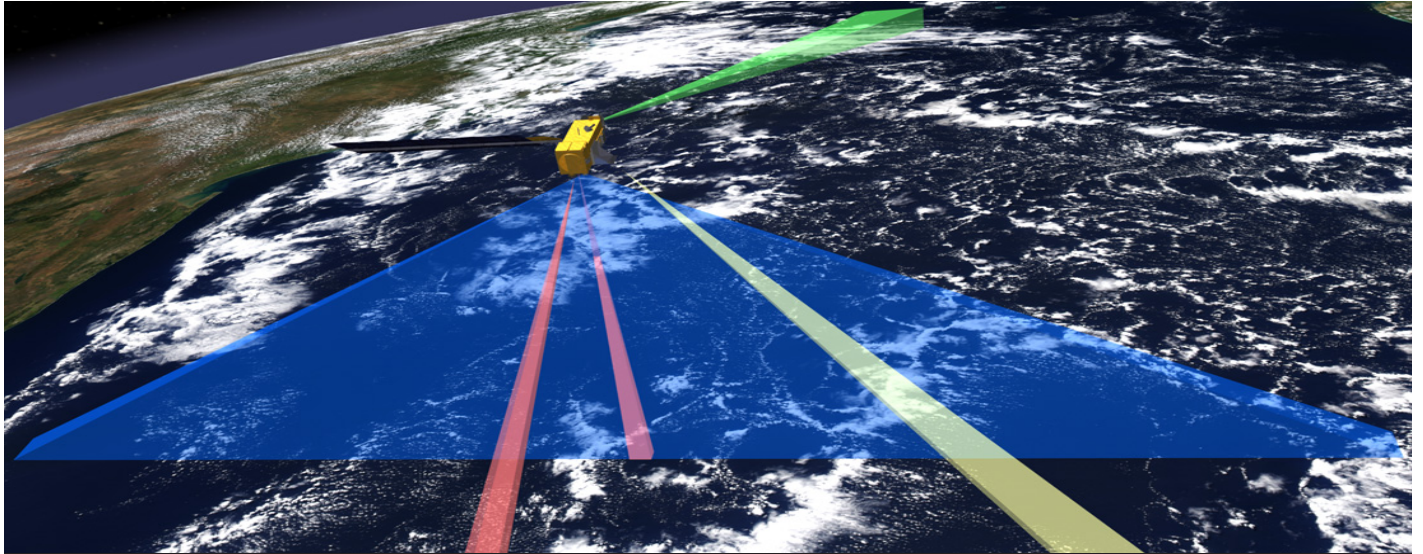
*Center for Urban & Environmental Change at Indiana State University*

The designation of Fellow is conferred on active Society members who have performed exceptional service in advancing the science and use of the mapping sciences and is awarded for professional excellence and for service to the Society. Nominees must have made outstanding contributions in a recognized Society specialization whether in practice, research, development, administration, or education in the mapping and related sciences.

### 2020 ASPRS Outstanding Technical Achievement Award Recipients

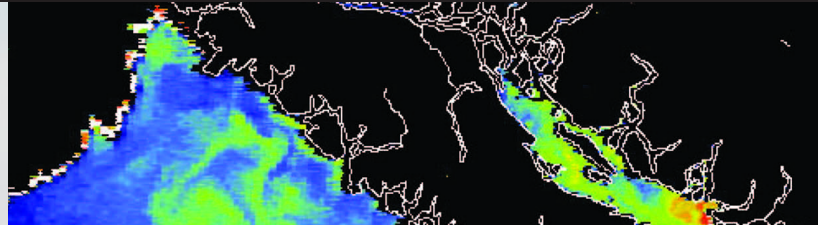
**USGS Digital Orthophoto Quad (DOQ) Technical Team: David Hooper, Lyman Ladner, George Lee and Randy Olsen.**

Using mathematics to differentially rectify pixels in digitized or digital imagery to produce image maps, with an approach that continues to impact remote sensing and GIS processes, was developed at the USGS Western Mapping Center. In 1986 a prototype digital orthophoto quadrangle (DOQ) production system launched an effort that not only improved USGS support to the federal civil mapping community but also stimulated an initiative within the Department of Defense. This award is to recognize the innovative drive of the initial proposal that was a turning point in the use of digital imagery and which laid the groundwork for today's democratization of imagery and remote sensing use and GIS.



# MANUAL OF REMOTE SENSING

## *Fourth Edition*



### Announcing the 4<sup>th</sup> Edition of the Manual of Remote Sensing

The fourth edition of the ASPRS *Manual of Remote Sensing, 4<sup>th</sup> Ed.* is an “enhanced” electronic publication available online from ASPRS. This edition expands its scope from previous editions, focusing on new and updated material since the turn of the 21<sup>st</sup> Century. Stanley Morain (Editor-in-Chief), and co-editors Michael Renslow and Amelia Budge have compiled material provided by numerous contributors who are experts in various aspects of remote sensing technologies, data preservation practices, data access mechanisms, data processing and modeling techniques, societal benefits, and legal aspects such as space policies and space law. These topics are organized into nine chapters. MRS4 is unique from previous editions in that it is a “living” document that can be updated easily in years to come as new technologies and practices evolve. It also is designed to include animated illustrations and videos to further enhance the reader’s experience.

The *Manual of Remote Sensing, 4<sup>th</sup> Ed.* will be available the beginning of 2020. All ASPRS members will have complimentary unlimited access to MRS as part of their ASPRS member benefits. Non-ASPRS members will be able to purchase access to MRS. More information will be announced in *PE&RS* and in the ASPRS eNewsletter. In the meantime, enjoy this preview of MRS.

edited by: Stanley A. Morain,  
Michael S. Renslow and Amelia M. Budge



# Table of Contents

## Preface

Stanley A. Morain, Michael S. Renslow, and Amelia M. Budge

## Chapter 1: Fundamentals of Electromagnetic Radiation

Stanley A. Morain and Amelia M. Budge

## Chapter 2: Sensors and Platforms

Charles K. Toth, Kenneth Jezek, Franz Meyer, Batuhan Osmanoglu, Stanley A. Morain and Amelia M. Budge

## Chapter 3: Selected 21st Century Remote Sensing Technologies

Stanley A. Morain, Shizuo Yamamoto, Yves Tourre, C. Vignolles and J-P. Lacaux

## Chapter 4: Unmanned Aerial Systems for Low-Altitude Remote Sensing

Costas Armenakis, Brandon Stark, Brendan Smith, YangQuan Chen, Ravi A. Persad, Julien Li-Chee-Ming, Norbert Haala, Michael Cramer, Jeff L. Sloan and Jill J. Cress

## Chapter 5: Quality Assurance and Quality Control of Remote Sensing Systems

Ayman Habib, Eija Honkavaara, Karsten Jacobsen, Ana Paula Kersting, Zahra Lari, Aparajithan Sampath, Ahmed Shaker and Wai Yeung Yan

## Chapter 6: Archiving and Access Systems for Remote Sensing

John Faundeen, George Percivall, Shirley Baros, Peter Baumann, Peter Becker, J. Behnke, Karl Benedict, Lucio Colaiacomo, Liping Di, Chris Doescher, J. Dominguez, Roger Edberg, Mark Ferguson, Stephen Foreman, David Giaretta, Vivian B. Hutchison, Alex Ip, N.L. James, Siri Jodha S. Khalsa, B. Lazorchak, Adam Lewis, Fuqin Li, Leo Lymburner, C.S. Lynnes, Matt Martens, Rachel Melrose, Steve Morris, Norman Mueller, Vivek Navale, Kumar Navulur, D.J. Newman, Simon Oliver, Matthew Purss, H.K. Ramapriyan, Russ Rew, Michael Rosen, John Savickas, Joshua Sixsmith, Tom Sohre, David Thau, Paul Uhler, Lan-Wei Wang and Jeff Young

## Chapter 7: Image Processing and Analysis Methods

Sergio Bernardes, Marguerite Madden, Ike Astuti, Sergio Bernardes, Emilio Chuvieco, David Cotten, Philip E. Dennison, Iryna Dronova, Ioannis Gitas, Peng Gong, Belen Franch-Gras, Matt Hancher, Akira Hirano, Allison Howard, Xuefei Hu, Alfredo Huete, Thomas Jordan, Chris Justice, Rick L. Lawrence, Linlin Lu, Marguerite Madden, Deepak R. Mishra, Sachidananda Mishra, Tomoaki Miura, Giorgos Mountrakis, Mahesh Pal, Caren Remillard, Dar A. Roberts, Jean-Claude Roger, Kunwar K. Singh, Ben Somers, Dimitris Stavrakoudis, Wanxiao Sun, Guoqing Sun, David Thau, Laurent Tits, E. Lynn Usery, Eric Vermote, Cuizhen Wang, Mingshu Wang, Qihao Weng, Wenjing Xu, Tian Yao, Hiroki Yoshioka, Lei Zhang, Qingyuan Zhang and Zhi Zhang

## Chapter 8: Societal Benefits - Methods and Examples for Estimating the Value of Remote Sensing Information

Richard Bernknopf, David Brookshire, Molly Macauley, Guy Jakeman, Yusuke Kuwayama, Holly Miller, Leslie Richardson and Alan Smart

## Chapter 9: Space Policy and Space Law

Jeanne Gabrynowicz, Karen D. Dacres, Kevin O'Connell, Kevin Pomfret and Timothy F. Robertson

## Appendix A

## Master Acronym List

# Chapter 1: Fundamentals of Electromagnetic Radiation

## SCIENTIFIC BASIS FOR 21ST CENTURY REMOTE SENSING

Remote Sensing, its component sciences, technologies, and applications are all governed by the universal physics of energy interacting with matter at scales from subatomic to galactic. MRS-1, -2, and -3 describe hardware, software, and data processing developments for an exploding suite of airborne and space-borne platforms and sensors; and the resulting array of Earth and planetary science applications. These editions are overwhelmingly Earth-oriented to monitor Earth's environments across spatial and temporal time-scales; and to develop methodologies for measuring and monitoring local-to-global phenomena. To maximize these capabilities, it has proven necessary for communities-of-practice to work within a broad framework that includes engineering designs that integrate environmental engineering, scientific, economic, human, and social considerations that, together, define the suite of remote sensing technologies. MRS-4 concentrates on state-of-the-art platforms, sensors, processing technologies and applications since the turn of the 2nd Millennium. Chapter 1 addresses basic matter and energy relationships as mathematical expressions; and

where possible, as illustrated in animated and interactive graphics from the World Wide Web. However, much of the graphical material from the Web is limited to screen resolution (72dpi).

The term *remote sensing* was coined in the United States by Evelyn Pruitt at the U.S. Office of Naval Research (ONR) to describe processes for identifying, observing, and measuring radiation from objects on the Earth's surface (Graham, 1999; see <http://earthobservatory.nasa.gov/Features/RemoteSensing/>). Secret activities were in use in the 1950s in the form of Corona imagery obtained from high altitude U-2 flights over the Soviet Union and the downing of one flight piloted by Francis Gary Powers on May 1, 1960. For a concise pictorial history of early high altitude and space-based imaging programs see Baumann (2009) (<http://www.oneonta.edu/faculty/baumanpr/geosat2/RS%20History%20II/RS-History-Part-2.html>). Advances in these technologies over the subsequent five-to-six decades are the basis for the first three editions of the *Manual of Remote Sensing*.

## Chapter 2: Sensors and Platforms

### INTRODUCTION

Remote sensing technologies have proliferated greatly in recent years. Unprecedented developments in sensing technologies and platforms have resulted in information-rich geospatial data acquisition, which, in turn, has driven applications by extending remote sensing performance as well as by creating new application fields from ground through space. The performance level and the application space of the sensors in terms of spatial, spectral and temporal sensing abilities have expanded far beyond the conventional boundaries of remote sensing. This chapter is dedicated to sensors and platforms that generally are not separable.

Sensors used for mapping Earth and Space observations generally fall into two major categories: active and passive. While technological developments are equally strong in both groups, active sensors often get more attention for two reasons. First, they generally provide direct three-dimensional (3D) observations, resulting in more robust surface and shape extraction. Second, active sensors are usually less dependent on environmental circumstances of the observation space, such as not needing ambient light, and they may have certain penetration capabilities through vegetation and/or cloud cover. Radio Detection and Ranging (Radar) sensors are used for imaging larger geographic areas, acquiring data from high-altitude flights and space. In contrast, Light Detection and Ranging (LiDAR) has a local character, allowing dense data acquisition of smaller areas, and acquiring aerosol measurements from space.

Passive sensors have a long history and produce the largest volume of remotely sensed data. Optical imaging has seen remarkable developments in both spatial and spectral resolution capabilities. Digital cameras can produce images easily in the billion pixel range (Gpix) by either single sensors, such as a 400 megapixel (Mpix) single sensor; or, by using multiple sensors and/or camera

heads. Spectral capabilities continue to improve in both single channel radiometric performance and in the number of spectral bands. Multispectral sensing is becoming ubiquitous, and the use of hyper-spectral imaging is growing rapidly. With the explosion of smartphones and consumer cameras, the amount of imagery acquired is skyrocketing, and crowd-sensing technologies add a totally new approach for observations at large scale.

Airborne and satellite systems represent traditional remote sensing platforms and these technologies have shown little development in recent years. In the past decade, however, major changes have appeared that simply redefine the field of remote sensing platforms from ground through space. First, Unmanned Airborne Systems (UAS) have grown from "hobby-level uses", to performance levels that offer viable alternatives between airborne and ground vehicle-based platforms. UAS provides unmatched maneuverability with easy deployment, and small optical cameras and/or other sensors can collect high spatial and spectral resolution data. Given the extremely small ground sampling distance (GSD) of UAS-based optical remote sensing systems, accurate point clouds can be generated easily by using dense image matching.

Recent developments in satellite platforms are similarly significant to the introduction of UAS. First, the use of agile sensors has become general on high-end satellite systems, allowing better image acquisition rates as well as in-track stereo capabilities. Next, to decrease revisit time, satellite constellations have been introduced, bringing down the revisit time to a matter of days, or less. Meanwhile, commercially available image resolution has continued to improve, standing currently at 30-50cm. Finally, the introduction of micro- and nano-satellites is probably the most noteworthy recent development. Deployed in clusters on the same orbit in multi-

orbit constellation, these systems allow for extremely low revisit times, and have high levels of orbit configuration capabilities.

Sensing platforms and sensor technologies currently are experiencing sustained and rapid development, and, in parallel, the operational envelope continues to expand. Crowd-sensed data provide new, highly redundant, geospatial data on the ground, including indoor

environments. UAS fills the gap between ground and conventional airborne platforms, while global data can be acquired increasingly from space. This Chapter provides samples from the exciting field of sensors and platforms. The material in this Chapter has been augmented recently by Toth and Józkó (2016).

## Chapter 3. Selected 21st Century Remote Sensing Technologies

### INTRODUCTION

Materials and topics in this Chapter have been assembled from space agencies around the world, many of which are available on the World-wide Web. Readers are encouraged also to review industry newsletters, trade journals, and vendor magazines because these sources describe advances in cutting-edge technologies, many on weekly or monthly schedules. National space agencies around the world feed user communities with ever-growing sources of data and information obtained by in-situ, aerial and space-based sensors and platforms. These outputs allow industry, academia, and commercial communities-of-practice to stay abreast of evolving technologies and applications. This chapter focuses on the Global

Earth Observing System of Systems (GEOSS), Nanotechnology, and Tele-epidemiology. This edition of the Manual of Remote Sensing is conceived to be a “living electronic manual” that can accommodate future technological advances as they emerge. To be successful, it will be necessary to promote a steady flow of new and emerging technologies that keep abreast of remote sensing hardware, software, and applications development. The following is a brief synopsis of three remote sensing technologies and applications in the first two decades of the 21st Century. Already a third technical arena, Drones, and a fourth, information systems, have advanced from concept to daily applications.

## Chapter 4 Unmanned Aerial Systems for Low-Altitude Remote Sensing

### INTRODUCTION

The last decade has witnessed the emergence of a new aerial platform for collecting geospatial data, the self-propelled Unmanned Aerial Systems (UAS) with no human operator onboard. UAS, also known as Remotely Piloted Aircraft Systems (RPAS), Unmanned Aerial Vehicles (UAV), or simply “drones” are transforming geomatics research and applications and creating new and innovative opportunities. It is believed that the first UAV was built around 425 B.C. by Archytas the Tarantine (Valavanis and Kontitsis, 2007). It was a self-driven flying pigeon-shaped device propelled by a jet of compressed air or steam (AET, 2014) that could cover a distance of approximately 200m. Unmanned aerial platforms originated and are mostly used in military applications supporting the so-called three “Ds” (dull, dirty, or dangerous missions in which a human pilot would be at a disadvantage or at high risk). The National Aeronautics and Space Administration’s (NASA) Environmental Research Aircraft and Sensor Technology (ERAST) program in the 1990s introduced the development of protocols and capabilities for using UAS in support of scientific research. NASA also has used them for fire-fighting (Wegener, 2000).

UAS now enjoy wide popularity, featuring very different types of platforms for numerous civilian applications such as scientific, commercial, public safety, and recreational activities. This chapter does not consider the military and space UAV, but focuses on small, light-weight, low-cost, and easy to operate UAS. Several market studies in the recent past have indicated a multi-billion dollar UAV market expansion in the next 10 years. According to the 2014 Teal Group market study (Teal Group, 2015), it is estimated that UAV spending will nearly double over the next decade from a current UAV world-wide expenditure of \$6.4 billion annually to \$11.5 billion,

totaling almost \$91 billion in the next ten years. The commercial RPAS market is set to expand and overtake the traditional military markets in the very near future. Applications include remote sensing and mapping, wildlife survey, commercial delivery, communication and broadcast, pipeline and power line monitoring, forest fire detection, resource exploration, precision agriculture, construction, surveillance, meteorology, photography, and search and rescue to name a few.

While UAS are pilotless, as systems they can be remotely controlled (RC), automatic, autonomous or a combination of these. There is a difference in using the terms automatic and autonomous (Transport Canada, 2014a). Automatic means the execution of a pre-defined process or event that requires UAV pilot initiation and/or intervention (e.g., automated take-off/landings, way-point navigation, auto-pilots, pre-programmed maneuvers, etc.). Autonomy is the ability to execute processes or missions using onboard decision-making capabilities; that is, the UAV system is not designed to permit crew member intervention. There are numerous UAS from small and simple RC models to large and complex UAS that can operate for longer distances, at high altitudes, and have high endurance with minimum operator intervention.

Based on their airframe type, UAVs usually are fixed-wing or multi-rotor (quad-, hexa-, octo-, etc.) aerial vehicles, but also paragliders and lighter than air (i.e., airships, balloons).

Fixed wing vehicles have longer ranges, better endurance, faster speeds, have a higher payload capacity and are most stable in poor weather conditions (e.g., high / cross winds) and may require a launching catapult or can be hand-launched. Usually small fixed wing UAVs are not equipped with landing gear and

crash land (“belly landing”). The multi-rotor types have the capability for vertical take-off and landing (VTOL), a feature of particular interest as they can operate in tighter and in-door spaces, around structures, and they have high maneuvering and hovering

abilities. There also are hybrid fixed-wing systems, VTOL UAV, such as the SONGBIRD (Thamm et al., 2015). For propulsion, electric (including solar) and gas /diesel engines are used.

## Chapter 5: Quality Assurance and Quality Control of Remote Sensing Systems

### INTRODUCTION

In the last few years, the mapping community has witnessed significant developments in using passive and remote sensing technologies onboard space-borne, airborne, and terrestrial platforms to provide a wide range of products. These developments can be ascribed to 1) proliferation of high resolution space borne imaging satellites operating in different portions of the electromagnetic spectrum, 2) reduced cost and improved performance of modern color, multispectral, and hyperspectral digital cameras, 3) continuous developments in Light Detection and Ranging (LiDAR) systems, 4) capability of integrated Global Navigation Satellite Systems/ Inertial Navigation Systems (GNSS/INS) in providing accurate position and orientation information for the utilized platforms, 5) incorporation of multiple cameras and/or laser scanners onboard a single platform, 6) emergence of non-traditional mapping platforms such as airborne and terrestrial unmanned autonomous systems - UAS, 7) convergence of research efforts from the mapping and computer vision communities, and 8) increased demand for geospatial data to satisfy the needs of non-traditional applications (e.g., precision farming, infrastructure monitoring, powerline clearance evaluation, and construction engineering management).

Taking advantage of such developments in the remote sensing technologies is only possible when standard Quality Assurance and Quality Control (QA/QC) procedures are in place to ensure the utmost precision of the mapping product. In this chapter, the term “Quality Assurance – QA” is used to denote pre-mission activities focusing on ensuring that a process will provide the quality needed by the user. On the other hand, the term “Quality Control – QC” is used to denote post-mission procedures for evaluating the quality of the final product. QA mainly deals with creating management controls including the calibration, planning, implementation, and review of data collection activities. For example, a LiDAR-based QA activity should entail gaining prior knowledge of the area to be surveyed in terms of its extent and terrain coverage (e.g., vegetation and buildings) to set up the appropriate flight configuration and specifications. In forested areas, a slower speed, smaller scan angle, higher overlap percentage, and/or lower flying height might be necessary to increase the point density and to have more pulses penetrating to the ground. Also, the selection of the appropriate mission time according to the GNSS satellite constellation distribution is another important QA item. For example, a typical requirement is to have at least four well-distributed satellites with elevation angles above 15° throughout the survey. Moreover, it is recommended that the aircraft should stay within a given distance from the GNSS base station. Another QA activity for LiDAR mapping is the system calibration. For such an activity, one should have access to the original observations (GNSS, IMU, and the laser measurements) or at least the trajectory and time-tagged point cloud. Such quantities might not be always available to the end user. This Chapter will be

mainly focusing on the system calibration component of QA activities.

For an illustration of standard QC activities, one can refer to the well-established photogrammetric procedures for evaluating the internal/relative and the external/absolute accuracy of the final product. For the evaluation of the internal/relative quality (IQC) of the outcome from a photo-grammetric reconstruction exercise, we typically use the a-posteriori variance factor and the variance-covariance matrix resulting from the bundle adjustment procedure. As for the external/absolute quality (EQC) evaluation, checkpoint analysis using independently measured targets is usually performed. Since the computation of the LiDAR point cloud is not based on redundant measurements, which are manipulated in an adjustment procedure, standard photogrammetric IQC measures are not possible. Moreover, the irregular and sparse nature of the LiDAR point cloud makes the EQC process more challenging. A commonly used EQC procedure compares the LiDAR surface with independently collected control points. Besides being expensive, this procedure does not provide accurate verification of the horizontal quality of the LiDAR points, unless specifically designed targets are utilized. Such inability is a major drawback since the horizontal accuracy of the LiDAR points is known to be inferior to the accuracy of these points in the vertical direction. In this regard, this Chapter addresses the validation of remote sensing data from space borne, airborne, and terrestrial platforms.

The chapter is organized as follows:

- Section 2: Geometric Calibration / Validation of High Resolution Imaging Sensors deals with the operational principles of modern high resolution imaging satellites as well as the geometric calibration and validation procedures which are adopted by the system manufacturers and end users, respectively.
- Section 3: Geometric Calibration / Validation of Airborne and Terrestrial Optical Imaging Systems provides the operational principles of single-head and multi-head airborne and terrestrial optical imaging systems together with their geometric calibration and validation in the presence or absence of onboard direct geo-referencing units.
- Section 4: Radiometric Calibration of Passive Optical Imaging Systems focuses on radiometric calibration and correction aspects of airborne and terrestrial, mobile passive imaging systems which operate in the reflective or thermal ranges of the electromagnetic spectrum.
- Section 5: Geometric Calibration for Active Remote Sensing Systems (LiDAR) provides important aspects for the geometric calibration of LiDAR systems while considering the possibility that the raw measurements are not always available.
- Section 6: Geometric Quality Control of LiDAR Data deals

with potential activities for ensuring the positional consistency and correctness of LiDAR point clouds while considering the fact that the point-positioning process is not based on redundant measurements and the difficulty in identifying corresponding points in overlapping strips and/or ground truth elevation data.

- Section 7: Radiometric Calibration, Correction, and Normalization of LiDAR Data: In addition to evaluating and improving geometric quality of LiDAR data, discussed earlier, this section deals with improving the radiometric quality of LiDAR intensity

data as well as the impact of such activity on further LiDAR data processing activities such as classification procedures.

- Section 8: Quality Control of LiDAR Data and Their Processing provides the technical details for characterizing LiDAR data; more specifically, evaluating the local point density and recent developments in evaluating LiDAR data quality and processing activities such as the segmentation process.

## Chapter 6: Archiving and Access Systems for Remote Sensing

### INTRODUCTION

MRS-4 Chapter 6, Archiving and Access, focuses on major developments inaugurated by the Committee on Earth Observation Satellites, the Group on Earth Observations System of Systems, and the International Council for Science World Data System at the global level; initiatives at national levels to create data centers (e.g. the National Aeronautics and Space Administration (NASA) Distributed Active Archive Centers and other international space agency counterparts), and non-government

systems (e.g. Center for International Earth Science Information Network). Other major elements focus on emerging tool sets, requirements for metadata, data storage and refresh methods, the rise of cloud computing, and questions about what and how much data should be saved. The sub-sections of the chapter address topics relevant to the science, engineering and standards used for state-of-the-art operational and experimental systems.

## Chapter 7: Image Processing and Analysis Methods

### INTRODUCTION

Recent developments for acquiring and distributing remotely-sensed data have greatly increased data availability to the user community. The past two decades have witnessed an explosion in data acquisition by a variety of ground, airborne and orbital sensors. The popularization of Unmanned Aerial Systems (UAS) and the development of reduced cost orbital platforms should guarantee that even higher data volumes will be available to future analysts. The past decades also saw the opening of image data archives (e.g., Landsat, CBERS, Sentinel), making access to a rich database of moderate resolution satellite images a reality across the globe. This increased volume and variety of remotely-sensed data increases the demand for methods and procedures for data handling and information extraction. This chapter, Image Processing and Analysis Methods, describes recent efforts to expand the analyst's data processing toolset and includes the theory and strategies used in manipulating remotely-sensed data by digital systems. The text focuses on presenting algorithms and techniques for image processing and analysis and emphasizes recent developments not covered by previous editions of the ASPRS Manual of Remote Sensing. Although the main topics covered by the chapter involve the direct processing of images, the text also covers concepts involved in processing remote sensing data that may not have been collected or stored as images, such as spectral curves acquired by spectroradiometers. Several sections of this chapter match this description, including Spectral Vegetation Indices and Spectral Mixture Analysis. Image processing includes not only the analysis of images, but also the necessary steps involved in preparing images for analysis, such as geometric correction, atmospheric correction and several techniques associated with image enhancement. Spectral indices resulting from the combination of multiple spectral bands are

presented, with emphasis on the description of vegetated targets. A detailed treatment is given to the mixture problem resulting from the contribution of multiple materials within the instantaneous field of view (IFOV) of a given sensor. Because multiple applications can benefit from the increased explanation power provided by a large number of spectral bands, hyperspectral data processing is also presented and discussed. Further, the chapter addresses the benefits and challenges involved in combining datasets acquired by different systems (Data Fusion). Image classification addresses multiple strategies involved in assigning classes to images (e.g., Support Vector Machine, and Decision Trees); and includes advances in Object-Based Image Analysis (OBIA), particularly those related to image segmentation in preparation for classification. Given the increasing length of remotely-sensed data time series, particular attention is given to preparing sequences of images and data, including multiple techniques for smoothing, spike removal and the retrieval of metrics associated with temporal variations of targets. The chapter also brings multiple examples of use of products derived from processing remotely-sensed data as input to a variety of workflows, including modeling and analysis efforts. Finally, very current topics involving recent advances in image acquisition and availability, are presented for generating 3D surfaces from multiple images using Structure from Motion (SfM); processing of very large datasets (Big Data); and processing of images in the cloud are presented.

## Chapter 8: Societal Benefits - Methods and Examples for Estimating the Value of Remote Sensing Information

### EXECUTIVE SUMMARY

*Remotely sensed data and information* (RSDI) is a form of infrastructure for decision-making that supports many societal activities. Remotely sensed data range over a wide array of spatial, temporal, and spectral resolutions and have many applications that can contribute to economic prosperity. Data collected using remote sensors have improved society's understanding of an array of Earth's natural and human systems by establishing baselines and monitoring changes. Monitoring spatiotemporal change provides a means to analyze how land use, land cover, air quality and sub-surface processes are affected by human and natural activities. Increasingly, these improvements in information have been applied in decision-making processes that take place in both the public and private sectors.

RSDI provides an input to other activities that are considered an intermediate economic good. As an intermediate good, the same RSDI can have many uses simultaneously. Because RSDI is digital, the cost of supplying the data is greatest to the first user; the cost of disseminating information to additional users is much smaller than the cost of obtaining information for the first user. In economics this situation is referred to as jointness-of-supply. This is true for the great majority of information goods and gives rise to the need for studies to demonstrate the socioeconomic benefits of the information. The benefits of RSDI are best demonstrated when an analysis explains how the data can be applied and used to make a particular decision.

This chapter is an overview of the approaches that have been undertaken to estimate the *value of information* (VOI) of RSDI and other digital geospatial information. The VOI for RSDI depends on what is at stake in a decision and how uncertain decision-makers are. In its simplest form, VOI is defined as the gains that result from making better decisions that are based on additional information

in the presence of uncertainty (e.g., benefits of improved weather forecasts). In addition to providing realized cost savings, RSDI provides new societal benefits from innovative applications (e.g., benefits of improved regulation of water quality). Examples of both types of analyses are provided in summaries of several case studies.

Section 1 is an introduction that presents an overview of the VOI concept from an economist's perspective. Descriptions of the microeconomics approach in Section 2 and macroeconomics approach in Section 3 follow the introduction. The microeconomic models focus on quantitative evaluations of individual decisions with uncertain information. The approach requires a specific application of remote sensing information and involves a comparison of the benefits in a scenario in which data are used to a scenario in which the data are not available. Included in this part of the chapter are: a formal development of a Bayesian decision model to determine VOI in Section 2.3, a summary of cost – benefit analysis in Section 2.5.1, and empirical valuation of publicly provided RSDI using stated preference methods in section 2.5.2. In Section 3 macroeconomic approaches are described that include input/output analysis in Section 3.2 and computable equilibrium models in Section 3.3. These models address the VOI problem in a different manner. The models are assumed to represent an economy that is in equilibrium. The economic impact of remotely sensed data can be evaluated at the national, regional, and local scales to evaluate policies and regulations. Following the description of the various approaches to quantifying VOI from RSDI, there are brief summaries of fifteen case studies. A discussion and summary follows.

1 <http://www.oxfordreference.com/view/10.1093/oi/authority.20110803100023635>.

## Chapter 9: Space Policy and Space Law

### INTRODUCTION

This chapter takes a holistic look, from the perspective of a data user, of the legal considerations that ought to be accounted for when acquiring data. To this end, a discussion of data gathering platforms is integrated into these considerations rather than having the chapter organized according to platform type.

The chapter takes a U.S.-centric perspective but also includes

non-U.S. materials and perspectives as well. Laws and regulations of other nations are also addressed. Lessons learned and thoughts about moving forward to increase the effectiveness of data access and use are also included. The chapter is written for a professional layperson; that is, a remote sensing professional.

## Preface

The first *Manual of Remote Sensing* (MRS-1) was a 2-volume compendium exceeding 3100 pages published by the American Society of Photogrammetry (ASP) in 1975. It was meant to be a bridging device between ASP's *Manual of Photographic Interpretation* (published in 1944) and as a consequence was weighted heavily toward airborne and space-borne imaging. However, it included material on rapidly evolving technologies across both the visible and longer wavelengths of the electromagnetic (EM) spectrum. In fact, the term remote sensing has a longer and somewhat more shadowy history. Sometime in the 1950s, the term, as first used in the United States, is credited to Evelyn Pruitt, then at the U.S. Office of Naval Research (ONR), to describe the process for identifying, observing, and measuring radiation from objects on the Earth's surface. That such activities were in use in the '50s is confirmed by top secret Corona imagery obtained from high altitude U-2 over-flights of the Soviet Union and the downing of one flight piloted by Francis Gary Powers on May 1, 1960. Advances in these technologies, and their transformations over the past 60+ years, are the basis for the *Manual of Remote Sensing*.

MRS-1 (Vol. 1) was divided into 21 Chapters, reprising the unclassified histories of airborne cameras, camera systems, and the analytical techniques used to conduct qualitative and quantitative analyses across a wide range of Earth systems and environments. Several of the chapters included early results from the Earth Resources Technology Satellite (ERTS-1). Volume 2 was divided into 26 chapters introducing the electro-magnetic spectrum, energy/matter interactions, platform and sensor designs, sensor physics, data transmission, and data processing techniques required to convert electronic and photographic data into useful information about Earth environments. MRS-1 was a game-changer for ASP, which soon changed its name to the American Society for Photogrammetry and Remote Sensing (ASPRS). As transformative as it was, MRS-1 was encyclopedic. It can be found, if at all, in university and industry libraries.

MRS-2 was published in 1983. Like MRS-1, it was a two-volume set. Volume 1 addressed theory, instruments and techniques in 25 Chapters (1232 pages.); and Volume 2 addressed interpretation and applications in 10 Chapters (1207 pages.). Volume 2 also contained a lengthy color quire of aerial, satellite (mainly Landsat-1), and extraterrestrial

images illustrating the range of image types and spatial resolutions then available. MRS-2 established the unclassified mathematical basis for acquiring and applying remotely sensed data to Earth's terrestrial, aquatic, and atmospheric environments, thus establishing the field as much broader than traditional photogrammetry. Its impact was to establish the technical basis for more than three decades of explosive growth in academic programs, remote sensing research centers, and global networking (1983-2009). It is now out-of-print but as of March 2015, was still available in limited quantities from online book sellers.

MRS-3 focused on the rapidly expanding range of platforms, sensors and applications in a series of hard-copy, thematic volumes. Between 1997 and 2009 six volumes were published before the program was terminated due to mounting publication costs and production delays (Table 1). In all, MRS-3 was just shy of 4000 pages, not including the color quires. Volume 1 (version 1) *Platforms and Sensors* was released as a searchable CD-ROM in 1997. It described both airborne and space-borne platforms and sensor designs, and a brief description of their data collection and transmission parameters. It was modernized and released in hardcopy as MRS-3 volume 1.1 in 2009. Between 1997 and 2006, Volumes 2 through 6 were released and are available through ASPRS. Initially, the idea was to publish these as a series of thematic monographs on specific technologies and/or applications, each of which would be available at manageable cost to attract broader classroom use and avoid repeating earlier MRS content. The strategy of MRS-3 was to refresh MRS-2 sensor and application technologies in a series of thematic monographs. As it happened author/editors found that technologies were advancing on an upward curve and could be monitored on the World Wide Web while hard-copy publications were experiencing a downward spiral...close, but not close enough to the cutting edge. The unintended consequence was a long-delayed set of volumes that were increasingly too expensive for most of the intended market. Three volumes were published by Wiley Press, and three by ASPRS. Clearly, a different approach was needed. One interim approach was to retail books, or chapters of books, as downloadable PDFs (e.g., ASPRS's LiDAR Manual (Renslow, 2013)). Hardcopy text books are still a common denominator for classroom instruction; but updating text books to keep pace with technological advances is ever harder.

Table 1. MRS-3 Production Data.

Title	Copyright	Number of Pages	Principal Author/Editors
Vol. 1 Earth Observing Platforms & Sensors	ASPRS, 1997	CD-ROM	S.A. Morain & A.M. Budge
Vol. 2 Principles & Applications of Imaging Radar	Wiley, 1998	866 + color quire	F.M. Henderson & T.J. Lewis
Vol. 3 Remote Sensing for Earth Resources	Wiley, 1999	707 + color quire	A.N. Rencz
Vol. 4 Remote Sensing for Natural Resources and Environmental Monitoring	Wiley, 2004	736 + CD-ROM no color	S.L. Ustin
Vol. 5 Remote Sensing of Human Settlements	ASPRS, 2006	752 + color quire	M.K. Ridd & J.D. Hipple
Vol. 6 Remote Sensing of the Marine Environment	ASPRS, 2006	338 (including color)	J.F.R. Gower
Vol. 1.1 Platforms & Sensors	ASPRS, 2009	520 + color quire	M.W. Jackson

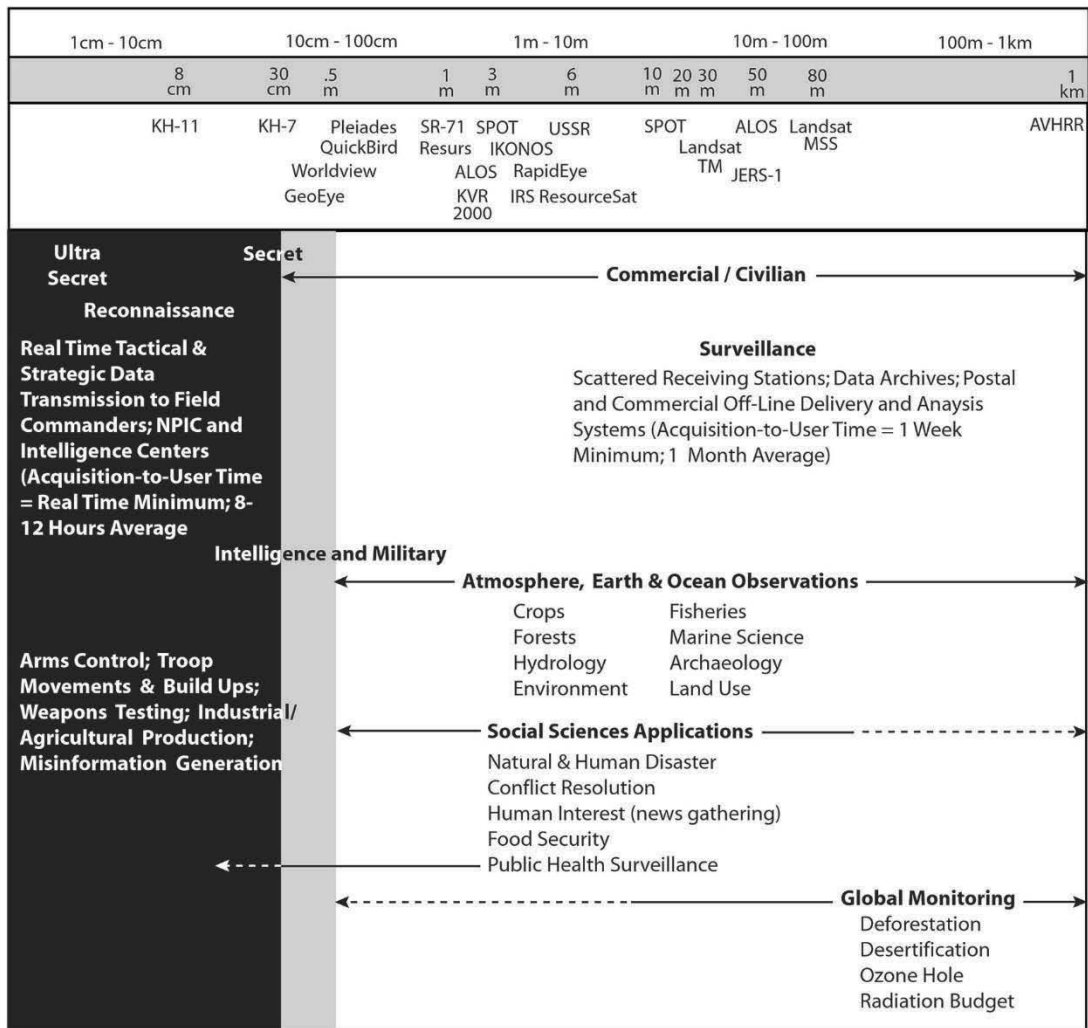


Figure 1. The range of social science applications expanded dramatically in the last decades of the 20th Century as system resolutions improved and were declassified. Compiled from data provided by Phillip Burrows, 1986, Deep Black: Space espionage and national security. New York: Random House.

MRS-4 was initiated in 2013. Headquarters' staff recruited an editorial team to create a more effective, affordable, and durable Manual, and to broaden its scope to include economic and societal benefits. *Effective* in the sense that MRS-4's content could be found online as an *enhanced e-book*; *affordable* in the sense that content could be retrieved by everyone on an annual subscription basis; and *durable* in the sense that it could be easily updated as a "living" manual through fresh, contributor-driven and vetted material as technologies advance. It does not reprise the extensive mathematical basis for remote sensing given in MRS-2, but instead focuses on system designs; data processing, storage, and retrieval; and on societal applications. A key feature of this concept is to facilitate timely updates of cutting edge or new developments from a wide spectrum of sophisticated contributors facile collectively with the technological, mathematical, and utilitarian aspects of Earth and space sciences. An example of these advances stemming from ever-finer spatial resolution is shown in Figure 1. Corresponding improvements in temporal and radiometric resolution also have contributed to the rapid expansion of Earth and Space applications.

MRS-4 is an enhanced *e-manual* available to the global community. The content is organized and compiled by chapter author/editors (A/Es) who are experts in their technical fields; and by contributors invited to develop topic-specific chapter elements. The overarching concept is that as an e-manual, MRS-4 should be updated as new subject matter and technological advances warrant. This implies that: (1) ASPRS maintains a mechanism for reviewing and vetting new and updated material submitted by contributors; and, (2) that this ongoing editorial process is flexible to accommodate new topics as well as revisions.

In future updates to MRS-4 a broader range of new and emerging remote sensing applications and results could be included such as data from in-situ sensors on the Moon, Mars, and perhaps including analysis of lunar samples and remote Martian samplers. These aims are ambitious in that most organizations like ASPRS, ISPRS and their international members (e.g., GEO, ICSU, UNESCO, and others) represent remote sensing communities-of-practice that rightly focus on Earth applications. But, there are other bodies like CEOS, a growing number of international space agencies, AIAA, and others that are ded-

icated also to solar system and astronomical research. These audiences also need sources of information that are produced by their peers and that are up-to-date and vetted. Consequently, the potential of MRS-4

will be realized when these other audiences become regular users of a self-perpetuating and self-refreshing information sources that are not tied to expensive re-publications every few years.

### **Acknowledgement**

ASPRS, the MRS-4 Editors-in-Chief, and Chapter Editors and their contributors acknowledge the generous support of the University of New Mexico, Earth Data Analysis Center, and Geography Department for providing office space, scanning devices, high speed printers, and communications equipment to generate the first version of MRS-4 as a “living electronic document.”

Stanley A. Morain

*Earth Data Analysis Center, University of New Mexico, Albuquerque, NM, USA*

Michael S. Renslow

*Renslow Mapping Services, Eugene, OR, USA*

Amelia M. Budge

*Earth Data Analysis Center, University of New Mexico, Albuquerque, NM, USA*

We hope you enjoyed this excerpt from *Manual of Remote Sensing, 4th Ed.* Stay tuned for more to come.

# Using Ranked Probability Skill Score (RPSS) as Nonlocal Root-Mean-Square Errors (RMSEs) for Mitigating Wet Bias of Soil Moisture Ocean Salinity (SMOS) Soil Moisture

Ju Hyoung Lee

## Abstract

To mitigate instantaneously evolving biases in satellite retrievals, a stochastic approach is applied over West Africa. This stochastic approach independently self-corrects Soil Moisture Ocean Salinity (SMOS) wet biases, unlike the cumulative density function (CDF) matching that rescales satellite retrievals with respect to several years of reference data. Ranked probability skill score (RPSS) is used as nonlocal root-mean-square errors (RMSEs) to assess stochastic retrievals. Stochastic method successfully decreases RMSEs from  $0.146 \text{ m}^3/\text{m}^3$  to  $0.056 \text{ m}^3/\text{m}^3$  in the Republic of Benin and from  $0.080 \text{ m}^3/\text{m}^3$  to  $0.038 \text{ m}^3/\text{m}^3$  in Niger, while the CDF matching method exacerbates the original SMOS biases up to  $0.141 \text{ m}^3/\text{m}^3$  in Niger, and  $0.120 \text{ m}^3/\text{m}^3$  in Benin. Unlike the CDF matching or European Centre for Medium-Range Weather Forecasts (ECMWF) Re-Analysis (ERA)-interim soil moisture, only a stochastic retrieval responds to Tropical Rainfall Measuring Mission rainfall. Based on the effects of bias correction, RPSS is suggested as a nonlocal verification without needing local measurements.

## Introduction

The quality of satellite-based soil moisture is important, particularly if used as an initialization for numerical weather prediction (NWP) or land surface models (Massey *et al.* 2016). However, satellite microwave sensors often produce large retrieval errors for various reasons (Gruhler *et al.* 2008; Zhu *et al.* 2019). In extremely dry soils, de Jeu *et al.* (2008) explain that the linear relationship between soil moisture and soil dielectric constant becomes invalidated, resulting in retrieval errors (Louvot *et al.* 2015). The linear relationship between microwave emission and soil moisture is also invalid in the event of rain (Dogusgen and Hornbuckle 2015). The presence of vegetation also contributes to retrieval errors, because vegetation attenuation underestimates brightness temperature, and it overestimates soil moisture as a consequence (Al-Yaari *et al.* 2014).

Although data assimilation is often used for error correction, it only reduces random errors. Thus, the cumulative density function (CDF) matching technique is widely used for reducing systematic errors in satellite retrievals. This approach rescales the CDF of satellite-derived soil moisture data with that of a long period of reference data. However, there are several limitations in that approach (Dee and Uppala 2009; Lee and Im 2015). First, CDF matching only considers stationary errors from 1–10 years of climatology, meaning that it does not mitigate retrieval errors that nonlinearly or abruptly evolve in every moment of satellite measurements (Reichle *et al.* 2007). However, the root-mean-square error

(RMSE) used for establishing the Soil Moisture Ocean Salinity (SMOS) and the Soil Moisture Active Passive retrieval goals indicates such instantaneous field of view (the angle over which a measurement is being made by an instrument in a single moment) satellite errors (Crow *et al.* 2012). CDF matching does not consider such retrieval errors made in an instant. However, instantaneous soil moisture data estimated in a specific time step is used for model initialization rather than time-averaged estimation. Secondly, CDF matching results may change, depending on the selection of reference data. When the satellite observations are rescaled to imperfect reference data, the original satellite observations can be exacerbated by its own biases of reference data (Muñoz-Sabater 2015). Considering that no perfect data exist, this aspect suggests that CDF matching inherently transfer biases.

For an alternative method, a Monte Carlo method is suggested in this study. Unlike deterministic retrievals of a single estimation, it uses a probability distribution function (PDF) for multiple retrievals. The statistical likelihood of optimal soil moisture values is determined from the mean value of the PDF (Kornelsen and Coulibaly 2013). A stochastic approach has been widely used for improving satellite-retrieved soil moisture (Lee and Im 2015; Lu and Gong 2012; Notarnicola, Angiulli, and Posa 2006; Pierdicca, Pulvirenti, and Big-nami 2010; Verhoest *et al.* 2007). That is because it resolves ill-posed retrieval problems with several unknown inputs, and enhances structural stability (Barabási and Albert 1999; Dhanya and Nagesh Kumar 2010; Lee and Ahn 2019).

However, none of those stochastic approaches introduced above has suggested a method to optimize PDFs (i.e., a reduction of RMSE in retrievals). In addition to computational costs (Parinussa *et al.* 2011), optimization is required for the purpose of bias correction. Not every PDF exhibits the correct estimation when taking an average. For example, if a spread of the PDF is not enough, the mean value of the PDF is biased. If the distribution is too wide, the mean of the PDF loses information of soil moisture dynamics. Although the field measurements-based RMSEs or biases are a local standard of verification, they do not cover the entire global domain that satellites operate. Thus, a nonlocal optimization of stochastic system is needed. Several studies in weather or climate models suggest an ensemble optimization via a ranked probability score (RPS) in that the ensemble method approximates the PDF by a finite set of multiple realizations (Dhanya and Nagesh

Photogrammetric Engineering & Remote Sensing  
Vol. 86, No. 2, February 2020, pp. 91–97.  
0099-1112/20/91–97

© 2020 American Society for Photogrammetry  
and Remote Sensing  
doi: 10.14358/PERS.86.2.91

Research Institute for Mega Construction, 145 Anam-ro,  
Seongbuk-gu, Korea University, Seoul, Republic of Korea  
(ju.lee@mail.com).

Kumar 2010; Jolliffe and Stephenson 2003; Weigel, Liniger, and Appenzeller 2007). RPS is considered as the CDF of a stochastic version. It compares the CDF of probabilistic estimates with that of a corresponding observation. In particular, Müller *et al.* (2005) states that rank probability skill score (RPSS) is the error metrics of a probabilistic version.

The objective of study is to stochastically mitigate SMOS overestimation that evolves at the time scale of several days and to investigate whether the RPSS can be a nonlocal measure for a stochastic retrieval instead of a local standard of RMSEs. In the section “Study Area and Satellite Data”, the study region and the satellite dataset are described. In the section “Methodology”, a stochastic retrieval method for satellite measurement is introduced along with the use of RPSS. The section “Results” presents local validations of stochastic retrievals with RMSEs and biases and compares its spatial distributions with other comparative data of ERA-interim and Tropical Rainfall Measuring Mission (TRMM) rainfall. The last section summarizes our conclusions.

### Study Area and Satellite Data

The study site is located in the sub-Saharan area at a longitude of 5–16 N and latitude of 10 W–10 E (Louvet *et al.* 2015). The Analyses Multidisciplinaires de la Mousson Africaine (AMMA) field campaign has been established in this region since 2006 for calibration and validation of satellite data (Cappelaere *et al.* 2009; Séguis *et al.* 2011). This study uses two stations located in Niger (13.5 N; 2.5 E) and Benin (9.5 N; 2 E). In 2010, eight probes per site were used for hourly measuring soil moisture at a soil depth of 5 cm. Niger in the Sahel region has bare soils in an extremely dry climate. In contrast, the Benin supersite has a moderate climate of the Guinean region covered with fallows or crops. More detailed description for a spatial upscaling of measurement instruments are previously described by Lee, Pellarin, and Kerr (2014).

The SMOS instrument measures microwave emission at an L-band (1.4 GHz) to produce brightness temperature data (e.g., SM\_REPR\_MIR\_SCLF1C) resampled on a 25 km EASEv2 grid. SMOS soil moisture retrievals were performed with L2SM Prototype Processor ver. 6.20 (Kerr *et al.* 2012). Detailed perturbation schemes for generating retrieval ensembles are provided by Lee & Ahn (2019) and Lee, Pellarin, and Kerr (2015). TRMM rainfall 3B24 [unit: mm/hrs, research version] was also used as comparative data for assessing soil moisture dynamics (Huffman *et al.* 2007; Lee 2018).

### MCM for Bias Correction

PDFs approximate the ensembles by multiple retrievals, instead of a single deterministic retrieval. It is referred to as retrieval ensembles in this study. To enhance structural stability, soil moisture ensembles were temporally integrated with other ensembles at adjacent days before and after the given day. Without integrations, the ensembles reduce biases when taking an average of ensembles. However, appropriate synthesis is more effective in terms of computational cost. In other words, the improved effects of bias correction are archived with a smaller sample size. For this ensemble synthesis, Jolliffe and Stephenson (2003) previously stated that combining more diverse ensembles increases structural stability and reliability. An optimal synthesis for ensembles is determined by RPSS, as described in the next section “Rank Probability Skill Score”.

After establishing the optimal ensembles with RPSS, the ensemble mean is used as bias-corrected estimation by MCM (Verhoest *et al.* 2007).

### Rank Probability Skill Score

Without integration of ensembles, the ensemble mean works for bias correction. However, the integration of ensembles saves computational costs, because it can achieve the effect of bias correction without increasing a sample number. It makes probabilistic retrievals more feasible in an operational mode. Question is how many days should be integrated. It is assessed by RPSS (Dhanya and Nagesh Kumar 2010; Müller *et al.* 2005). It quantifies the extent to which the stochastic retrieval ensembles improve upon the original SMOS soil moisture.

The RPS is estimated from the squared difference between the cumulative soil moisture ensembles and original SMOS product (Weigel, Liniger, and Appenzeller 2007), as follows:

$$RPS = (P - O)^2 \quad (1)$$

where P is the cumulative distribution function for the ensembles in the section “MCM for Bias Correction”, and O is an observation determined by the Heaviside function for the SMOS soil moisture given at the same time. Because observation event has no uncertain cases, it is considered as a deterministic binary system.

$$O = \begin{cases} 1 & \text{at SMOS observation} \\ 0 & \text{no observation} \end{cases} \quad (2)$$

Then, RPSS is shown as follows:

$$RPSS = 1 - \frac{\overline{RPS}}{RPS_{\text{clim}}} \quad (3)$$

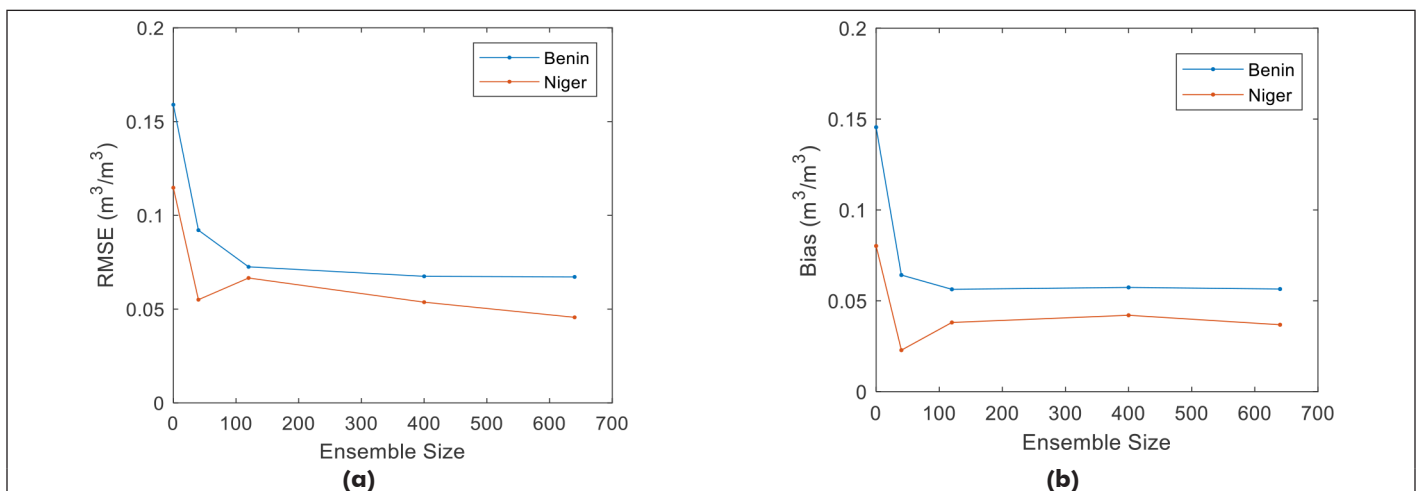


Figure 1. Performance of stochastic retrievals by ensemble size: (a) RMSE and (b) bias.

where  $\overline{RPS}$  is the mean for RPS in Equation 1, and  $\overline{RPS}_{clim}$  is the mean RPS between SMOS soil moisture and ERA-interim climatology data. An RPSS value of 1 implies a perfect estimate. A negative RPSS suggests that stochastic retrieval is worse than the climatology,  $RPS_{clim}$ . An RPSS of 0 indicates that the stochastic retrieval is no better than  $RPS_{clim}$ .

It is investigated whether it is possible to obtain an RPSS of 1 (i.e., perfect estimation) through appropriate ensemble synthesis. In other words, while increasing an ensemble size—i.e., by increasing the number of ensemble adjacent days from 40, 120, 400, to 640 days as discussed in the section “MCM for Bias Correction”, a change in RPSS values is examined. If an RPSS of 1 is obtained, then the ensemble mean is taken at that ensemble size. If an RPSS of 1 is not achieved, but RPSS is greater than 0.3 (Lee and Ahn 2019), then an ensemble size of 20 days is used as a threshold for calculating the ensemble mean. If RPSS is less than 0.3, a stochastic retrieval is not used. Instead, the original SMOS soil moisture is used for that case.

### CDF Matching

The stochastic approach proposed in this study is also compared to the CDF matching method. A year of ERA interim reanalysis soil volumetric water layer 1 data is used for the reference climatology, while original SMOS soil moisture product is used as observation data. For the shape of distribution, see Lee and Im (2015).

## Results

### RPSS as a Nonlocal Indicator for RMSEs

Figure 1a shows that the RMSEs and biases at the Benin location quickly decrease with ensemble size. However, beyond 120, there is no clear improvement in error metrics. In Niger, an ensemble size of 40 is found to be the optimal point, meaning that it reaches the best RMSEs and biases at low computational costs (i.e., the smallest ensemble size as much as possible), as shown in Figure 1b. Beyond this saturation point, the improvements in RMSEs and biases do not linearly increase with an ensemble size. Thus, the large ensemble size of 640 is a wasting of computational cost.

These optimal ensemble sizes are consistent with a nonlocal indicator of RPSS, as shown in Figure 2. As described in the section “Rank Probability Skill Score”, stochastic retrievals can be applied when RPSS is greater than 0.3 or unity. In this analysis, an RPSS of 1 is achieved at an ensemble size of 120 in Benin, and 40 in Niger, respectively. Because these

optimal ensemble sizes found from RPSS (Figure 2) are consistent with the RMSEs and biases (Figure 1), RPSS for a stochastic retrieval is suggested when nonlocal RMSEs on a spatial scale for field measurements are unavailable.

### Validation of Bias Correction at Local Point Scale

For time-series data, Figure 3a shows that a large SMOS overestimation is persistent in Benin during the entire experiment period. As shown in Figure 4a and Table 1, the original SMOS data present time-average RMSEs of  $0.159 \text{ m}^3/\text{m}^3$  and wet biases of  $0.146 \text{ m}^3/\text{m}^3$ . One of the reasons for this overestimation can be related to vegetation attenuation in Benin. As shown by Louvet *et al.* (2015), the site is covered with grass. In such a condition, vegetation attenuation underestimates brightness temperature and, as a consequence, overestimates soil moisture. The other factor to consider in Figure 3a is frequent rainfall events, during which a theoretical assumption of the retrieval algorithm is violated (Dogusgen and Hornbuckle 2015), resulting in nonlinear retrieval errors. This SMOS overestimation is slightly mitigated by CDF matching. In Figure 4a and Table 1, the time-average RMSEs of the original SMOS data decrease from  $0.159 \text{ m}^3/\text{m}^3$  to  $0.125 \text{ m}^3/\text{m}^3$ , while the biases diminish from  $0.146 \text{ m}^3/\text{m}^3$  to  $0.120 \text{ m}^3/\text{m}^3$ .

On the other hand, the SMOS overestimation is more effectively mitigated by stochastic retrievals (ensemble size: 120). In Figure 4a and Table 1, time-average RMSEs of original SMOS data dramatically decrease from  $0.159 \text{ m}^3/\text{m}^3$  to  $0.072 \text{ m}^3/\text{m}^3$ , while the biases diminish from  $0.146 \text{ m}^3/\text{m}^3$  to  $0.056 \text{ m}^3/\text{m}^3$ .

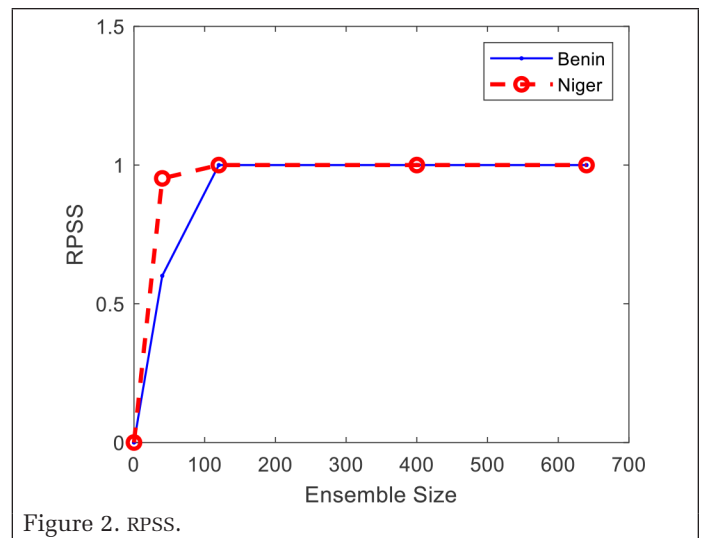


Figure 2. RPSS.

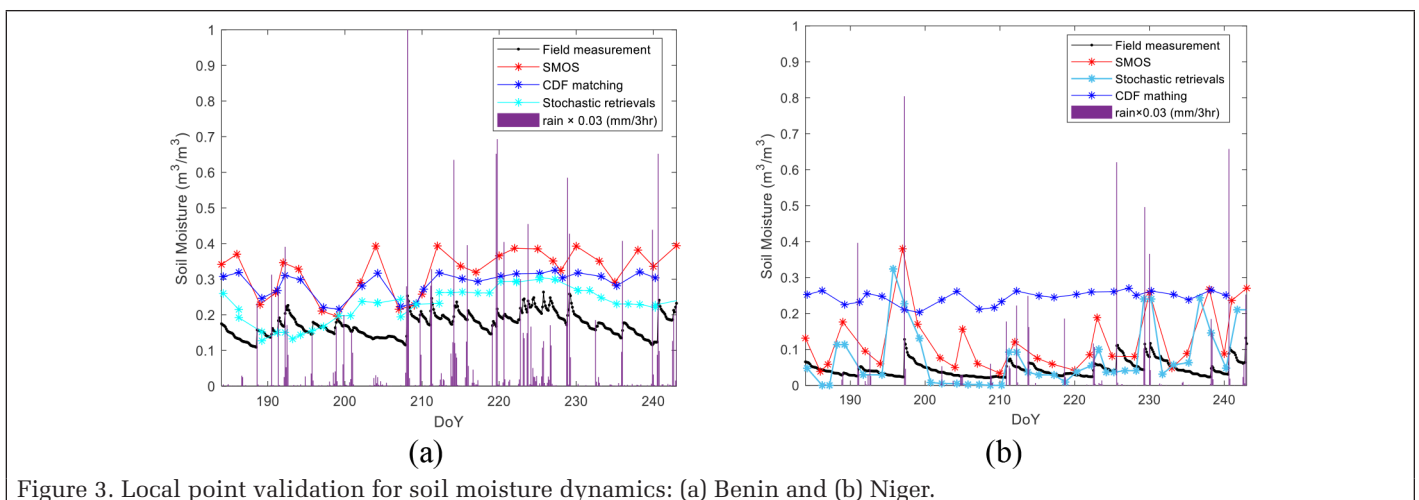


Figure 3. Local point validation for soil moisture dynamics: (a) Benin and (b) Niger.

m<sup>3</sup>. Simple explanation for how a stochastic system corrects biases is as follows. Wet biases of SMOS soil moisture produce ensembles with negative skewness. Negative skewness implies that the mode of the ensemble has higher values than the ensemble mean. By taking the ensemble mean, the estimation automatically shifts towards lower levels of soil moisture than the most frequently found median. Thus, taking an average of ensembles has the effect of bias correction.

Figure 3b also illustrates a SMOS overestimation in Niger. As shown in Figure 4b and Table 1, the time-average RMSE of original SMOS data is found at 0.115 m<sup>3</sup>/m<sup>3</sup>, while their wet bias is 0.080 m<sup>3</sup>/m<sup>3</sup>. This SMOS overestimation in Niger is unlikely due to rainfall events or vegetation attenuation, because the Niger site is characterized by bare soil and not much rain (Louvet *et al.* 2015). Rather, this may be because a linear assumption between the soil dielectric constant and the soil moisture becomes invalid at extremely low soil moisture contents (de Jeu *et al.* 2008).

However, such SMOS overestimation is largely alleviated by stochastic retrievals. In Figure 4b and Table 1, time-average RMSEs of original SMOS data dramatically decrease from 0.115 m<sup>3</sup>/m<sup>3</sup> to 0.067 m<sup>3</sup>/m<sup>3</sup>, while the biases diminish from 0.080 m<sup>3</sup>/m<sup>3</sup> to 0.038 m<sup>3</sup>/m<sup>3</sup>. In contrast, CDF matching increases retrieval errors in the original SMOS soil moisture. Specifically,

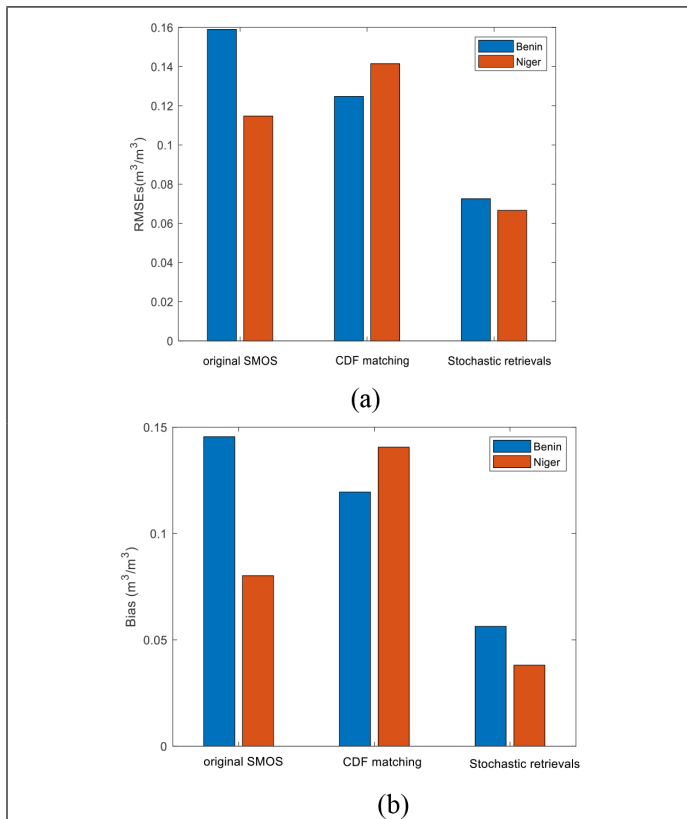


Figure 4. Local point validation for SMOS, CDF matching and stochastic methods: (a) time-average RMSEs, (b) time-average bias.

Table 1. Time-average error statistics in Figure 4.

	RMSE (m <sup>3</sup> /m <sup>3</sup> )		Bias (m <sup>3</sup> /m <sup>3</sup> )	
	Benin	Niger	Benin	Niger
SMOS data	0.159	0.115	0.146	0.080
CDF matching	0.125	0.142	0.120	0.141
Stochastic retrievals	0.072	0.067	0.056	0.038

the time-average RMSEs of the original SMOS data increase from 0.115 m<sup>3</sup>/m<sup>3</sup> to 0.142 m<sup>3</sup>/m<sup>3</sup>, while the biases dramatically worsen from 0.080 m<sup>3</sup>/m<sup>3</sup> to 0.141 m<sup>3</sup>/m<sup>3</sup>. This is possibly because CDF matching is contaminated by intrinsic errors in the reference data. The ERA-interim climatology reference data are used as input information of CDF matching. For the calculation of soil evaporation, their model sets the lower bound at wilting point (Balsamo *et al.* 2009). When soil moisture is sandy and dry below the wilting point as in Niger, the model data does not properly capture extremely low soil moisture, resulting in a large overestimation of CDF matching in this region.

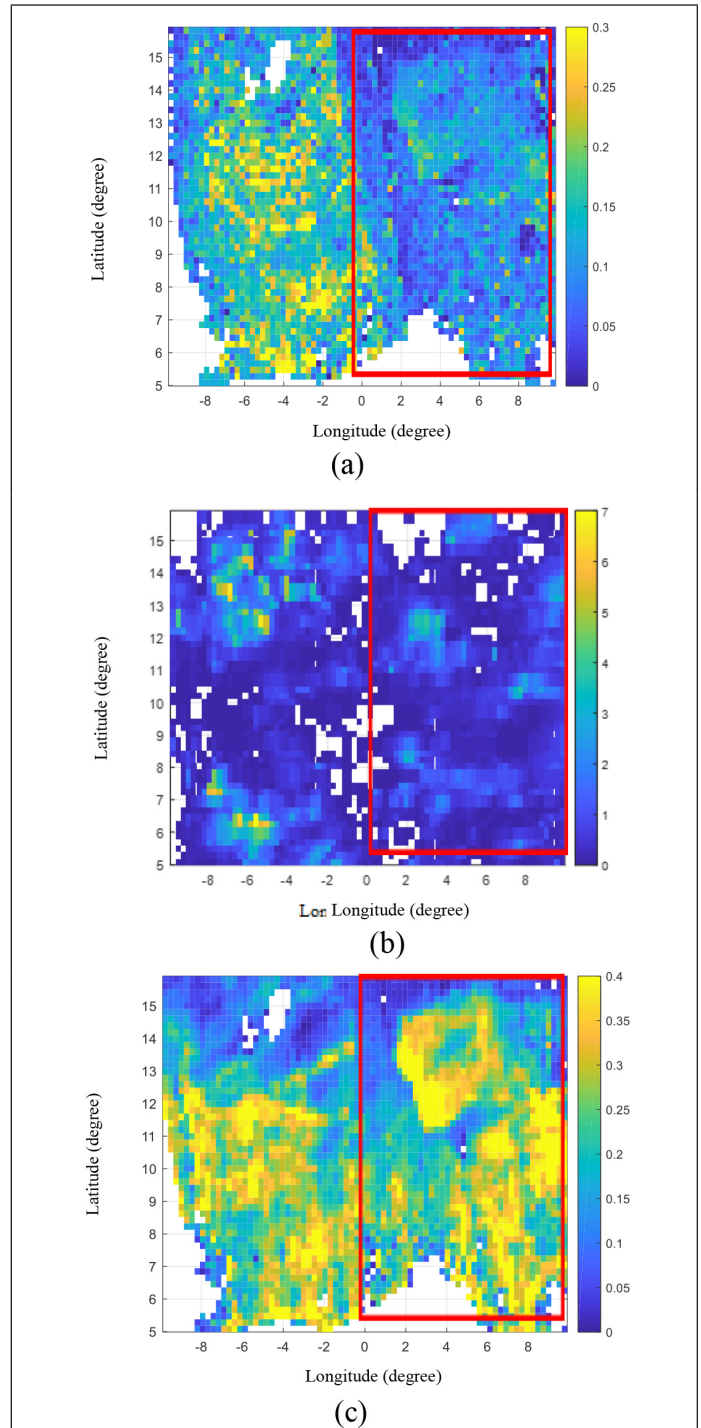


Figure 5. Spatial distribution of soil moisture (day of year (DoY) 196–197) in m<sup>3</sup>/m<sup>3</sup>: (a) stochastic method, (b) TRMM rainfall 3B24 [mm/hrs], (c) SMOS.

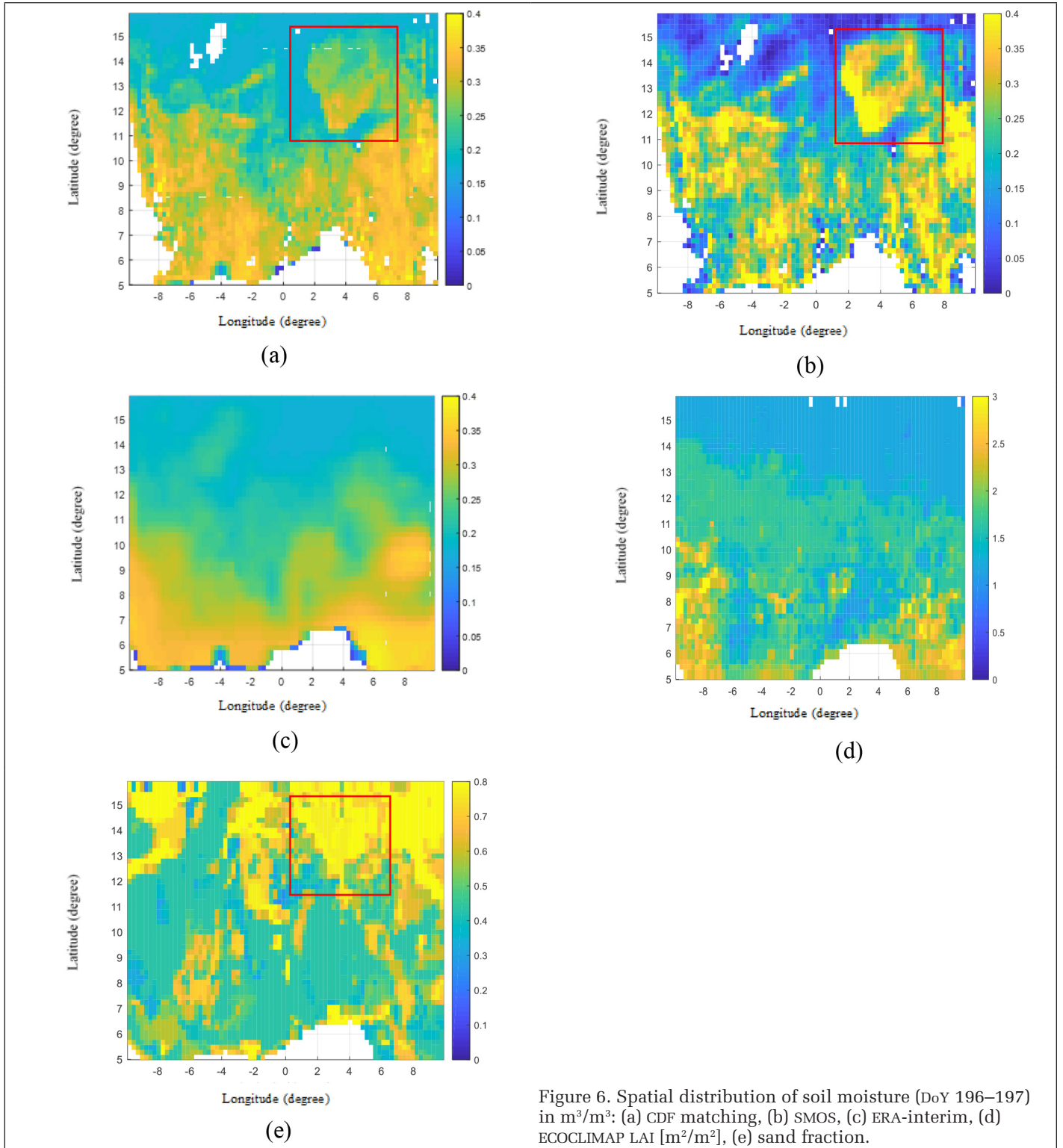


Figure 6. Spatial distribution of soil moisture (DoY 196–197) in  $\text{m}^3/\text{m}^3$ : (a) CDF matching, (b) SMOS, (c) ERA-interim, (d) ECOCLIMAP LAI [ $\text{m}^2/\text{m}^2$ ], (e) sand fraction.

In summary, although the SMOS overestimation in Benin is slightly reduced by CDF matching, a stochastic approach is more effective. In Niger, the RMSEs and biases of SMOS are exacerbated by CDF matching, implying that the CDF matching is adversely affected by the reference data that does not simulate extreme hydro-climatic conditions. This is a limitation of CDF matching. However, it is unavoidable, as all the models used for reference data rely on various assumptions and simplifications. Considering that no perfect reference data exists, it is a merit of a stochastic retrieval not to require the external data to compare with. A stochastic retrieval independently

self-corrects its own inherent biases with a probabilistic distribution; therefore, stochastic retrievals correct biases that were nonlinearly produced under extreme hydro-climatic conditions and that climate models neglect.

#### Spatial Dynamics

Figures 5–7 compare the spatial dynamics of several soil moisture data sets, where spatial dynamics is defined as temporal changes in a spatial pattern due to external forcing such as meteorological events or vegetation growth. The stochastic method is the only one showing a spatial distribution similar to the hourly dynamics of TRMM rainfall. More specifically,

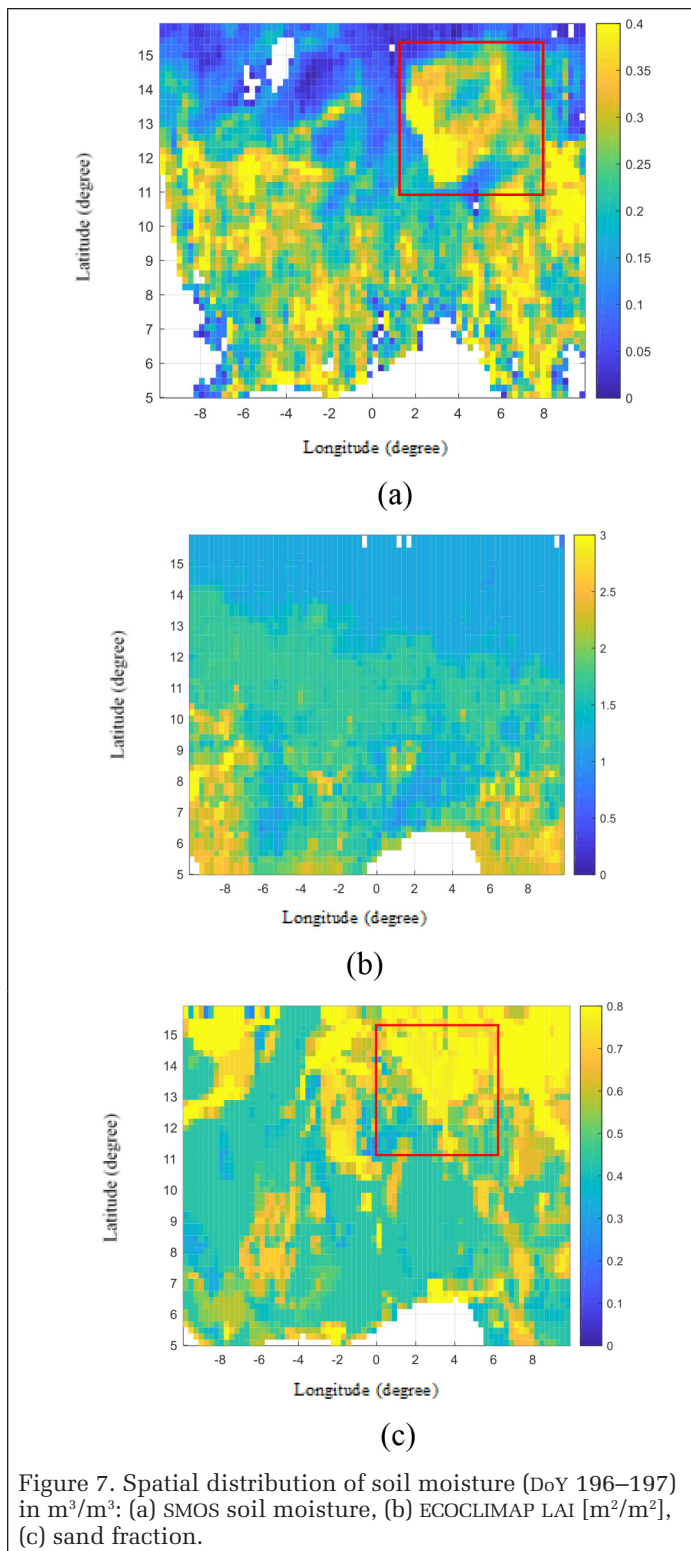


Figure 7. Spatial distribution of soil moisture (DoY 196–197) in  $\text{m}^3/\text{m}^3$ : (a) SMOS soil moisture, (b) ECOCLIMAP LAI [ $\text{m}^2/\text{m}^2$ ], (c) sand fraction.

the stochastic approach in Figure 5a captures the spatial and temporal features of hourly TRMM rainfall in Figure 5b, particularly around at a longitude of  $-8^\circ$  to  $-2^\circ$ . As shown by red box in Figure 5, it is also suggested that stochastic retrievals reduce the SMOS wet biases in Figure 5c.

On the contrary, in terms of latitudinal gradients, CDF matching shows the spatial and temporal features of the SMOS soil moisture and the ERA-interim, as both are the inputs for CDF matching. In Figure 6, CDF matching in Figure 6a mostly represents the spatially static feature of SMOS (red box in Figure 6b), and latitudinal gradients of ERA interim climatology

data in Figure 6c at a more slowly evolving time-scale. In SMOS retrieval algorithm, coarse sandy bare soils (red box in Figure 6e) tend to overestimate dielectric constant in comparison with clay at the same soil moisture, since free water in sandy soils increases the soil dielectric constant and soil moisture (de Jeu *et al.* 2008). However, if the site is covered with vegetation, it has also a large influence on CDF matching. Latitudinal gradient of CDF matching is similar to that of vegetation in Figure 6d. This may be related to the fact that the vegetation affects the soil moisture and evaporation representation in the land surface model of ERA interim (Balsamo *et al.* 2009).

Similar to CDF matching, the spatial distribution of SMOS soil moisture in Figure 7a follows more slowly evolving parameters such as LAI (Figure 7b) and soil texture (red box in Figure 7c) than hourly TRMM rainfall. As discussed above, the SMOS overestimation is related to vegetation attenuation (i.e., decrease in soil emission) or soil texture.

Taken together, the spatial average of CDF matching shows the highest estimate at  $0.261 \text{ m}^3/\text{m}^3$ , while the ERA-interim is  $0.246 \text{ m}^3/\text{m}^3$ . It is followed by the spatial average of SMOS at  $0.2315 \text{ m}^3/\text{m}^3$ . The lowest spatial average is found to be stochastic retrievals at  $0.1217 \text{ m}^3/\text{m}^3$ . It is suggested that a stochastic retrieval mitigate wet biases in extremely dry conditions, for example, below wilting point as in Niger.

## Conclusions

In this study, a generalized procedure for stochastic retrievals of soil moisture is provided. This aims to reduce the instantaneous SMOS wet biases evolving at time scale of several days instead of climatology errors accumulating several years. To determine applicability of a stochastic retrieval, RPSS is suggested. If RPSS indicates no improvement in estimating soil moisture, it is better to use the original SMOS soil moisture product. Local field measurements are not required for the use of RPSS so that this approach has the potential to be applied globally. Thus, RPSS is suggested as a substitute for nonlocal RMSEs.

In addition, this stochastic approach self-corrects its own intrinsic biases so that it is not contaminated by errors in reference data. In contrast, as the reference data in CDF matching are not able to capture hydro-climatic extreme conditions (e.g., soil moisture below a wilting point), CDF matching results are also influenced by biases of reference. Finally, the stochastic retrievals mitigate instantaneously evolving errors, as compared to climatology data such as the ERA-interim that accumulates several years. Unlike the SMOS soil moisture, CDF matching and ERA-interim data that respond to static parameters such as soil texture or monthly evolving vegetation dynamics, the stochastic approach responds to hourly rainfall dynamics, and mitigates SMOS overestimation.

Future work may include the application of this approach to near-real-time soil moisture products. It is also our interest to expand the application of this approach to other sites in different soil and vegetation conditions.

## Acknowledgments

This research was supported by the National Research Foundation of Korea (NRF-2018R1D1A1B07048817, 2015R1C1A1A02037224). We also thank “Centre Aval de Traitement des Données SMOS” (CATDS) operated for the “Centre National d’Etudes Spatiales” (CNES, France) by IFREMER (Brest, France), and Y. Kerr for helping SMOS analysis, and V. Maggioni for helping TRMM data description. We greatly thank all data providers that kindly shared their data with the ISMN: Thierry Pellarin (AMMA).

## References

- Al-Yaari, A., J. P. Wigneron, A. Ducharne, Y. H. Kerr, W. Wagner, G. De Lannoy, R. Reichle, A. Al Bitar, W. Dorigo, P. Richaume and A. Mialon. 2014. Global-scale comparison of passive (SMOS) and active (ASCAT) satellite based microwave soil moisture retrievals with soil moisture simulations (MERRA-Land). *Remote Sensing of Environment* 152:614–626.
- Balsamo, G., A. Beljaars, K. Scipal, P. Viterbo, B. van den Hurk, M. Hirschi and A. K. Betts. 2009. A revised hydrology for the ECMWF model: Verification from field site to terrestrial water storage and impact in the integrated forecast system. *Journal of Hydrometeorology* 10:623–643.
- Barabási, A.-L. and R. Albert. 1999. Emergence of scaling in random networks. *Science* 286:509.
- Cappelaere, B., L. Descroix, T. Lebel, N. Boulain, D. Ramier, J. P. Laurent, G. Favreau, S. Boubkraoui, M. Boucher, I. Bouzou Moussa, V. Chaffard, P. Hiernaux, H. B. A. Issoufou, E. Le Breton, I. Mamadou, Y. Nazoumou, M. Oi, C. Otlé and G. Quantin. 2009. The AMMA-CATCH experiment in the cultivated Sahelian area of south-west Niger—Investigating water cycle response to a fluctuating climate and changing environment. *Journal of Hydrology* 375:34–51.
- Crow, W. T., A. A. Berg, M. H. Cosh, A. Loew, B. P. Mohanty, R. Panciera, P. Rosnay, D. Ryu and J. P. Walker. 2012. Upscaling sparse ground-based soil moisture observations for the validation of coarse-resolution satellite soil moisture products. *Reviews of Geophysics* 50.
- de Jeu, R. A. M., W. Wagner, T. R. H. Holmes, A. J. Dolman, N. C. van de Giesen and J. Friesen. 2008. Global soil moisture patterns observed by space borne microwave radiometers and scatterometers. *Surveys in Geophysics* 29:399–420.
- Dee, D. P. and S. Uppala. 2009. Variational bias correction of satellite radiance data in the ERA-Interim reanalysis. *Quarterly Journal of the Royal Meteorological Society* 135:1830–1841.
- Dhanya, C. T. and D. Nagesh Kumar. 2010. Nonlinear ensemble prediction of chaotic daily rainfall. *Advances in Water Resources* 33:327–347.
- Dogusgen, C. and B. K. Hornbuckle. 2015. A non-linear relationship between terrestrial microwave emission at 1.4 GHz and soil moisture caused by ponding of water. *Remote Sensing Letters* 6:238–246.
- Gruhier, C., P. de Rosnay, Y. Kerr, E. Mougin, E. Ceschia, J.-C. Calvet and P. Richaume. 2008. Evaluation of AMSR-E soil moisture product based on ground measurements over temperate and semi-arid regions. *Geophysical Research Letters* 35.
- Huffman, G. J., D. T. Bolvin, E. J. Nelkin, D. B. Wolff, R. F. Adler, G. Gu, Y. Hong, K. P. Bowman and E. F. Stocker. 2007. The TRMM multisatellite precipitation analysis (TMPA): Quasi-Global, multiyear, combined-sensor precipitation estimates at fine scales. *Journal of Hydrometeorology* 8:38–55.
- Kerr, Y., P. Waldteufel, P. Richaume, J.-P. Wigneron, P. Ferrazzoli, A. Mahmoodi, A. Al Bitar, F. Cabot, C. Gruhier, S. E. Juglea, D. Leroux, A. Mialon and S. Delwart. 2012. The SMOS soil moisture retrieval algorithm. *IEEE Transactions on Geoscience and Remote Sensing* 50 (5):1384–1403. <<http://dx.doi.org/10.1109/TGRS.2012.2184548>>.
- Kornelsen, K. and P. Coulibaly. 2013. Advances in soil moisture retrieval from synthetic aperture radar and hydrological applications. *Journal of Hydrology* 476:460–489.
- Lee, H. J. and J. Im. 2015. A novel bias correction method for soil moisture and ocean salinity (SMOS) soil moisture: Retrieval ensembles. *Remote Sensing* 7.
- Lee, J. H. 2018. The consecutive dry days to trigger rainfall over West Africa. *Journal of Hydrology* 556:934–943.
- Lee, J. H. and C. K. Ahn. 2019. Stochastic relaxation of nonlinear soil moisture ocean salinity (SMOS) soil moisture retrieval errors with maximal Lyapunov exponent optimization. *Nonlinear Dynamics* 95:653–667.
- Lee, J. H., T. Pellarin and Y. H. Kerr. 2014. Inversion of soil hydraulic properties from the DEnKF analysis of SMOS soil moisture over West Africa. *Agricultural and Forest Meteorology* 188:76–88.
- Lee, J. H., T. Pellarin and Y. H. Kerr. 2015. EnOI optimization for SMOS soil moisture over West Africa. *IEEE Journal of Selected Topics in Applied Earth Observations and Remote Sensing* 8:1821–1829.
- Louvet, S., T. Pellarin, A. al Bitar, B. Cappelaere, S. Galle, M. Grippa, C. Gruhier, Y. Kerr, T. Lebel, A. Mialon, E. Mougin, G. Quantin, P. Richaume and P. de Rosnay. 2015. SMOS soil moisture product evaluation over West-Africa from local to regional scale. *Remote Sensing of Environment* 156:383–394.
- Lu, H. and P. Gong. 2012. Multi-algorithm ensemble reconstruction of surface soil moisture over China from AMSR-E. Pages 718–721 in *Proceedings of the 2012 IEEE International Geoscience and Remote Sensing Symposium*.
- Massey, J. D., W. J. Steenburgh, J. C. Knievel and W. Y. Y. Cheng. 2015. Regional soil moisture biases and their influence on WRF model temperature forecasts over the Intermountain West. *Weather and Forecasting* 31:197–216.
- Müller, W. A., C. Appenzeller, F. J. Doblas-Reyes and M. A. Liniger. 2005. A debiased ranked probability skill score to evaluate probabilistic ensemble forecasts with small ensemble sizes. *Journal of Climate* 18:1513–1523.
- Muñoz-Sabater, J. 2015. Incorporation of passive microwave brightness temperatures in the ECMWF soil moisture analysis. *Remote Sensing* 7.
- Notarnicola, C., M. Angiulli and F. Posa. 2006. Use of radar and optical remotely sensed data for soil moisture retrieval over vegetated areas. *IEEE Transactions on Geoscience and Remote Sensing* 44:925–935.
- Parinussa, R. M., A. G. C. A. Meesters, Y. Y. Liu, W. Dorigo, W. Wagner and R. A. M. de Jeu. 2011. Error estimates for near-real-time satellite soil moisture as derived from the land parameter retrieval model. *IEEE Geoscience and Remote Sensing Letters* 8:779–783.
- Pierdicca, N., L. Pulvirenti and C. Bignami. 2010. Soil moisture estimation over vegetated terrains using multitemporal remote sensing data. *Remote Sensing of Environment* 114:440–448.
- Reichle, R. H., R. D. Koster, P. Liu, S. P. P. Mahanama, E. G. Njoku and M. Owe. 2007. Comparison and assimilation of global soil moisture retrievals from the advanced microwave scanning radiometer for the Earth observing system (AMSR-E) and the scanning multichannel microwave radiometer (SMMR). *Journal of Geophysical Research: Atmospheres* 112.
- Séguis, L., N. Boulain, B. Cappelaere, J. M. Cohard, G. Favreau, S. Galle, A. Guyot, P. Hiernaux, É. Mougin, C. Peugeot, D. Ramier, J. Seghier, F. Timouk, V. Demarez, J. Demarty, L. Descroix, M. Descloîtres, M. Grippa, F. Guichard, B. Kamagaté, L. Kergoat, T. Lebel, V. Le Dantec, M. Le Lay, S. Massuel and V. Trichon. 2011. Contrasted land-surface processes along the West African rainfall gradient. *Atmospheric Science Letters* 12:31–37.
- Jolliffe, I. T. and D. B. Stephenson, eds. 2003. *Forecast Verification: A Practitioner's Guide in Atmospheric Science*. Ian T. Jolliffe (Editor), David B. Stephenson (Editor)
- Verhoest, N. E. C., B. De Baets, F. Mattia, G. Satalino, C. Lucau and P. Defourny. 2007. A possibilistic approach to soil moisture retrieval from ERS synthetic aperture radar backscattering under soil roughness uncertainty. *Water Resources Research* 43.
- Weigel, A. P., M. A. Liniger and C. Appenzeller. 2007. The discrete brier and ranked probability skill scores. *Monthly Weather Review* 135:118–124.
- Zhu, L., J. P. Walker, N. Ye and C. Rüdiger. 2019. Roughness and vegetation change detection: A pre-processing for soil moisture retrieval from multi-temporal SAR imagery. *Remote Sensing of Environment* 225:93–106.

## Optical Polarization Remote Sensing & Photogrammetry

Light is an electromagnetic wave vector and its wave equation of scalar propagation has four basic parameters: amplitude, frequency, phase and polarization. The polarization signal is usually ignored, and the remaining three parameters provide the physical basis of the four major resolutions (radiometric, spectral, spatial and temporal) of optical remote sensing. Nevertheless, polarization, which refers to the asymmetry of the light vibration, provides key information for studying the properties of materials.

More than 30 years of work has resulted in a science of polarization remote sensing (PoIRS). PoIRS includes the underlying physical theories, measurement instruments, including precision detection technology, and analytical approaches for studying polarization in imagery. The general conclusion of this research is that including the polarization signal in optical remote sensing images (such as hyperspectral or infrared images) can increase the contrast ratio by 2–3 orders of magnitude for mapping snow and ice, water quality, environmental pollution, rock density and roughness, oil spills, vegetation biomass, air pollution particle detection and atmospheric attenuation applications. Thus, PoIRS offers a unique detection capability.

This special issue seeks papers on all aspects of optical polarization remote sensing science and technology, including theory, technology and applications.

### How to Submit your Manuscript

All submissions will be peer reviewed according to the Photogrammetric Engineering and Remote Sensing (*PE&RS*) guidelines. Submitted manuscripts should not have been published or be under review elsewhere.

Prospective authors should consult the *PE&RS* Instructions for Authors on the journal homepage for guidelines and information on paper formatting and submission.

Authors should submit manuscripts using the *PE&RS* manuscript central system at <https://www.editorialmanager.com/asprs-pers/default.aspx>. Please choose '**PE&RS Special Issue Paper**' from the 'Manuscript Type' picklist on the submission form, irrespective of the paper type (i.e. even if your paper would normally be classified as a Research Letter, Tech Note, Research Paper, or Review Article). Also, please enter "**Polarization**" in the space provided on the submission form for the name of the special issue.

Should you have any submission questions, please [PERSEditor@asprs.org](mailto:PERSEditor@asprs.org).

### Important Dates

Deadline for the submission of contributions: **March 20, 2020**

Expected print publication date: **Late 2020**

Articles will be available online after acceptance, final technical review and the completion of revisions for compliance with journal format. However, the paper copy of the special issue will be published only when all papers are accepted.

If you have any specific questions about the special issue, please contact the editorial team listed below.

### Editorial information

#### Editorial Team:

- Lei Yan, Peking University, China, [lyan@pku.edu.cn](mailto:lyan@pku.edu.cn)
- Jouni Peltoniemi, Finnish Geospatial Research Institute (FGI), Finland, [jouni.peltoniemi@nls.fi](mailto:jouni.peltoniemi@nls.fi)

# Economy Estimation of Mainland China at County-Level Based on Landsat Images and Multi-Task Deep Learning Framework

Bo Yu, Ying Dong, Fang Chen, Yu Wang

## Abstract

*The social-economic statistics collected from local governments are the main access for the central government to achieve national economic circumstance, especially for China. However, the statistics of almost 10% of national counties are missing or inconsistent due to the statistical caliber change in the wave of urbanization during economic development. Some researchers proposed to apply a night luminosity product to solve such issue. However, it lacks the ability to distinguish between the wealthy populations with a dense distribution and the less developed places. In this paper, the publicly available daytime Landsat images are used to estimate economic statistics. An end-to-end multi-task deep learning framework is constructed to estimate the county-level economy of Mainland China and the overall accuracy of this model achieves higher than 85%. The experiments show that our model provides a potential strategy to make up for the missing statistics and examines the reliability of the statistics collected for the central government.*

## Introduction

Data, which have penetrated into all walks of life, have become an important factor that drives production in our study, work, life, and social development. Socioeconomic data, especially in economy, education, and agriculture, are the key factors in measuring development level (Cheng *et al.* 2018). With well-documented socioeconomic data, governments can make accurate evaluations and predictions, and put forward reasonable policies to ensure rational allocation of public resources to realize the more balanced and full development goal especially under the unstable social and economic situation. Moreover, detailed data record supplements international researchers or institutions to understand economic status of different places from different aspects (Puzo, Mehlum, and Qin 2018). Despite the significant work in collecting data,

---

Bo Yu and Fang Chen are with Key Laboratory of Digital Earth Science, Institute of Remote Sensing and Digital Earth, Chinese Academy of Sciences, Beijing 100094, China (chenfang@radi.ac.cn).

Fang Chen is also with Hainan Key Laboratory of Earth Observation, Institute of Remote Sensing and Digital Earth, Chinese Academy of Sciences, Sanya 572029, China.

Fang Chen is also with the University of Chinese Academy of Sciences, Beijing 100049, China.

Ying Dong is with the College of Economics and Management, South China Agricultural University, Guangzhou 510642, China. Yu Wang is with the Beijing Twenty-First Century Science & Technology Development Co., Ltd., Beijing 100096, China. Yu Wang is also with the School of Electronics and Information Engineering, Harbin Institute of Technology, Harbin 150001, China.

improving data quality, and distributing data, actions mobilized by global governments, companies, and researchers, there are still many places suffering from a lack of socioeconomic data or the lack of accessibility to the data (Ieag 2014). Such inaccessibility hinders objective economy analysis for the developing or undeveloped places, which should have needed more resources or pertinent strategies to grow.

China has spent billions of U.S. dollars to collect and share data collected by different departments of the government (Li and James 2015). The quantity and quality of economic data available in China have improved steadily, but continuous and complete data on key measurements of economic situations are still missing to some degree (Lo 2016). In addition, there is a data inconsistency problem due to statistical caliber and standard change during economic development (Liu *et al.* 2016). The data gaps are hampering efforts to identify and understand variation in these outcomes and target intervention effectively to areas of greatest need (Wei and Zhang 2013; Yu and Jin 2016).

Moreover, the data gaps in China's county economic data are particularly constraining (Tao *et al.* 2015). The Chinese County Statistical Yearbook covers annual detailed macro-economic statistics in comprehensive economy, agriculture, industry, and education for more than 2000 counties of mainland China except for prefecture-level cities (Dong *et al.* 2016). However, the macro-economic statistics do not involve all the counties. Almost 10% of the national counties do not have statistics. On the other hand, due to the issue of statistical caliber, some statistics deviate from the reality (Wang 2015). The collection of county economic data in China relies on the statistical demand of the research hotspot and urbanization degree. The statistical caliber of county economy indicators is inconsistent because of the frequent data update and modification of urban and rural population classification standards in the census (Wang 2015). In addition, it is especially difficult for the current statistical caliber to take China's "semi-urbanization" phenomenon into account, which is mainly occurring in Central China. Central China is a typical place where villages are being withdrawn and the corresponding towns are being established with different versions of statistical calibers (Pan, Wei, and Wang 2015). However, consistent county-level economic data are crucial in economic prediction and policy making process under the large-scale population flow as well as the urban-rural integration development (Friedmann 2005; Wang 2006; Zhang 2011). Therefore, it is urgent to find an objective way to fill in the missing data and correct the inconsistent statistics collected.

---

Photogrammetric Engineering & Remote Sensing  
Vol. 86, No. 2, February 2020, pp. 99–105.  
0099-1112/20/99–105

© 2020 American Society for Photogrammetry  
and Remote Sensing  
doi: 10.14358/PERS.86.2.99

Owing to the development of technology, the difficulties of traditional collecting and sharing data can be overcome by means of third-party media, such as satellites and mobile phones (Blumenstock, Cadamuro, and On 2015; Chen and Nordhaus 2011; Jean *et al.* 2016). The popularization of mobile phones around the world makes it possible to collect human behavior data to estimate poverty locally and nationally. However, the model is difficult to scale into other countries and the collection is difficult to repeat as well, since it requires local survey and necessary funding. Satellites provide a stable avenue to collect data and luminosity at night is a widely used product to estimate economic statistics, including poverty, population, and gross domestic product (Chen and Nordhaus 2011; Jean *et al.* 2016). However, the simulation results show that luminosity data are still difficult to distinguish between the places with densely distributed population but wealthy and the places less developed. Recent studies are seeking methods to combine daytime and nighttime satellite images to estimate social economy, such as the works done by Jean *et al.* (2016). Their model can explain up to 75% variance at local-level economic output, but the input high spatial resolution images of the model are drawn from Google Static Maps application programming interface. That requires the access to Google, which is forbidden in several countries, such as China. Moreover, the proposed model is a multi-step transfer-learning framework, which is not convenient to apply in other cases.

In this paper, we aim to introduce an end-to-end workflow to fill in the missing data and correct the inconsistent data and then apply this model to estimate Chinese mainland socioeconomic features. The workflow is a multi-task deep learning framework, which is composed of two tasks. One task is to extract socioeconomic features from publicly available midresolution daytime satellite images to mimic luminosity data and the other task is to estimate and to examine its estimation accuracy using county-level comprehensive economic index by learning features from the same midresolution images. We apply the proposed model to the publicly released statistics from the Chinese county statistical yearbook. Moreover, to show the potential application of this method, we also apply this model to estimate the composite economic index including welfare indicators. The main difference of our method from others is that data adopted in our method are publicly accessible from the public internet, and the proposed method has strong applicability and convenience to apply in other countries, since it is single-model based. Furthermore, in spite of estimating economic statistics for counties that lack data, we also validated the veracity of the statistics.

The introduction of data used in our study is described in the following part. Our multi-task deep learning based economic index calculation model, results, discussion and conclusion are given respectively after that.

## Data Introduction

Our study is conducted using the data from year 2009, which is believed to represent the Chinese county economy status after the global financial crisis happened in 2008. Therefore, with such data, mainland China's economic situation after the financial crisis can be evaluated through the county where most township and village enterprise distributed and agglomerated due to local fiscal incentives and industrial transfer (Li and James 2015; Teng, Hu, and Hou 2016). In details, the data used in our study comprise Landsat images, luminosity images, and Chinese county statistical yearbook, which are described as follows.

## Luminosity Images

The Defense Meteorological Satellite Program/Operational Linescan System (DMSP/OLS) provides a time series product of nighttime lights from the year 1992 with a resolution of 30 arc second. The annual products are publicly available, covering 65°S–75°N and 180°E–180°W (NGDC 2013).<sup>1</sup> There are three types of images in the product, cloud-free total observations (*cf\_cvgt*), average visible band digital number without processing (*avg\_vis*), and cleaned up average visible band digital number (*stable\_lights.avg\_vis*). The cleaned up product records stable light observations after removing background noise, such as fires. Our study is based on the cleaned up nighttime light product. However, nighttime light has difficulty in distinguishing between poor but densely populated areas and wealthy but sparsely populated areas (Chen and Nordhaus 2011; Jean *et al.* 2016). Therefore, we use the nighttime light product as a supplementary to improve our economic index calculation model.

## Landsat Images

Thanks to the Landsat program, Landsat images keep the longest record of earth from satellite since 1972, when the first Earth Resources Technology Satellite was launched (Short 1982). There have been eight Landsat satellites launched to acquire global imagery one after another. The images are publicly available from the U.S. Geological Survey (USGS) Earth Explorer.<sup>2</sup> Since our study is conducted in year 2009, Landsat 7 images are used. Landsat 7 has a spatial resolution from 15 m to 60 m with eight spectral bands, and its temporal resolution is 16 days. Moreover, the Landsat 7 images we used are synthesized from the annual Landsat 7 time series images in year 2009 with a spatial resolution of 30 m. The intensity of each pixel of the synthesized image is achieved by selecting the largest intensity from all the pixels of the same location in the band of near-infrared throughout the annual Landsat 7 time series images. This selection works because the multiple ground objects are easily distinguished from each other in summer, when vegetation turns green, which gets high intensity in the band of near-infrared. The synthesized Landsat 7 image has six spectral bands including, the blue, green, red, near-infrared, mid-infrared, and thermal infrared band, which are sensitive to various characteristics of different ground objects. It can better capture economic variation among wealth sparse distributed areas and poorer clusters by providing more detailed ground object information for economic index estimation (Chen and Nordhaus 2011, Jean *et al.* 2016).

## Chinese County Statistical Yearbook

To examine the estimation accuracy of our model, the Chinese county statistical yearbook is also used.<sup>3</sup> It comprehensively reflects the social and economic situation of a Chinese county, and is collected by the Department of Rural Social and Economic Investigation Division of the Chinese Bureau of Statistics. Specifically, the statistical yearbook covers basic information, comprehensive economy, agriculture, industry, education, health, and social security of 2053 counties. Of all the counties, almost 10% are missing the statistics in both socioeconomic indices. This motivates our research to fill up the voids. Moreover, during the tide of urbanization, many villages in Central China are being withdrawn and counties are being established (Pan, Wei, and Wang 2015). The statistical caliber may change during the tide and the corresponding statistics recorded in the yearbook may deviate from the reality. Therefore, the inconsistent county economic statistics are left out as outliers to validate the reliability of the collected statistics.

1. <https://ngdc.noaa.gov/eog/dmsp/downloadV4composites.html>.

2. <https://earthexplorer.usgs.gov/>.

3. <http://www.tjcn.org/tjnj/XXX/35826.html>.

In our work, to evaluate the applicability of our method in indicating China's economic situation after financial crisis and the sustainability of China's future economic development considering welfare, we analyze the statistics from two perspectives; one is in terms of comprehensive economy, and the other is composite economic indices considering welfare indicators in education, healthcare, and old-age service. These additional composite economic indices indicate the three dimensions of intelligence, physical power, and family resources buttress concerning human being welfare and even the sustainability for future economy development (Mackenbach 2012; Rindermann 2008; Wong 2008). The indices of comprehensive economy (CEI) and composite economy index including welfare (WCEI) are calculated respectively. For each perspective analysis, we calculated the first principle component on the corresponding statistics from Chinese county statistical yearbook as the corresponding economic index and the lacked statistics of the counties are assigned zero. It needs to point out that the calculated socioeconomic indices are rescaled to 0–255 for the convenience to illustrate and categorize the economic level for each county.

### Multi-Task Deep Learning Based Economic Index Calculation Model

Multi-task learning is a learning framework that shares representations among related tasks. It has achieved significant progress in many applications that machine learning can involve (Csaplovics 2003; Deng, Hinton, and Kingsbury 2013; Girshick 2015; Ramsundar *et al.* 2015; Yu and Lane 2014). A typical multi-task learning framework comprises a main task and an auxiliary task, as shown in Figure 1. Each task has a loss function. The main task is our main target to learn and auxiliary task contains the related information with the main target. There is a large quantity of literature concluding that multi-task learning can be a way to augment sample size by training two tasks simultaneously, coping with limited amount of supervised labeled training samples by providing other supervised but non semantic training examples (Baxter 2000; Caruana 1998).

Recent advances of deep learning (LeCun, Bengio, and Hinton 2015) in computer vision have promoted rapid progress in other applications, such as remote sensing (Zhang, Zhang, and Du 2016) and medical image processing (Litjens *et al.* 2017). The advances owe to the development of convolutional neural network, which learns local spatial relationships of images by a set of convolution filters. The convolutional layers are followed by nonlinear active functions and down sampling to capture hierarchical features. Based on convolutional neural networks, several typical network structures, such as ResNet (He *et al.* 2016) and Inception architectures (Szegedy *et al.* 2017), are developed and show landmark performances in the annual Large Scale Visual Recognition Competition using the largest image data set ImageNet (Russakovsky *et al.* 2015).

The main issue of deep learning application is a requirement of huge amounts of training data. It is hard to meet in our case, because the collected economic statistics cannot cover all the counties, so the quantity of economic statistics is less than 2000. To deal with such a challenge, we propose a multi-task deep learning model to estimate the economic statistics at pixel-level based on satellite images. The multi-task deep learning model (see Figure 2) consists of four tasks, one main task, and three auxiliary tasks. The main task is to calculate CEI and WCEI, and each of the three auxiliary tasks is to extract contextual features from daytime Landsat images by mimicking luminosity data. The auxiliary tasks are trained simultaneously with main task. The layers labeled as green in Figure 2 are shared layers between auxiliary tasks and main

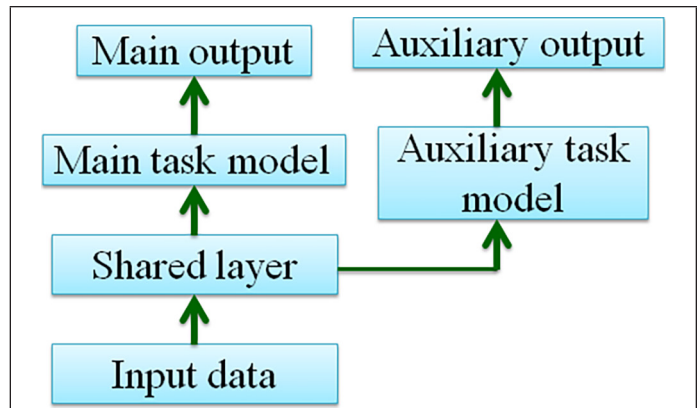


Figure 1. Typical structure of multi-task learning framework.

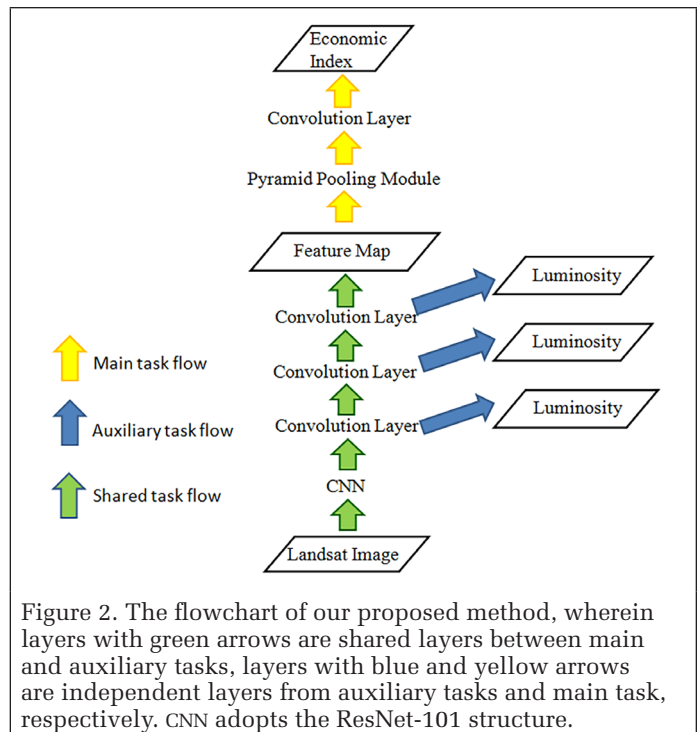


Figure 2. The flowchart of our proposed method, wherein layers with green arrows are shared layers between main and auxiliary tasks, layers with blue and yellow arrows are independent layers from auxiliary tasks and main task, respectively. CNN adopts the ResNet-101 structure.

task. The layers labeled as blue and yellow are independent layers in training auxiliary tasks and main task, respectively. Since the Landsat image and luminosity image are both global products, the quantity of training data can be guaranteed. Moreover, from Figure 2 we can recognize that the proposed model mainly comprises two parts, the convolutional neural network (CNN) and the pyramid pooling module. The convolutional neural network in our model stems from the structure of ResNet-101 (Szegedy *et al.* 2017), and the pyramid pooling module is from the pyramid scene parsing network (PSPNET) (Zhao *et al.* 2017), which achieved first place in the ImageNet Scene Parsing Challenge 2016. ResNet is practical in training deep neural network by introducing residual learning to simplify the training of deeper network in the network building block (shown in Figure 3) and improve the performance by overcoming the phenomenon of accuracy saturation (Zhao *et al.* 2017). The activation function adopts Rectified Linear Unit (ReLU) function (Nair and Hinton 2010), which is recognized as biologically plausible in object detection applications. Moreover, the  $1 \times 1$  kernel is used to reduce and recover the number of feature map channels and the  $3 \times 3$  kernel is used to do convolution operation to learn features. The detailed

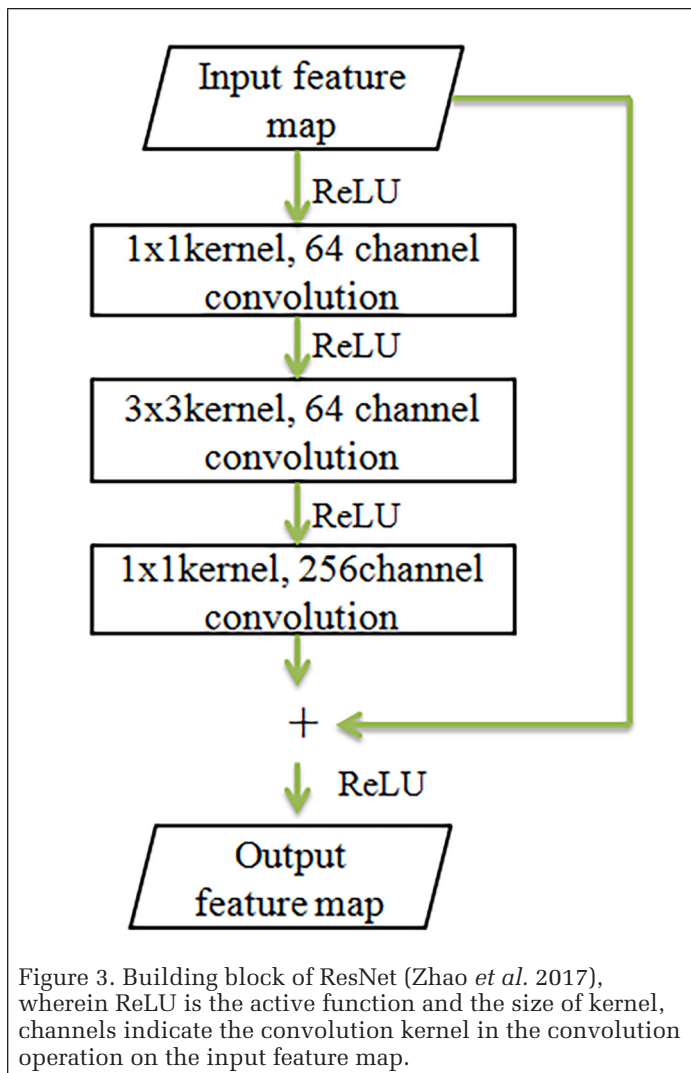


Figure 3. Building block of ResNet (Zhao *et al.* 2017), wherein ReLU is the active function and the size of kernel, channels indicate the convolution kernel in the convolution operation on the input feature map.

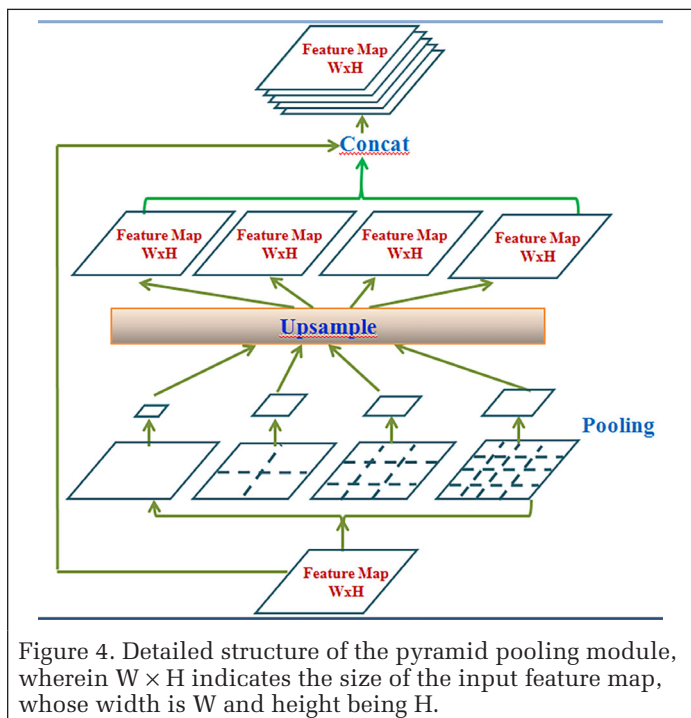


Figure 4. Detailed structure of the pyramid pooling module, wherein  $W \times H$  indicates the size of the input feature map, whose width is  $W$  and height being  $H$ .

network structure of the pyramid pooling module in PSPNET is shown in Figure 4. It consists of a pooling operation to extract the subinformation of the input feature map and upsample the pooled feature maps using bilinear operation to be the same size as that of the input feature maps, whose width is  $W$  and height is  $H$  in Figure 4. Such operations can be used to capture multi-scale local features in segmentation. That can be applied to delve into Landsat images for detailed ground object features. From Figure 2, we can recognize that the auxiliary tasks are located in shallower layers. That aims to regulate the main task model to converge continuously.

The pipeline of training our multi-task deep learning model mainly includes three steps. Firstly, the proposed model is partially initialized by the pretrained model ResNet-101 (Szegedy *et al.* 2017) on ImageNet data set (Russakovsky *et al.* 2015). The pretrained model has a strong capability to classify 1000 objects, which can enhance the discriminative ability of various ground objects of our model. Secondly, the initialized auxiliary task branch is fine-tuned by training the network to estimate luminosity of each pixel based on Landsat image. Such strategy is widely used, because it will be easier for the whole network to converge when part of the network has been trained in other relative tasks. On top of the fine-tuned auxiliary task model, we finally train the main task model to estimate economic index through pixel-level semantic segmentation strategy, calculating economic index for each pixel of the input image.

## Results and Discussion

To evaluate the multi-task model in estimating the economic statistics calculated by our proposed model in comprehensive economy and education, considering local comprehensive economy for Chinese counties, we conducted a 10-fold cross-validation covering national China for the two statistics separately. In terms of each validation, we calculated estimation accuracy and compared the results with the accuracy of the economic statistics calculated by the luminosity product only. Luminosity product is used as a control group, because it has been widely used in many economical evaluations (Chen and Nordhaus 2011; Jean *et al.* 2016). The statistics are calculated by the luminosity product according to our proposed model structure but without auxiliary tasks. The single-task model takes the luminosity product as an input image and the corresponding economic indices are the output. The comparisons of accuracies between both models are demonstrated in Figure 5. Clearly, we can recognize that Landsat images are far better in estimating economic statistics by providing more detailed and specific ground object information with six spectral bands especially. The accuracy achieved by semantic segmentation using luminosity product reaches only about 7.3%, while Landsat images are able to improve the estimation accuracy up to 85% and 86.5% in CEI and WCEI, respectively. Such improvement is dramatic and turns the proposed model into practically applicable with a reliable accuracy. The statistical significance is further calculated by t-test and the economic statistics in a comprehensive economy and education calculated by Landsat are significantly better than luminosity ( $p < 0.0001$ ).

Based on our trained framework, we have applied the model to fill up the void economic statistics in the Chinese county statistical yearbook using daytime Landsat images. Therefore, we have economic indices and composite sustainable economic indices considering welfare indicators including education, medical treatment, and old-age service covering counties in mainland China, as demonstrated in Figure 6. In accordance with the principle of statistical caliber with a Chinese county, the prefecture-level cities are left void. From Plate 6a we can see the county economy of mainland China in CEI shows a relatively higher level in the eastern coastal area, and a gradual step-down trend to the middle, western,

and northeastern areas. In addition, there is wide discrepancy among different provinces. In terms of social welfare considered in WCEI in Plate 6b, the overall economy level has been highly improved compared with CEI in Plate 6a apart from the counties around Chinese population line. That means that most counties in mainland China have a better level of social welfare economy, while the welfare situation for the transitional zone of population distribution is relatively poor. Moreover, the standard deviation of CEI and WCEI in each province also shares the same trend with the mean value discussed above, and the discrepancy among different provinces is reduced after considering social welfare indicators as well.

Apart from that, we also validate the reliability of the statistics of the six provinces in Central China, whose statistics are likely to be inconsistent due to the inconsistency in statistical caliber in the wave of urbanization.<sup>4</sup> We calculated the estimation accuracy and standard deviation of the six provinces in Central China to evaluate the reliability of the statistics collected and achieved an accuracy of 20.6% in CEI and 14.4% in WCEI economy indices. The accuracies are much lower than that of the other region of mainland China in Figure 5. The corresponding standard deviations are 2.08

4. The six provinces are: Jiangxi, Hunan, Hubei, Anhui, Shanxi, and Henan.

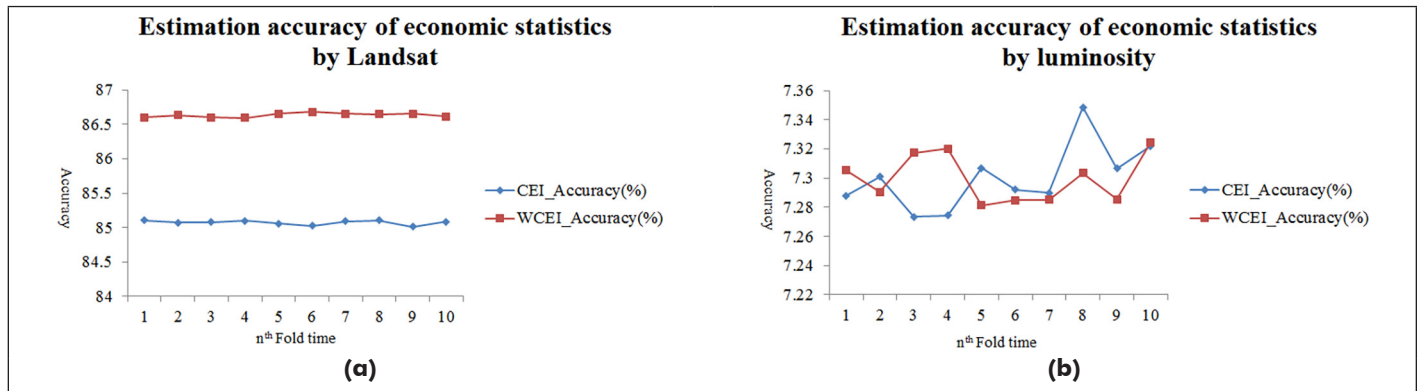


Figure 5. Comparisons of the estimated economic indices calculated using Landsat images and luminosity products in the 10-fold cross-validation.

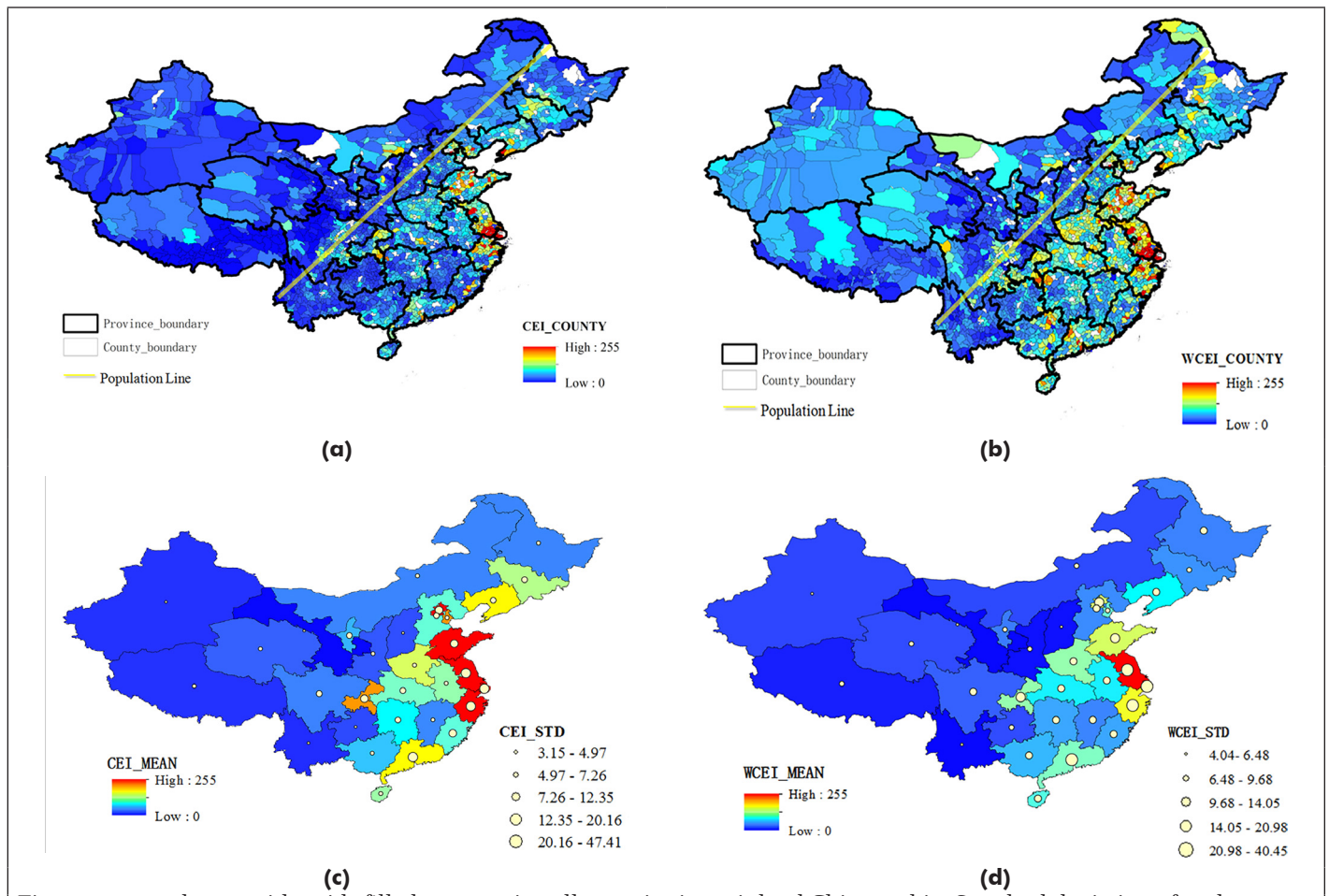


Figure 6. CEI and WCEI with voids filled up covering all counties in mainland China and its Standard deviation of each province, wherein (a) and (b) indicate the county economy status of mainland China in CEI and WCEI, respectively, (c) and (d) represent the standard deviation and mean values in each county in mainland china in CEI and WCEI, respectively.

and 3.13, respectively. Such phenomenon is consistent with the situation of “semiurbanization” happening in counties of Central China. In the wave of urbanization, the administrative boundaries of counties are not quite stable according to the project of “transforming county into urban district”. Therefore, the collections of economic statistics according to the boundaries are not quite stable as expected. Moreover, such collection will not only lead to a significantly underestimated urbanization rate, but also influence the evaluation accuracy of economy level (Chen and Nordhaus 2011; Jean *et al.* 2016).

The proposed method indicates that the daytime midresolution remote sensed images can be practically applied to estimate economic statistics for all the counties across national China. Apart from high spatial resolution images (Jean *et al.* 2016), the ground objects in midresolution daytime images with multiple spectral bands are enough to discriminate economic status among different counties as well. Our model gets a reliable estimation accuracy of 85% at pixel-level, which can be used to demonstrate the economic status in more details and straightforward. It does not need preprocessing, such as statistical clustering or model after model training, such as the training regression model after segmentation model as done in Jean *et al.* (2016). With little prior hypothesis and background knowledge, our model can get more objective economic estimations. Moreover, since daytime midresolution remote sensed images can indicate the economic prosperity with more details at a county level, it can be used as a reasonable instrumental variable to express the economic circumstance. In addition, we found that “semiurbanization” phenomenon highly influences the accuracy of the statistics in counties of Central China where we applied our model to estimate the CEI and WCEI indices. That mostly owes to the reason of the modification of statistical caliber in the wave of urbanization. In other words, our proposed model can be further used to modify the inconsistent statistics during the social and economic development period.

## Conclusions

Our multi-task deep learning framework provides a promising strategy in calculating economic statistics to make up for the missing data in traditional statistics collection. Through synthesizing the learned features from daytime Landsat images in the main task and the features from nighttime luminosity product in the auxiliary task, the constructed model can perform reliably in estimating socioeconomic statistics by handling overall information happening on the ground. Moreover, the pyramid pooling module in the model structure extracts multi-scale ground features, so that the economic features from ground objects can be represented robustly and propagated to the final layers. Therefore, it can achieve an accuracy of higher than 85% with a stable performance. Apart from that, the whole model structure does not need preprocessing, such as clustering or multiple model training, and the data used for training are employed from globally publicly available remote sensed images. The end-to-end deep neural network not only provides an efficient and practical method to economic researchers but also convenient for the official governments to evaluate the authenticity and validity of the statistics collected from the local government. However, there is also limit for the proposed model, that other socioeconomic relevant data, such as rainfall, distance to rivers, and landscape pattern, can be adopted to build a more comprehensive model to improve the estimation accuracy at county level. Our proposed model provides a potential strategy to replace traditional time and money consuming statistics collection in the future.

## Acknowledgments

This work was supported by the National Key R&D Program of China (Grant No.2017YFE0100800), the National Natural Science Foundation of China (41871345), and the International Partnership Program of the Chinese Academy of Sciences (Grant No. 131211KYSB20170046).

## References

- Baxter, J. 2000. A model of inductive bias learning. *Journal of Artificial Intelligence Research (JAIR)* 12 (3):149–198.
- Blumenstock, J., G. Cadamuro and R. On. 2015. Predicting poverty and wealth from mobile phone metadata. *Science* 350 (6264):1073–1076.
- Caruana, R. 1998. Multitask learning. In *Learning to Learn*, 95–133. Springer.
- Chen, X. and W. D. Nordhaus. 2011. Using luminosity data as a proxy for economic statistics. *Proceedings of the National Academy of Sciences* 108 (21):8589–8594.
- Cheng, X., L. Chen, R. Sun and P. Kong. 2018. Land use changes and socio-economic development strongly deteriorate river ecosystem health in one of the largest basins in China. *Science of the Total Environment* 616:376–385.
- Csaplovics, E. 2003. Multi-task remote sensing supporting the development of environmental policies for National Park regions in the Central European Space. Pages 4573–4575 in *Proceedings of the Geoscience and Remote Sensing Symposium (IGARSS'03)*.
- Deng, L., G. Hinton and B. Kingsbury. 2013. New types of deep neural network learning for speech recognition and related applications: An overview. Pages 8599–8603 in *Proceedings of the Acoustics, Speech and Signal Processing (ICASSP)*.
- Dong, H., S. Duan, L. Bogg, Y. Wu, H. You, J. Chen, X. Ye, K. Seccombe and H. Yu. 2016. The impact of expanded health system reform on governmental contributions and individual copayments in the new Chinese rural cooperative medical system. *The International Journal of Health Planning and Management* 31 (1):36–48.
- Friedmann, J. 2005. *China's Urban Transition*. University of Minnesota Press.
- Girshick, R. 2015. Fast R-CNN. *arXiv preprint arXiv:1504.08083*.
- He, K., X. Zhang, S. Ren and J. Sun. 2016. Deep residual learning for image recognition. Pages 770–778 in *Proceedings of the IEEE Conference on Computer Vision and Pattern Recognition*.
- Ieag, U. 2014. *A World that Counts—Mobilising the Data Revolution for Sustainable Development*. Report prepared for the U.N. Secretary General by the Independent Expert Advisory Group on a Data Revolution for Sustainable Development.
- Jean, N., M. Burke, M. Xie, W. M. Davis, D. B. Lobell and S. Ermon. 2016. Combining satellite imagery and machine learning to predict poverty. *Science* 353 (6301):790–794.
- LeCun, Y., Y. Bengio and G. Hinton. 2015. Deep learning. *Nature* 521 (7553):436.
- Li, H. and K. K.-S. James. 2015. Fiscal incentives and policy choices of local governments: Evidence from China. *Journal of Development Economics* 116:89–104.
- Li, X., D. Zhang, Z. Liu, Z. Li, C. Du and C. Dong. 2015. Materials science: Share corrosion data. *Nature News* 527 (7579):441.
- Litjens, G., T. Kooi, B. E. Bejnordi, A. A. A. Setio, F. Ciampi, M. Ghafoorian, J. A. van der Laak, B. van Ginneken and C.I. Sánchez. 2017. A survey on deep learning in medical image analysis. *Medical Image Analysis* 42:60–88.
- Liu, J., J. Li, W. Li and J. Wu. 2016. Rethinking big data: A review on the data quality and usage issues. *ISPRS Journal of Photogrammetry and Remote Sensing* 115:134–142.
- Lo, A. Y. 2016. Challenges to the development of carbon markets in China. *Climate Policy* 16 (1):109–124.
- Mackenbach, J. P. 2012. The persistence of health inequalities in modern welfare states: The explanation of a paradox. *Social Science & Medicine* 75 (4):761–769.

- Nair, V. and G. E. Hinton. 2010. Rectified linear units improve restricted Boltzmann machines. In *Proceedings of the 27th International Conference on Machine Learning*, held in Haifa, Israel.
- NOAA. 2013. Version 4 DMSP-OLS nighttime lights time series. *National Oceanic and Atmospheric Administration-National Geophysical Data Center*.
- Pan, X., X. Wei and Y. Wang. 2015. Explorations on optimizing the statistical caliber of urbanization rate in counties in Central China: The perspective of semi-urbanization. *Planning Studies* 39 (11):48–54.
- Puzo, Q., L. Mehlum and P. Qin. 2018. Socio-economic status and risk for suicide by immigration background in Norway: A register-based national study. *Journal of Psychiatric Research* 100:99–106.
- Ramsundar, B., S. Kearnes, P. Riley, D. Webster, D. Konerding and V. Pande. 2015. Massively multitask networks for drug discovery. *arXiv preprint arXiv:1502.02072*.
- Rindermann, H. 2008. Relevance of education and intelligence at the national level for the economic welfare of people. *Intelligence* 36 (2):127–142.
- Russakovsky, O., J. Deng, H. Su, J. Krause, S. Satheesh, S. Ma, Z. Huang, A. Karpathy, A. Khosla and M. Bernstein. 2015. ImageNet large scale visual recognition challenge. *International Journal of Computer Vision* 115 (3):211–252.
- Short, N. 1982. The Landsat tutorial workbook—Basics of satellite remote sensing. *NASA*.
- Szegedy, C., S. Ioffe, V. Vanhoucke and A. A. Alemi. 2017. Inception-v4, inception-resnet and the impact of residual connections on learning. Page 12 in the *Proceedings of the AAAI Conference*.
- Tao, F., S. Zhang, Z. Zhang and R. P. Rötter. 2015. Temporal and spatial changes of maize yield potentials and yield gaps in the past three decades in China. *Agriculture, Ecosystems & Environment* 208:12–20.
- Teng, T.-W., S.-L. Hu and L.-Y. Hou. 2016. The industrial transfer trend and spatial pattern of undertaking industry in the Yangtze River economic belt. *Economic Geography*.
- Wang, C. 2006. A study of floating rural people's "semi-urbanization". *Sociological Studies*.
- Wang, F. 2015. Impact of urban designation criteria and criteria for statistically defining urban population on urbanization development in China. *Population & Development* 17 (2):82–87.
- Wei, Y. and L. Zhang. 2013. "Statistical chaos" or "divisional administration" : An understanding of multiple definitions of China's floating population. *Population Research* 37 (4):56–65.
- Wong, L. 2008. The third sector and residential care for the elderly in China's transitional welfare economy. *Australian Journal of Public Administration* 67 (1):89–96.
- Yu, B. and I. Lane. 2014. Multi-task deep learning for image understanding. In *Proceedings of the 2014 6th International Conference of Soft Computing and Pattern Recognition (SoCPaR)*.
- Yu, L. and Y. Jin. 2016. Parameter estimation methods dealing with nonignorable missing data in panel data. *Statistical Research* 33 (1):95–102.
- Zhang, L. 2011. A discussion on the definition of urban/rural population in the Chinese urbanization process. *Urban Planning Forum* (2):77–85.
- Zhang, L., L. Zhang and B. Du. 2016. Deep learning for remote sensing data: A technical tutorial on the state of the art. *IEEE Geoscience and Remote Sensing Magazine* 4 (2):22–40.
- Zhao, H., J. Shi, X. Qi, X. Wang and J. Jia. 2017. Pyramid scene parsing network. Pages 6230–6239 in the *Proceedings of the IEEE Conference on Computer Vision and Pattern Recognition (CVPR)*.

# WHO'S WHO IN ASPRS

## BOARD OF DIRECTORS

### BOARD OFFICERS

#### President

Thomas Jordan, Ph.D.  
*University of Georgia*

#### President-Elect

Jeff Lovin  
*Woolpert*

#### Vice President

Jason M. Stoker, Ph.D.  
*U.S. Geological Survey*

#### Past President

Anne Hillyer, CP  
*Bonneville Power Administration (USDOE)*

#### Treasurer

Stewart Walker, Ph.D.

#### Secretary

Roberta E. Lenczowski

### BOARD MEMBERS

#### Sustaining Members Council – 2019

Chair: Joe Cantz

Vice Chair: TBA

[www.asprs.org/About-Us/Sustaining-Members-Council.html](http://www.asprs.org/About-Us/Sustaining-Members-Council.html)

#### Early-Career Professionals Council – 2020

Chair: Peng Fu

Vice Chair: TBA

#### Region Officers Council – 2021

Chair: Lorraine B. Amenda, PLS, CP

Vice Chair: Demetrio Zourarakas

#### Student Advisory Council – 2020

Chair: Victoria Scholl

Vice Chair: TBA

<http://www.asprs.org/Students/Student-Advisory-Council.html>

#### Technical Division Directors Council – 2020

Chair: John McCombs

Vice Chair: Bandana Kar, Ph.D.

### TECHNICAL DIVISION OFFICERS

#### Geographic Information Systems Division – 2021

Director: Xan Fredericks

Assistant Director: Denise G. Theunissen  
[www.asprs.org/Divisions/GIS-Division.html](http://www.asprs.org/Divisions/GIS-Division.html)

#### Lidar Division – 2020

Director: Amar K. Nayegandhi, CP, CMS

Assistant Director: Joshua Nimetz, CMS  
[www.asprs.org/Divisions/Lidar-Division.html](http://www.asprs.org/Divisions/Lidar-Division.html)

#### Photogrammetric Applications Division – 2020

Director: Paul C. Bresnahan

Assistant Director: Kurt Rogers  
[www.asprs.org/Divisions/Photogrammetric-Applications-Division.html](http://www.asprs.org/Divisions/Photogrammetric-Applications-Division.html)

#### Primary Data Acquisition Division – 2021

Director: Jon Christopherson

Assistant Director: J. Chris Ogier  
[www.asprs.org/Divisions/Primary-Data-Aquisition-Division.html](http://www.asprs.org/Divisions/Primary-Data-Aquisition-Division.html)

#### Professional Practice Division – 2022

Director: Harold W. Rempel, III, CP

Assistant Director: TBA  
[www.asprs.org/Divisions/Professional-Practice-Division.html](http://www.asprs.org/Divisions/Professional-Practice-Division.html)

#### Remote Sensing Applications Division – 2020

Director: David W. Kreighbaum

Assistant Director: Raechel A. White, Ph.D.  
[www.asprs.org/Divisions/Remote-Sensing-Applications-Division.html](http://www.asprs.org/Divisions/Remote-Sensing-Applications-Division.html)

#### Unmanned Autonomous Systems (UAS) – 2020

Director: Benjamin Vander Jagt, Ph.D.

Assistant Director: Megan Miller, Ph.D.

### REGION PRESIDENTS

#### Alaska Region

David Parret

<http://www.asprsalaska.org/>

#### Cascadia Region

TBA

<http://columbia.asprs.org/CRR/>

#### Central New York Region

John Boland, C.P.

<http://www.esf.edu/asprs/>

#### Eastern Great Lakes Region

Edward Kunz, GISP

<http://egl.asprs.org/>

#### Florida Region

Erin McCormick

<http://florida.asprs.org/>

#### Heartland Region

Paul Manley

<http://heartland.asprs.org/>

#### Intermountain Region

TBA

<http://asprsimountain.weebly.com/>

#### Mid-South Region

Dr. David Hughes

<https://www.asprs.org/all-regions/mid-south.html>

#### New England Region

TBA

<http://neweng.asprs.org/>

#### North Atlantic Region

Richard W. Carlson, Jr., P.L.S., C.P.

<http://natlantic.asprs.org/>

#### Pacific Southwest Region

Riadh Munjy, Ph.D.

<https://pswasprs.org/>

#### Potomac Region

Jackie Carr

<http://www.asprspotomac.org/>

#### Rocky Mountain Region

Jeffrey M. Young

<http://www.asprs-rmr.org/>

#### Western Great Lakes Region

Kirk Contrucci, CP

<http://wgl.asprs.org/>

# Multi-Spatial Resolution Satellite and sUAS Imagery for Precision Agriculture on Smallholder Farms in Malawi

Brad G. Peter, Joseph P. Messina, Jon W. Carroll, Junjun Zhi, Vimbayi Chimonyo, Shengpan Lin, and Sieglinde S. Snapp

## Abstract

*A collection of spectral indices, derived from a range of remote sensing imagery spatial resolutions, are compared to on-farm measurements of maize chlorophyll content and yield at two trial farms in central Malawi to evaluate what spatial resolutions are most effective for relating multispectral images with crop status. Single and multiple linear regressions were tested for spatial resolutions ranging from 7 cm to 20 m using a small unmanned aerial system (sUAS) and satellite imagery from Planet, SPOT 6, Pléiades, and Sentinel-2. Results suggest that imagery with spatial resolutions nearer the maize plant scale (i.e., 14–27 cm) are most effective for relating spectral signals with crop health on smallholder farms in Malawi. Consistent with other studies, green-band indices were more strongly correlated with maize chlorophyll content and yield than conventional red-band indices, and multivariable models often outperformed single variable models.*

## Introduction

### Precision Agriculture and sUAS

Precision agriculture has become a prominent subject of research for remote sensing of cropping systems since the advent of individual-use small unmanned aircraft systems (sUAS) (Zhang and Kovacs 2012). While national governments have been monitoring agricultural production via satellite since the 1970s (Macdonald 1984), coarse spatial resolutions, cloud cover, and infrequent collection has rendered much of these image data unfit for the needs of smallholder farmers (Mulla 2013). Now, the use of quadcopters and fixed-wing drones for precision farming continues to grow as sUAS technologies become increasingly cost effective and programmatic operations are developed that streamline the process of collecting

Brad G. Peter is with The University of Alabama, Department of Geography, Farrah Hall, Tuscaloosa, AL 35405 (bpeter@ua.edu).

Joseph P. Messina is with The University of Alabama, College of Arts & Sciences, Clark Hall, Tuscaloosa, AL 35487.

Jon W. Carroll is with Oakland University, Department of Sociology, Anthropology, Social Work, and Criminal Justice, Varner Hall, Rochester, MI 48309.

Junjun Zhi is with the Anhui Normal University, School of Geography and Tourism, Wuhu, 241002, China.

Vimbayi Chimonyo is with the University of KwaZulu-Natal, School of Agricultural, Earth, and Environmental Sciences, Scottsville 3290, Pietermaritzburg, South Africa.

Shengpan Lin (deceased) was with Michigan State University, Social Science Data Analytics Initiative, East Lansing, MI 48824 at the time of research.

Sieglinde S. Snapp is with Michigan State University, Department of Plant, Soil, and Microbial Sciences, Plant and Soil Sciences, Michigan State University, East Lansing, MI 48824.

imagery and generating map outputs (Floreano and Wood 2015). Many sUAS, such as the senseFly eBee fixed-wing aircraft with eMotion software, no longer require manual piloting and can be launched with preprogrammed flight plans. Moreover, associated software such as Pix4D photogrammetric software (Pix4D SA 2017) can handle many of the previously arduous image preprocessing tasks, such as image mosaicking, georeferencing, orthorectification, and radiometric calibration.

The autonomous acquisition and processing of remote sensing data via sUAS, coupled with attainable fine spatial resolutions, are rapidly transforming the landscape of remote sensing science. Lippitt and Zhang (2018) offer a conceptual perspective on the historical and future use of sUAS in the field of remote sensing, as well as the technological and theoretical challenges faced; similarly, Pajares (2015) offers an exhaustive synopsis of technologies, applications, sensors, and methods in sUAS-based remote sensing. Automation advancements in sUAS have made precision agriculture accessible to users with minimal to no experience with aerial vehicle piloting and remote sensing-based crop analytics. While the abundance and affordability of sUAS may be a net positive for monitoring agriculture, the emergent limitations, challenges, and potential misuse are not completely understood, and given the continually changing nature of sUAS, optimal operational frameworks are not always present or relevant (Mesas-Carrascosa *et al.* 2015).

### Multispectral Imaging Capabilities of sUAS

The standard agricultural-use sUAS multispectral camera, such as the Parrot Sequoia used here, can acquire images across five spectral wavelengths; onboard sensors include red, green, red edge, near-infrared (NIR), and red, green, and blue (RGB) (Parrot Drones SA 2017). More sophisticated cameras with a broader range of spectral bands can record shortwave infrared (SWIR) and thermal infrared (TIR) (Saari *et al.* 2017; Stark, McGee, and Chen 2015), which are critical for monitoring crop water and heat stress (Ceccato *et al.* 2001). With the visible spectrum (RGB) and NIR, a broad range of crop status indices can be calculated. Most notable is the normalized difference vegetation index (NDVI) (Tucker 1979). This metric is widely used as a measure of crop health—a healthy plant will absorb visible light (especially blue and red), while the fortified leaf structure will reflect a high amount of NIR. NDVI calculation is simply  $(\text{NIR} - \text{red}) / (\text{NIR} + \text{red})$ , returning values between  $-1$  and  $1$ , ranging from nonvegetated (water or barren) to healthy crops and plants with a high leaf area index (LAI) (Jiang *et al.* 2006). Beyond being a metric for crop health, NDVI is frequently correlated with crop production and yield, thus many farmers find value in mapping NDVI across their fields (Wall, Larocque, and Léger 2008).

Photogrammetric Engineering & Remote Sensing  
Vol. 86, No. 2, February 2020, pp. 107–119.  
0099-1112/20/107–119

© 2020 American Society for Photogrammetry  
and Remote Sensing  
doi: 10.14358/PERS.86.2.107

Although NDVI is an extensively used vegetation index, it is well known that it does not always emerge as having the strongest correlation with on-farm yields or leaf chlorophyll content and is often outperformed by other remote sensing indicators (Hatfield and Prueger 2010). Indices that are regularly used to correlate spectral signals with crop status include green normalized difference vegetation index (GNDVI), soil adjusted vegetation index (SAVI), green soil adjusted vegetation index (GSAVI), green chlorophyll index (GCI), ratio vegetation index (RVI), chlorophyll vegetation index (CVI), and modified chlorophyll absorption ratio index 1 (MCARI1). Zhu, Wang, and Yao (2012), for example, found that SAVI was effective for estimating leaf nitrogen content of wheat. Shanahan *et al.* (2001) found GNDVI to be highly correlated with corn grain yields, particularly during midgrain filling. Panda, Ames, and Panigrahi (2010) found the red- and NIR-based perpendicular vegetation index (PVI) reliable for predicting corn yields. Mulla (2013) supplies a comprehensive list of remote sensing-based indices used in precision agriculture contexts.

### What Spatial Resolutions and Spectral Indices Are Needed?

Fine spatial resolution sUAS offer unprecedented levels of geospatial analytics at the farm scale; however, while the use of sUAS for precision agriculture is growing, the potential benefits have not yet been sufficiently exploited in smallholder systems in southern Africa (Dlodlo and Kalezhi 2015). At submeter spatial resolutions, intrafarm variability can be measured and intrafarm recommendations made; however, the linear correlation between remote sensing-based indices and *in situ* crop measurements will vary depending on the crop evaluated, crop growth stage, planting density, index selected, spatial resolution of the imagery, and interference of clouds, shadows, or soil (Hatfield and Prueger 2010).

Over the last several decades, much of remote sensing science has utilized satellite data with static spatial resolutions (e.g., Landsat and Moderate Resolution Imaging Spectroradiometer (MODIS)). Sensors onboard aircrafts offered some level of control in terms of spatial resolutions achieved, but remote sensing-based analyses that commission aircraft missions are comparatively rare. In the modern era, sUAS devices have opened a broad range of spatial resolutions attainable at the submeter scale. In contrast to satellite systems, sUAS can provide intrafarm measurements for individual plants down to the leaf scale. Since sUAS have become available for individual researchers, satellite-based remote sensing scientists migrating to sUAS technologies now bear the onus of selecting appropriate spatial resolutions (Hengl 2006).

Finer spatial resolution data are commonly regarded as superior; however, the most effective spatial resolutions for specific applications is currently under researched, and it may often be the case that the finest spatial resolution is not the optimal choice. One study conducted by Mesas-Carrascosa *et al.* (2015) explored optimal flight parameters for spectral discrimination of bare soil, crops, and weeds. At all flight heights (60, 80, and 100 m; spatial resolutions of 3 cm, 4 cm, and 5 cm, respectively), spectral discrimination of bare soil and vegetation showed satisfactory results, suggesting that flying higher (coarser spatial resolution) might be an acceptable tradeoff to capture a larger extent (Mesas-Carrascosa *et al.* 2015).

Of particular interest in this study is the utility of various sUAS-based spectral signatures and the appropriate spatial resolutions for the scales of analysis in smallholder agriculture contexts.

Two questions of interest regarding sUAS spatial resolutions and spectral measurements are addressed: (1) What spatial resolutions (ranging from national government and commercial satellites to sUAS) are effective for conducting precision agriculture at the smallholder farm scale in Malawi? (2) What spectral indices are effective for informing variable-rate technologies on smallholder farms? This study evaluates a comprehensive range of satellite and sUAS spatial resolutions

and spectral indices (given the availability of data at the time of analysis) to determine effective spatial resolutions for precision agriculture in the smallholder farming context.

### National Government and Commercial Satellites

While sUAS are an increasingly viable option for industrial farms and many small-scale operations, there is still a considerable financial and infrastructural barrier to entry in many remote areas (Dlodlo and Kalezhi 2015; Zhang and Kovacs 2012). As such, national government and commercial satellites play an integral role in scaling agricultural technologies and improving crop production worldwide. MODIS (250 m), Landsat (30 m), and Sentinel-2 (20 m) are national government satellites that offer global coverage at regular temporal intervals. Governmental and commercial satellites that collect quasi-global imagery with finer spatial resolution can be commissioned for specific missions. Notably, SPOT 6 (6 m), Planet (3 m), Pléiades (2 m), and WorldView-2 (1.8 m) satellites offer regional, interfarm, and intrafarm multispectral imagery to measure crop status, although none at the individual maize plant scale with multispectral bands (Planet Team 2017; Airbus Defence and Space 2012a; Airbus Defence and Space 2012b; DigitalGlobe 2009). Although MODIS, Landsat, and Sentinel-2 images are free to the public, finer spatial resolution images require purchase. A cost per spatial resolution curve of multispectral imagery from the Apollo Mapping repository (Apollo Mapping 2018) is plotted for comparison in Figure 1.

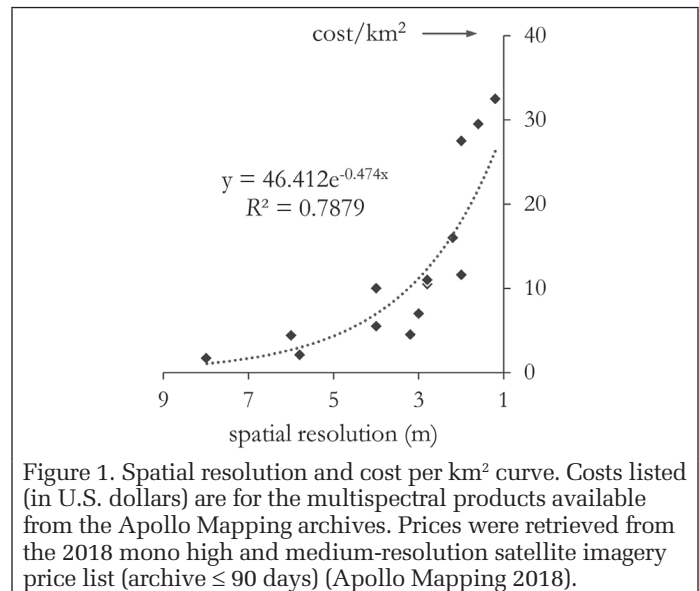


Figure 1. Spatial resolution and cost per km<sup>2</sup> curve. Costs listed (in U.S. dollars) are for the multispectral products available from the Apollo Mapping archives. Prices were retrieved from the 2018 mono high and medium-resolution satellite imagery price list (archive ≤ 90 days) (Apollo Mapping 2018).

### Variable-Rate Technology and Spectral Signatures of a Farm

Perhaps the most common use of sUAS imagery on-farm is the application of variable-rate technology (VRT). VRT is the term coined to describe farm productivity improvement applications that are informed by spatiotemporal measurements of crop performance (Sawyer 1994). In the case of NDVI being used as an indicator of crop productivity, fertilizer may be applied proportionately across a field (or within plots) depending on the spatial organization of measured crop status. VRT combined with crop modeling predictions is another way in which sUAS imagery is being used to improve farm production (Basso *et al.* 2001). Considering nitrogen use efficiency at various stages of crop growth, fertilizer applied to a plant of moderate to high health can have a greater return on investment than fertilizer applied to an unhealthy plant (Cassman, Dobermann, and Walters 2002). Further continuing the precision autonomous farming trends, large-scale agribusinesses have begun to leverage global positioning system (GPS)-enabled

systems to guide fertilizer and water application relative to spatial need as measured via sUAS (Eaton *et al.* 2008).

In other VRT applications, the normalized difference water index (NDWI), a ratio of the SWIR and NIR bands (Gao 1996) or a ratio of the green and NIR bands (McFeeters 1996), can inform how water supply is managed across a field (e.g., directing water to areas where crops are experiencing water stress and/or restricting the amount delivered to areas at risk of waterlogging). Depending on the spatial resolution, an image interpreter may also be able to visually detect areas that are experiencing leaf damage from pests or disease and identify invasive plants and weeds between row crops (Hunt and Daughtry 2017; Peña *et al.* 2013). Furthermore, elevation point clouds derived from sUAS imagery can be used to model hydrology, identify sloping terrain prone to erosion, and illuminate areas susceptible to pooling (Beene, Zhang, and Paulus 2019; Pineux *et al.* 2017), which can be managed by manipulating the field structure or by integrating crops with substantial root biomass (Gyssels and Poesen 2003).

### Smallholder Farms in Sub-Saharan Africa

Smallholder agriculture, also referred to as subsistence or small-scale farming, is the predominant form of crop cultivation in southern Africa (Franke, van den Brand, and Giller 2014). Regional differences in scale of production and agro-ecological constraints exist among the smallholder farming population (Williams *et al.* 2018); however, smallholder farmers are typically characterized as rural producers with land holdings ranging between 0.5 and 5 hectares (ha) (Ngcoya and Kumarakulasingam 2017). Smallholder agricultural production systems often exhibit mixed cropping, variable management practices, and may have “fuzzy” field boundaries (Jain *et al.* 2017; Jayne *et al.* 2016). Problematically, Matese *et al.* (2015) found that satellite-based land characterizations failed to adequately represent intrafield variability (vineyards in this case), particularly in heterogeneous systems.

Smallholder farmers often face considerable challenges associated with limited natural resources, under-resourced extension services, lack of infrastructure, unpredictable markets, and access to climate and terrain information needed to make informed management decisions (Giller *et al.* 2006; Lowder, Skoet, and Raney 2016; Williams *et al.* 2018). According to the National Statistical Office of Malawi (NSO 2012) Integrated Household Survey 3 (IHS3), approximately 85% of Malawian households engage in agricultural activities; of the rural population, 94% engage in agricultural activities. With recurring food shortages countrywide (Babu and Sanyal 2018), it is critical to increase smallholder farm production to

improve the overall national food security status. Given these challenges, there is apparent need to generate more geospatial climate and crop productivity data at fine spatial scales that can address the heterogeneity across the smallholder agriculture landscape in Malawi to improve precision agriculture, food security, and farm resilience.

## Methods and Data

### Remote Sensing Product and Workflow Overview

The objective of this study was to test for linear relationships between *in situ* farm measurements (crop chlorophyll content and yield) and spectral indices of crop status across multiple spatial resolutions. Spatial resolutions included in this analysis are 7 cm, 14 cm, and 27 cm (sUAS), 2 m (Pléiades), 3 m (Planet), 6 m (SPOT 6), and 20 m (Sentinel-2); spatial resolutions of 30 m (Landsat 8), 250 m (MODIS), 500 m (Visible Infrared Imaging Radiometer Suite ([VIIRS])), and 5 km (Advanced Very-High-Resolution Radiometer ([AVHRR])) are also included in this analysis, but only in time-series presentation to demonstrate timing issues (Table 1).

The workflow for this study (outlined in Figure 2) consisted of the following: (1) sUAS image collection and satellite image acquisition, (2) image mosaicking, georeferencing, radiometric calibration, and orthorectification, (3) index calculation (NDVI, GNDVI, SAVI, GSAVI, GCI, RVI, CVI, and MCARI1), (4) mean zonal statistic calculations by plot for each index, (5) single multiple linear regression (SLR) and multiple linear regression (MLR) permutations of all selected indices compared to crop chlorophyll content and crop yield, (6) regression model rankings using Akaike information criterion (AICc) (Akaike 1974), and (7) comparison of correlation results across all spatial resolutions under analysis. The performance of each spectral index in relation to on-farm crop measurements was also evaluated.

### Study Area and Plot Design

The study was conducted at two experimentation farms in the central region district of Machinga, in the villages of Ntubwi and Nyambi (Figure 3). Nyambi is characterized predominantly by clay loam soils (chromic luvisols and orthic ferralsols) and Ntubwi is characterized predominantly by sandy loam soils (ferric luvisols). The farms were separated into three columns (referred to herein as replicates), each containing nine unique fertilizer treatments (T) (Table 2). There are 27 total plots per farm, with six rows of monocrop maize in each plot; surrounding land cover was a complex mosaic of

Table 1. Summarization table of data used in this study.

Platform	Type	Spatial Resolution	Collection Date	Location
<sup>1</sup> senseFly eBee	sUAS	7 cm, 14 cm, and 27 cm	20 Feb. 2018 19 Feb. 2018	Nyambi Ntubwi
<sup>2</sup> Pléiades	Satellite	2 m	28 Jan. 2018	Nyambi
<sup>3</sup> Planet	Satellite	3 m	20 Feb. 2018 17 Feb. 2018	Ntubwi Nyambi
<sup>4</sup> SPOT 6	Satellite	6 m	25 Mar. 2018	Ntubwi
<sup>5</sup> Sentinel-2	Satellite	20 m	20 Feb. 2018 20 Feb. 2018	Ntubwi Nyambi

The following data products are used for time-series demonstration in Figure 4.

Sentinel-2	Satellite	20 m	2017/2018	Nyambi
Landsat 8	Satellite	30 m	2017/2018	Nyambi
MODIS	Satellite	250 m	2017/2018	Nyambi
VIIRS	Satellite	500 m	2017/2018	Nyambi
AVHRR	Satellite	~5 km	2017/2018	Nyambi

There are three modes of data presentation in this analysis: statistics, illustration, and time-series. Refer to Figure 4 for time-series illustration. Refer to Figure 8 and Plates 1, 2, and 3 for sample imagery. Refer to Table 5, Figure 12, and Figures 7 and 8 for statistical analyses. <sup>1</sup>Parrot Sequoia multispectral camera specifications: green 530–570 nm, red 640–680 nm, and NIR 770–810 nm. <sup>2</sup>Pléiades Level 1A top of atmosphere (TOA) reflectance; multispectral specifications: green 490–610 nm, red 600–720 nm, and NIR 750–950 nm. <sup>3</sup>PlanetScope Level 3B surface reflectance (SR); multispectral specifications: green 500–590 nm, red 590–670 nm, and NIR 780–860 nm. <sup>4</sup>SPOT 6 Level 1A TOA; multispectral specifications: green 530–590 nm, red 625–695 nm, and NIR 760–890 nm. <sup>5</sup>Sentinel-2 Level 1C TOA; multispectral specifications: green 560 nm, red 665 nm, and NIR 835 nm.

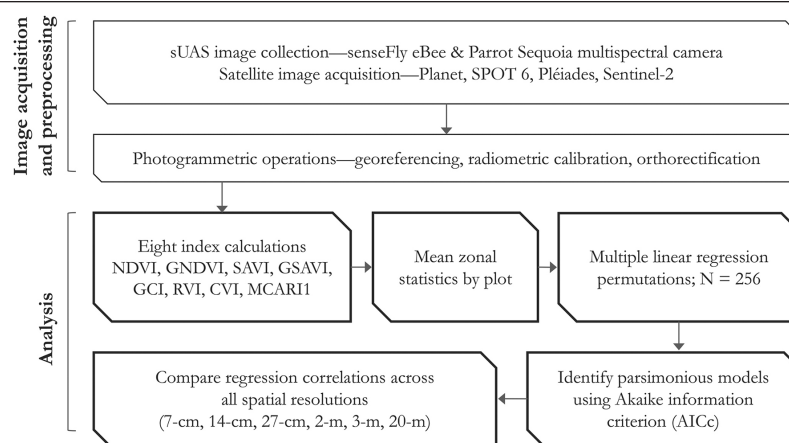


Figure 2. Heuristic: Multi-spatial resolution satellite and sUAS imagery for precision agriculture on smallholder farms in Malawi. Image acquisition and preprocessing is detailed in Figure 5.

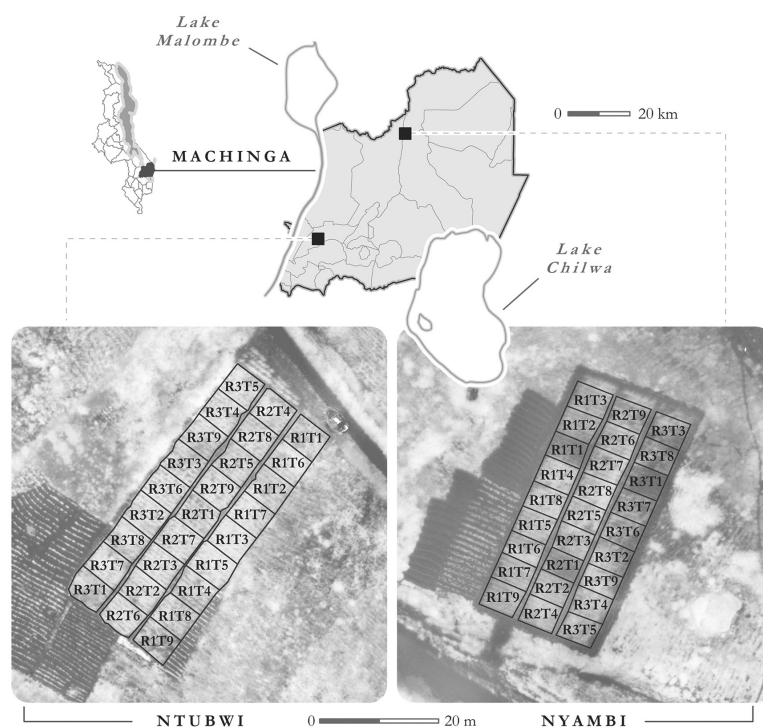


Figure 3. Study area map of the trial farms in Ntubwi and Nyambi, Malawi, with plots of differing management strategies labeled (refer to Table 4 for plot metrics).

Table 2. Nitrogenous fertilizer applications were split between a basal application at planting and a top-dress application during crop growth.

Treatment	Basal N:P	N Top-Dressing	Total N	Side Dress 1, 2, 3
1	0:21*	0	0	-, -, -
2	23:21	0	23	-, -, -
3	23:21	23	46	23, -, -
4	23:21	46	69	23, 23, -
5	23:21	69	92	23, 46, -
6	23:21	92	115	46, 46, -
7	23:21	115	138	46, 46, 23
8	23:21**	69	92	23, 46, -
9	23:21	var***	var	var, var, var

\*The control received 21 kg P ha<sup>-1</sup> in the form of single super phosphate. Treatments 2–9 received basal fertilizer in a compound of 23 kg N and 21 kg P ha<sup>-1</sup>. \*\*Treatment 8 was similar to treatment 5 but received micronutrient zinc in the form of zinc sulfate. \*\*\*Treatment 9 was designed to simulate the rate and timing of fertilizer application by farmers in the respective regions.

agriculture (e.g., groundnut, soybean, cassava, and finger millet), tree cover, shrubs, barren land, and housing structures. The Ntubwi farm is approximately 0.092 ha (918 m<sup>2</sup>) with an average plot size of 34.0 m<sup>2</sup> and the Nyambi farm is approximately 0.077 ha (769 m<sup>2</sup>) with an average plot size of 28.5 m<sup>2</sup>. These farms are under experimentation by a research group at Michigan State University in collaboration with Africa RISING and researchers at the Lilongwe University of Agriculture and Natural Resources (LUANAR) evaluating maize response to variable fertilizer treatments.

### Problems of Clouds and Satellite Revisit Rates

One substantial challenge associated with precision agriculture using remote sensing satellites is the abundance of clouds during the crop production season. This is particularly problematic in Malawi, where the unimodal rainy season introduces regular cloud cover. Advances in spatial and temporal resolution satellite imaging have made precision agriculture in remote areas increasingly feasible; however, persistent cloud cover and infrequent satellite image revisit rates pose a considerable hurdle (Mulla 2013) and may result in few clear images available for farm observation. In the peak of the Malawi growing season, this may mean that only a handful of commercial satellite images free of clouds will be available. In the case presented here, for two trial sites in the central region of Malawi (Ntubwi and Nyambi) during peak growing season (February/March), only one clear image was available from Pléiades and only one clear image was available from SPOT 6; no WorldView-2 imagery was satisfactory. Cloud-free Planet images were available for both sites in close temporal proximity to the sUAS flights (refer to Table 1).

The regular revisit rate of national government satellites (e.g., Sentinel-2) can largely overcome the temporal hurdle; however, the spatial resolution is insufficient for intrafarm precision agriculture in the Malawian smallholder context, where a 0.5 hectare farm may contain only nine complete Sentinel-2 20 m pixels. To demonstrate and visualize the cloud-cover problem, NDVI imagery was assembled for the Nyambi trial farm from five global monitoring satellites—AVHRR (Vermote *et al.* 2014), VIIRS (NASA LP DAAC 2015a), MODIS (NASA LP DAAC 2015b), Landsat 8 (USGS 2013), and Sentinel-2 (ESA 2015) (Figure 4). Each open circle on the time-series represents an image collection and/or image delivery. In the case of VIIRS and MODIS, composite images are delivered that “smooth” out the effects of cloud cover. In the Sentinel-2 time-series, for example, the impact of clouds on the spectral signature is made apparent through frequent drops in NDVI; a clear advantage of sUAS technologies is that imaging occurs below the cloud layer.

### Satellite Image Data Acquisition and Preparation

In order to evaluate a comprehensive range of spatial resolutions, this study included commercial satellite data from Planet, SPOT, and Pléiades. Coarser spatial resolution data (i.e., Sentinel-2 20 m spatial resolution) were also included so that a wide range of spatial resolutions would be represented, as well as to demonstrate problems of scale given the size of smallholder farms in Malawi and the heterogeneity of the land.

Every cloud free image over the Ntubwi and Nyambi experimentation farms that was available on the Apollo Mapping web service (Apollo Mapping 2018) was purchased and processed for dates as close to 20 February 2018 as possible (the time of sUAS imagery collection). Those satellites included SPOT 6 (25 March 2018 for Ntubwi) and Pléiades (28 January 2018 for Nyambi); however, the SPOT 6 image was collected after harvest had already taken place and is excluded from analysis but is presented to further demonstrate unexpected timing issues (Figure 5). Planet images were downloaded via the Planet API for 17 February 2018 (Nyambi) and 20 February 2018 (Ntubwi) (Planet Team 2017). Sentinel-2 images were acquired using Google Earth Engine (Gorelick *et al.* 2017) at both sites for 20 February 2018. Georeferencing of the SPOT 6

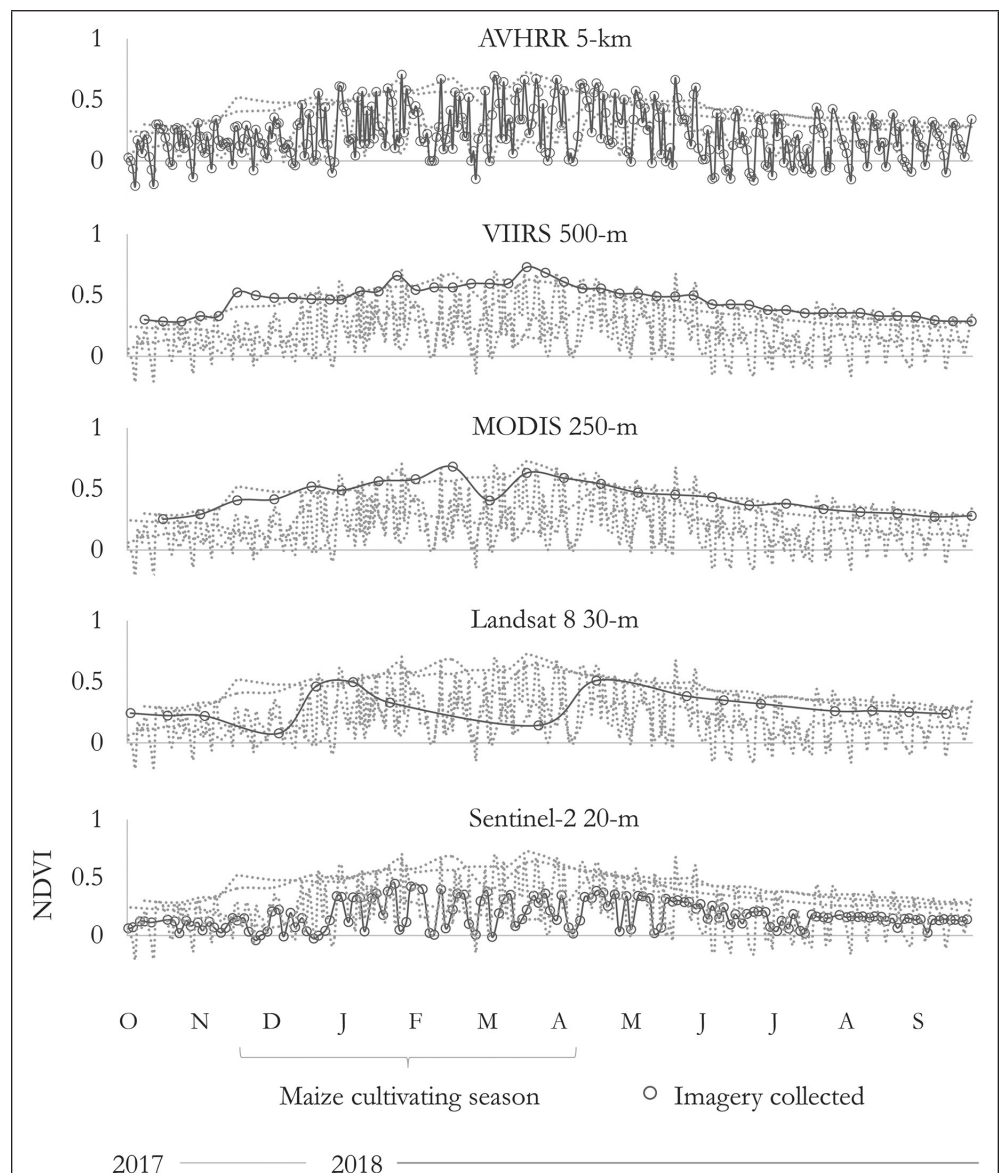


Figure 4. Satellite image NDVI acquisition over the trial farm in Nyambi, Malawi. Hollow circles indicate image collection or image delivery.

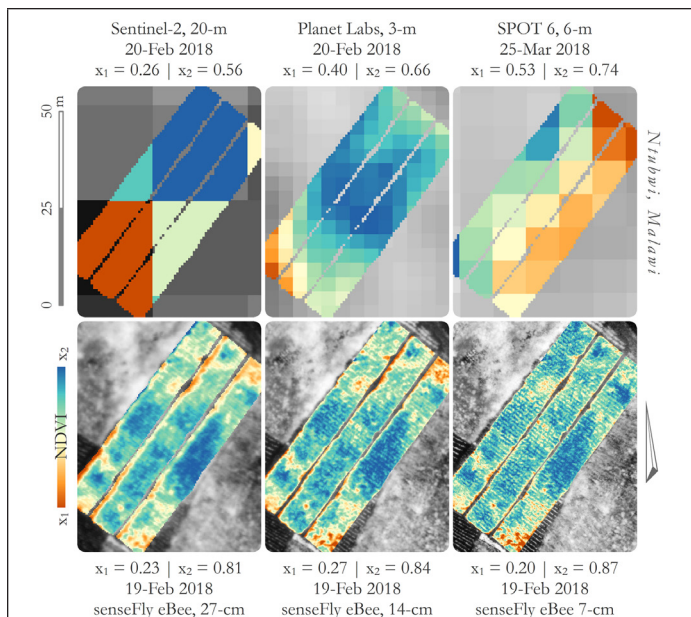


Figure 5. NDVI of the trial farm in Ntubwi across spatial resolutions. Note that min ( $x_1$ ) and max ( $x_2$ ) NDVI are unique to each map.

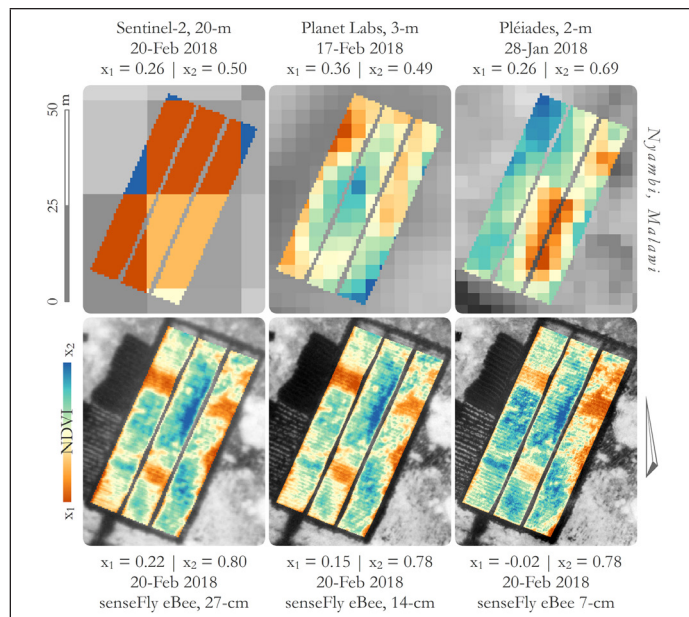


Figure 6. NDVI of the trial farm in Nyambi across spatial resolutions. Note that min ( $x_1$ ) and max ( $x_2$ ) NDVI are unique to each map.

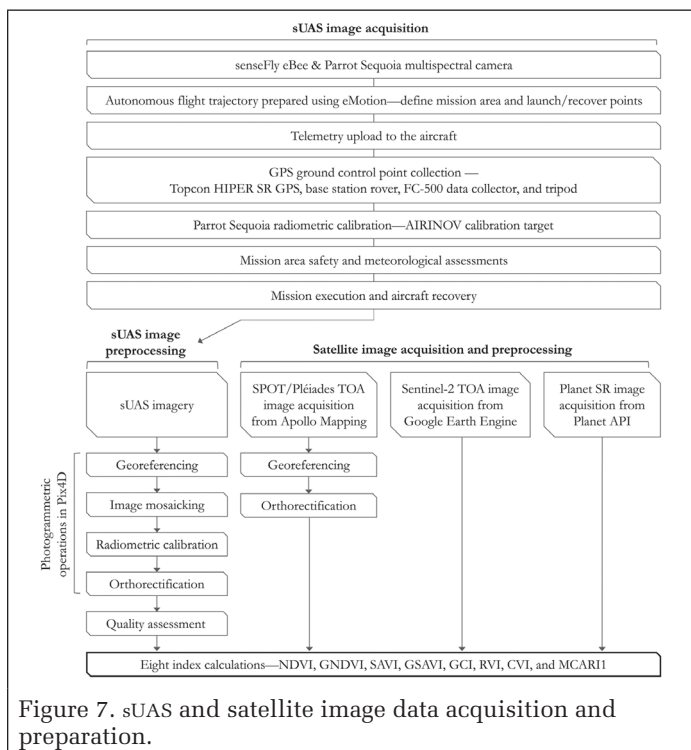


Figure 7. sUAS and satellite image data acquisition and preparation.

and Pléiades imagery was performed using the metadata from the imagery suppliers and orthorectification conducted using SRTM 30 m elevation (Farr *et al.* 2007) in ArcGIS 10.6 (ESRI 2018). Satellite and sUAS image acquisition and preprocessing is outlined in Figure 7.

### sUAS Image Data Acquisition and Preparation

The sUAS missions were conducted using a senseFly eBee agricultural fixed-wing aircraft equipped with a Parrot Sequoia multispectral camera (Parrot SA 2017; senseFly 2014). Three missions were conducted at Nyambi at flight heights of approximately 79, 146, and 276 m above ground level (AGL)

elevation with ground sampling distances (GSD) remaining constant at 6.88 cm, 13.54 cm, and 27.18 cm, respectively. Three missions were also conducted at Ntubwi at flight heights of approximately 83, 136, and 267 m AGL elevation with GSD remaining constant at 7.30 cm, 14.02 cm, and 27.37 cm, respectively.

Image collection occurred at peak overhead sun hours between 1000 and 1400 to minimize effects of shadows. Autonomous flight plans were prepared using eMotion software. Ground control points were set with a Topcon HIPER SR GPS base station with rover, FC-500 data collector, and tripod. The routine for image collection and initial processing in the field followed this sequence: (1) defining the mission area and setting launch/recovery points, (2) aircraft trajectory planning using eMotion flight control software to ensure proper image overlap (senseFly 2014), (3) telemetry upload to the aircraft, (4) GPS ground control point (GCP) collection, (5) mission area safety and meteorological assessments, (6) Parrot Sequoia multispectral camera radiometric calibration using an AIRNOV calibration target, (7) mission execution and recovery, (8) image processing in Pix4D photogrammetric software (mosaicking, georeferencing, radiometric calibration, orthorectification, and resampling to 7 cm, 14 cm, and 27 cm spatial resolutions) (Pix4D SA 2017), (9) data quality assessment and additional postprocessing adjustments such as GCP corrections (transforming approximately 3 m position accuracy to 1.5 cm) (Figure 7). Plates 1 and 2 show the range of imagery spatial resolutions and collection dates for both sites using NDVI as an example.

### Relating Multispectral Indices to On-Farm Measurements

Using spectral bands consistent across all imaging platforms under study (i.e., green, red, and NIR), eight vegetation indices were selected to relate spectral signals with on-farm plant metrics (Table 3). The indices selected included NDVI, GNDVI, SAVI, GSAVI, GCI, RVI, CVI, and MCARI1 (Figure 8).

Index selection was based on *a priori* knowledge of demonstrated relationships between crop status (e.g., crop chlorophyll content and yield) and remote sensing spectral signals. The indices selected are among the most commonly used in precision agriculture contexts, and consideration was given to representation of both red- and green-based spectral indices,

as well as two indices (CVI and MCARI1) that use both the green and red bands in their calculation (Table 3).

NDVI is one of the most commonly used indices for evaluating healthy vegetation (Tucker 1979) and is ubiquitous across precision agriculture applications; however, NDVI is sensitive to high LAI. GNDVI was popularized by Gitelson and Merzlyak (1998) as a metric sensitive to chlorophyll content in leaves and has been used similarly to NDVI as a decision support metric in precision agriculture mapping tools (Candiago *et al.* 2015; Zhang *et al.* 2010); its calculation mimics NDVI, but uses the green band in place of red. SAVI is similar in formulation to NDVI, but uses an adjustment factor to minimize the effects of soil on the spectral signal (Huete 1988); this can be critical in areas where vegetation is sparse or where cropping arrangements (or crop types) allow visibility of the soil beneath the canopy. GSAVI follows the SAVI formula structure but uses

the green band in calculation instead of red; this index has shown to be effective for determining early in-season nitrogen requirements for corn (Sripada *et al.* 2006). CVI and MCARI1 are both indices that use NIR, red, and green in combination. CVI was designed to estimate leaf chlorophyll at the canopy scale while minimizing the effects of LAI variation (Vincini, Frazzi, and D'Alessio 2008). Conversely, MCARI1 has an increased sensitivity to leaf area while also suppressing the sensitivity to chlorophyll (Haboudane *et al.* 2004).

#### Index Calculations and Field Sampling

Indices were calculated using raster calculator in ArcGIS 10.6 and mean values were calculated for each index (across all satellite platforms) at each plot using the zonal statistics tool. Mean statistics were selected for consistency with the field methodology for Soil-Plant Analyses Development (SPAD)

Table 3. Indices, abbreviations, and equations for each index under study. NIR = near infrared; R = red; G = green.

Index	Abbreviation	Equation
Normalized difference vegetation index	NDVI	$(\text{NIR} - \text{R}) / (\text{NIR} + \text{R})$
Green normalized difference vegetation index	GNDVI	$(\text{NIR} - \text{G}) / (\text{NIR} + \text{G})$
Soil adjusted vegetation index	SAVI	$1.5 \times [(\text{NIR} - \text{R}) / (\text{NIR} + \text{R} + 0.5)]$
Green soil adjusted vegetation index	GSAVI	$1.5 \times [(\text{NIR} - \text{G}) / (\text{NIR} + \text{G} + 0.5)]$
Green chlorophyll index	GCI	$(\text{NIR} / \text{G}) - 1$
Ratio vegetation index	RVI	$\text{NIR} / \text{R}$
Chlorophyll vegetation index	CVI	$(\text{NIR} / \text{G}) \times (\text{R} / \text{G})$
Modified chlorophyll absorption ratio index 1	MCARI1	$1.2 \times [2.5 \times (\text{NIR} - \text{R}) - 1.3 \times (\text{NIR} - \text{G})]$

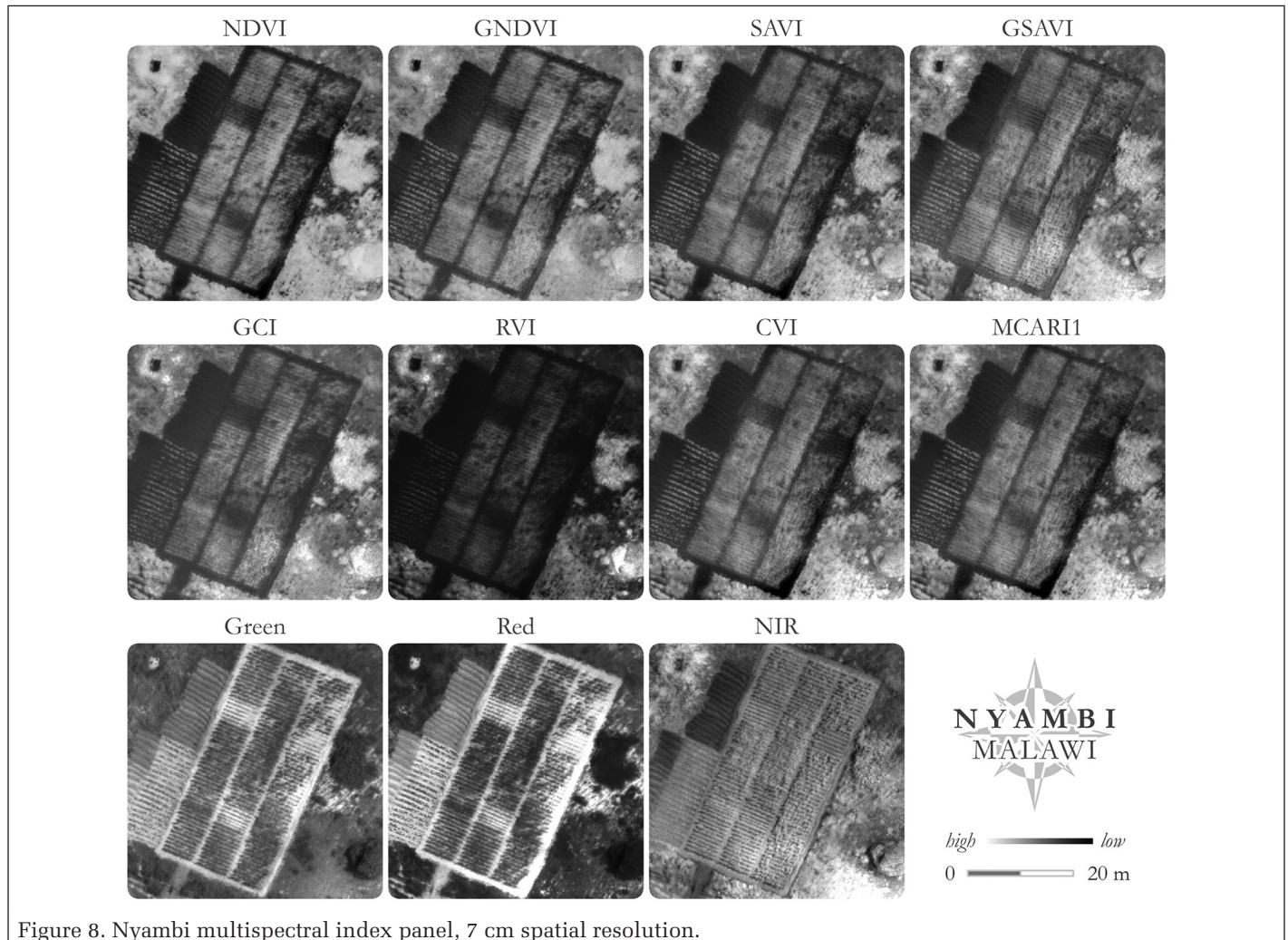


Figure 8. Nyambi multispectral index panel, 7 cm spatial resolution.

chlorophyll content calculations (discussed below) conducted by the agronomy field team maintaining the sites. Satellite images were resampled down to 50 cm so that mean value statistics of the coarse spatial resolution images were relative to the amount of each pixel contained within each plot.

A handheld Soil-Plant Analyses Development (SPAD) 502 Plus Chlorophyll Meter, which returns an index of relative chlorophyll content (calculated using the 650 nm and 940 nm spectral bands) (Spectrum Technologies Inc. 2019), was used to link the imagery with *in situ* measurements. This index is effective for estimating leaf nitrogen concentration in maize (Bullock and Anderson 1998). The average SPAD reading was collected from the center two rows of each plot. The

Table 4. SPAD and yield measurements at the Ntubwi and Nyambi trial farms.

	T1	T2	T3	T4	T5	T6	T7	T8	T9
Ntubwi									
R1									
SPAD	33.2	54.7	55.7	51.9	56.6	53.5	56	52	54.1
Yield	1426	2133	3494	1848	2966	1808	3433	3128	3880
R2									
SPAD	39.6	51.1	56.9	53.6	54.4	54	56	51.6	53
Yield	2033	3169	2600	3067	2336	2986	2377	2397	3006
R3									
SPAD	42.3	53.1	53.3	51.5	54.6	54.6	56.5	55.5	50.9
Yield	911	2113	3433	2275	3250	1727	4063	4834	2945
Nyambi									
R1									
SPAD	24.6	36.8	38.9	43.8	35.7	41.6	39	49.9	34.2
Yield	467	3129	3869	4514	3415	3153	1696	6067	2723
R2									
SPAD	25.9	36.3	39.9	45.8	46.7	44.9	49.5	48.2	43
Yield	467	3105	3798	4347	6950	4228	9172	5876	2651
R3									
SPAD	25.5	42.7	46.4	46.6	54.2	53.9	50.8	58.2	47
Yield	488	6616	5422	6019	6067	5876	5780	9482	6473

T = treatment; R = replicate.

Table 5. Top performing SLR and MLR models as ranked by AICc.

Site	Var.	Res. (m)	R <sup>2</sup>	p-Value	Regression Equation		
Ntubwi	SPAD	0.07	0.196	0.021	S = 37.3 + 2.5(RVI)		
		0.14	0.553	8.7E-6	S = -19.4 + 112.6(GNDVI)		
		0.27	0.495	4.3E-5	S = -1.4 + 94(GNDVI)		
		0.07	0.750	0.033*	S = 491.3 - 76.2(CVI) + 202.7(GCI) - 2314(GNDVI) + 1715.2(GSAVI) - 1010.6(MCARI1) + 939(NDVI) - 64.9(RVI)		
		0.14	0.790	8.7E-5*	S = -252.3 - 48(CVI) + 1498.6(GNDVI) - 622.8(NDVI) - 7.7(RVI)		
		0.27	0.580	0.008*	S = -31.3 + 179.8(GNDVI) - 4.3(RVI)		
	Yield	0.14	0.349	0.001	Y = -4694.2 + 1820.5(CVI)		
		0.27	0.302	0.003	Y = -3599.7 + 16880.1(GSAVI)		
		Nyambi	SPAD	0.07	0.283	0.004	S = 3.8 + 74.6(GNDVI)
				0.14	0.476	6.9E-5	S = 7.9 + 71.6(NDVI)
0.27	0.607			1.7E-6	S = -16.2 + 160.1(GSAVI)		
3	0.165			0.035	S = -61.1 + 288.5(GSAVI)		
0.14	0.546			0.020*	S = 31.3 - 128(GSAVI) + 176(MCARI1)		
0.27	0.720			3.8E-4*	S = -50.8 + 235.6(GNDVI) + 69.2(MCARI1) - 13(RVI)		
Yield	0.07	0.226	0.012	Y = -5068.4 + 18407.3(GNDVI)			
	0.14	0.464	9.1E-5	Y = -4944.7 + 19526(NDVI)			
	0.27	0.637	6.1E-7	Y = -12112.7 + 45275.7(GSAVI)			
	3	0.157	0.041	Y = -17753.2 + 69123.8(SAVI)			
	20	0.147	0.049	Y = -2103.8 + 31495(MCARI1)			
	0.27	0.677	3.2E-4*	Y = -18049.5 + 6263.3(CVI) + 19556.8(MCARI1)			

\*Bonferroni correction applied. S = SPAD; Y = yield. Only models of  $p < 0.05$  are included in this listing.

rationale for selecting plants near the center of each plot was to minimize influence from neighboring plots that underwent different fertilizer treatments. Yield measurements were also collected for each plot (Table 4).

### MLR Permutations and Model Rankings

Hatfield and Prueger (2010) argue that using a collection of indices to quantify agricultural status can be more effective than selecting a single index. To correlate the remote sensing indices with crop status, tests were performed on every possible MLR permutation between the remote sensing indices selected (independent variables) and the on-farm measurements (SPAD and yield as dependent variables). A principal component analysis was also conducted, but no significant groupings emerged due to the inherent collinearity among the variables under study. In addition to multiple regression, tests were conducted using stepwise regression, partial least squares regression, and a classification and regression tree approach. Ultimately, the multiple regression approach was selected to maximize potential linear relationships while maintaining model parsimony. The following is the global MLR model:

$$\hat{Y} = b_0 + b_1 \text{NDVI} + b_2 \text{GNDVI} + b_3 \text{SAVI} + b_4 \text{GSAVI} + b_5 \text{GCI} + b_6 \text{RVI} + b_7 \text{CVI} + b_8 \text{MCARI1},$$

where  $\hat{Y}$  is SPAD or yield.

The Multi-Model Inference (MuMIn) package in R (Barton 2009) was used to generate the permutations, which produced 256 MLR equations per imagery spatial resolution. Models were then ranked according to AICc, which aims for a parsimonious balance of predictive power and model simplicity that also adjusts for model overfitting or underfitting (Akaike 1974). Additionally, the Bonferroni Correction (Bonferroni 1935) was applied to the multiple regression permutation  $p$ -values to adjust again for model overfitting. The Bonferroni Correction method selected involved simply multiplying each  $p$ -value by the number of permutations ( $N = 256$ ), which was done using *p.adjust* in R. The top performing models from these tests are listed in Table 5.

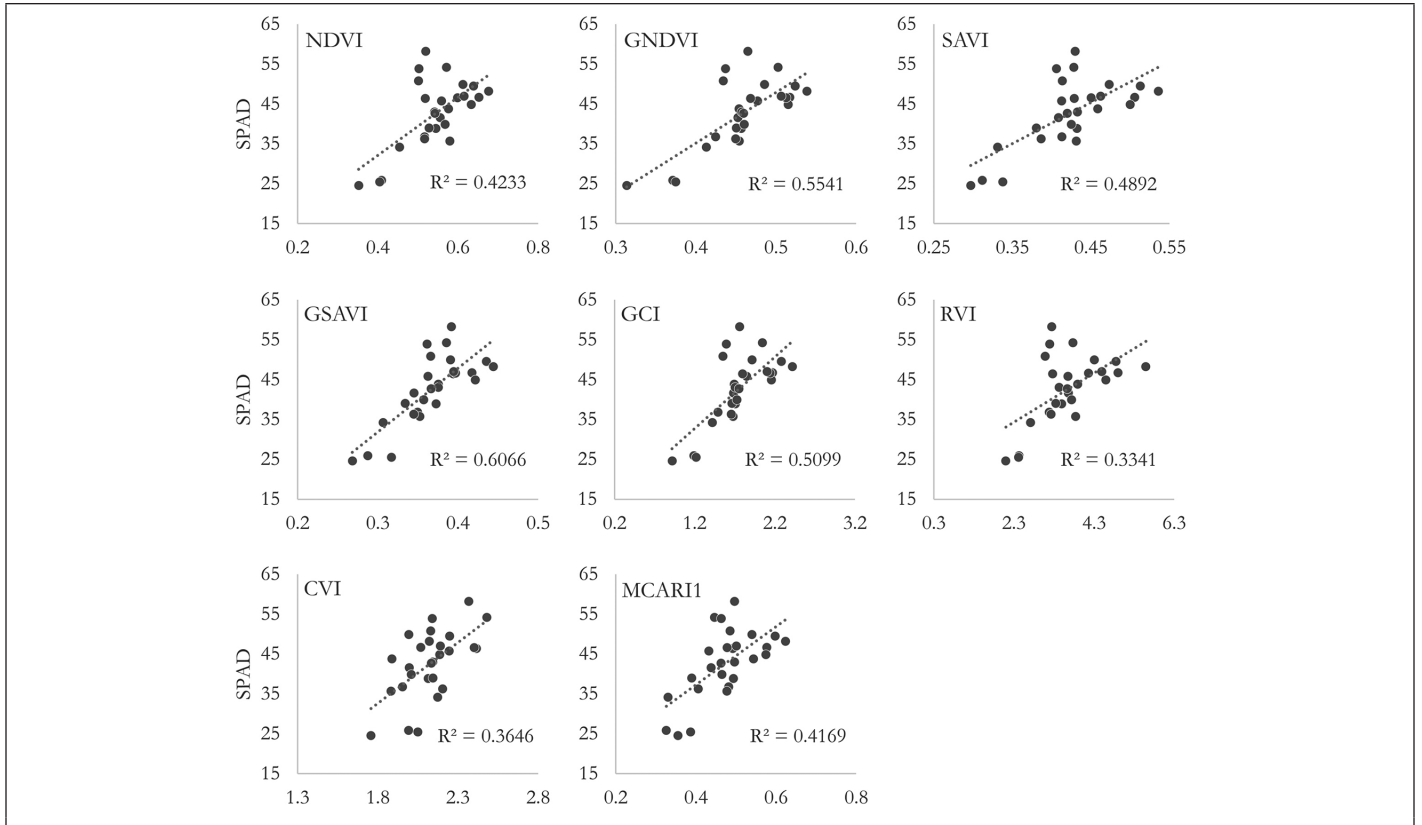


Figure 9. Example SLR—SPAD and spectral indices. Nyambi, senseFly eBee Parrot Sequoia 27 cm spatial resolution.

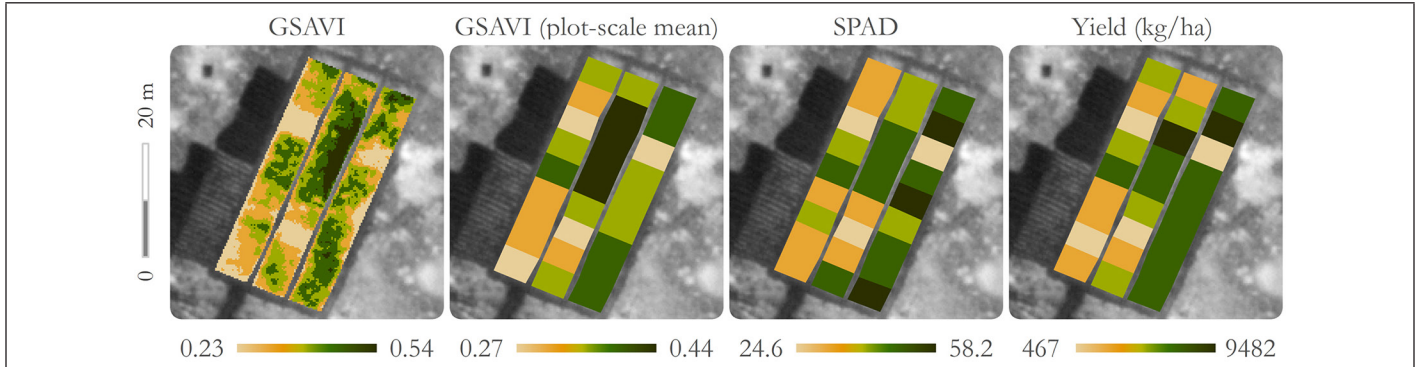


Figure 10. GSAVI 27 cm spatial resolution grid at Nyambi, scaled to the plot level and compared to on-farm measurements of SPAD and yield.

**Results and Discussion**

**SLR Results**

One example of the SLR tests is presented in Figure 9 to illustrate the relationships between proximal farm measurements and spectral signals derived from the sUAS images. This example is from the senseFly eBee/Parrot Sequoia multispectral camera at a spatial resolution of 27 cm at Nyambi. The index with the highest R<sup>2</sup> in this particular case is GSAVI (R<sup>2</sup> = 0.607), followed by GNDVI (R<sup>2</sup> = 0.554), GCI (R<sup>2</sup> = 0.510), and SAVI (R<sup>2</sup> = 0.489). Contrary to popular use, NDVI does not rank among the top four, but ranks fifth with an R<sup>2</sup> of 0.423. Interestingly, the green band is in each of the top three index calculations. This evidence is consistent with other studies that have found green-band indices critical for accurately predicting crop health (Sripada *et al.* 2006; Shanahan 2001; Gitelson and Merzlyak 1998). Early assessments of the green spectral range have also noted the value of this band for evaluating crops with a moderately high leaf area index (Gitelson, Kaufman,

and Merzlyak 1996), as was the case with the tropical maize crop in this study. Overall, these R<sup>2</sup> values fall below those produced with the MLR models, echoing the argument from Hatfield and Prueger (2010) that a multivariable approach to predicting farm yields from remote sensing spectral indices is the optimal route. Given these findings and the abundance of literature reiterating the value of a broader range of spectral indices (Hatfield and Prueger 2010; Mulla 2013), precision agriculture and sUAS developers would benefit from diversifying their marketed indices and integrate green-based indices alongside NDVI. The 27 cm spatial resolution GSAVI image at Nyambi is mapped in Figure 10, scaled to the plot level, and compared to the on-farm measurements of SPAD and yield. **MLR Results** The second test consisted of all possible MLR permutations of the indices under study. From the collection of multiple regression permutations, the top performing models across all

of the imaging platforms were extracted to compare spatial resolutions with maximum correlative strength (Table 5). Each regression model presented has a  $p$ -value less than 0.05. MLR models are only presented if the SLR was outperformed. At Ntubwi, the highest  $R^2$  (0.553) for SPAD (SLR) was at a spatial resolution of 14 cm with GNDVI. The highest  $R^2$  (0.790) overall for SPAD was at a spatial resolution of 14 cm in an MLR with CVI, GNDVI, NDVI, and RVI.

SLR models for SPAD at a 7 cm spatial resolution at Ntubwi did not perform well, with the top performing model returning an  $R^2$  of 0.196 using RVI. The highest  $R^2$  (0.349) for yield at Ntubwi was at a spatial resolution of 14 cm using CVI; 0.27 cm spatial resolution ranked second ( $R^2 = 0.302$ ) with GSAVI, and there was no statistically significant relationship between yield and spectral indices at a 7 cm spatial resolution at this site ( $p > 0.05$ ). Somewhat surprisingly, the top performing MLR at 7 cm spatial resolution for SPAD at Ntubwi returned a high  $R^2$  of 0.750; however, this MLR equation required seven out of the eight selected indices. At Ntubwi, neither Sentinel-2 nor Planet returned significant relationships with SPAD or yield.

At Nyambi the highest  $R^2$  (0.607) for SPAD (SLR) was at a spatial resolution of 27 cm with GSAVI. The highest  $R^2$  (0.720) overall for SPAD was at a spatial resolution of 27 cm in an MLR with GNDVI, MCARI1, and RVI. SLR models for SPAD at a 7 cm spatial resolution at Nyambi also did not perform well, with the top performing model returning an  $R^2$  of 0.283 using GNDVI. In contrast to Ntubwi, there was no significant MLR model for SPAD at Nyambi at the 7 cm spatial resolution. At Nyambi, Planet (3 m spatial resolution) GSAVI emerged as statistically significant ( $p < 0.05$ ), but with an  $R^2$  of only 0.165. At Nyambi, neither Sentinel-2 nor Pléiades returned statistically significant relationships with SPAD.

At Nyambi, there were more statistically significant relationships between spectral indices and yield than at Ntubwi. The highest  $R^2$  (0.637) for yield (SLR) at Nyambi was at a spatial resolution of 27 cm using GSAVI. The top performing model overall was at a 27 cm spatial resolution using MLR with CVI and MCARI1 ( $R^2 = 0.677$ ). Planet and Sentinel-2 emerged with statistically significant relationships to yield at Nyambi ( $p < 0.05$ ), but both with  $R^2 < 0.2$ . The results of these tests are plotted in Figure 11.

### Summary of Findings

The primary objective of this research was to quantify the effective spatial resolutions for conducting precision agriculture

on smallholder farms in Malawi. Based on the weak correlations drawn from the satellite imagery, the abundance of cloud cover, and infrequent satellite revisit rates, it is clear that sUAS are the optimal platforms for evaluating intrafarm variability in this context. Figure 12 includes all SLR models ( $p < 0.05$ ) and the top performing SLR/MLR models. Illustrated in this figure is a substantial drop in the statistical relationship between spectral index and on-farm measurements at the satellite scale. While the satellite spatial resolutions ranged from 2 m to 20 m, Pléiades, Planet, and Sentinel-2 all fell below an  $R^2$  of 0.2. The relationship at the sUAS scale varied substantially depending on the index and spatial resolution, generally ranging between  $R^2$  values of 0.2 to 0.6, with some instances nearing zero, while MLR models reached upwards of approximately 0.8. The second and fourth scatterplots show the regression model  $R^2$  values at the sUAS scale (7–27 cm). This visualization demonstrates that the relationship between crop status and spectral signals varies substantially even at fine scales.

It is clear that the 14 cm and 27 cm spatial resolutions are more effective than 7 cm for relating spectral indices with proximal farm measurements in this particular case. Interestingly, resampling from 7 cm to 14 cm and 27 cm did not produce an increased correlation—there was minimal distinguishable change. These findings are somewhat consistent with a hydrological study by Beene, Zhang, and Paulus (2019) that evaluated the effect of pixel size on modeling water velocity, depth, and surface elevation; in this analysis the original imagery was 2 cm spatial resolution and presumably resampled to 100 cm in increments of 14 cm. Pixel size was found to be a strong predictor of surface elevation variation, a marginal predictor for marginal depth, and there was no clear trend for maximum velocity (Beene, Zhang, and Paulus 2019). As in the study presented here, it may be the case that initial image collection GSD has a greater impact on model outcomes than coarsening spatial resolutions by resampling.

To evaluate the impact of soil and shadow on the relationship between on-farm measurements and spectral indices derived from the sUAS images, a linear regression test with soil/shadows removed was also tested. As shown in Figure 12,  $R^2$  values obtained from the models with soil and shadow removal were higher than those models without soil and shadow removal, indicating that soil and shadow removal can improve model performance. However,  $R^2$  values obtained from the models using 7 cm spatial resolution images

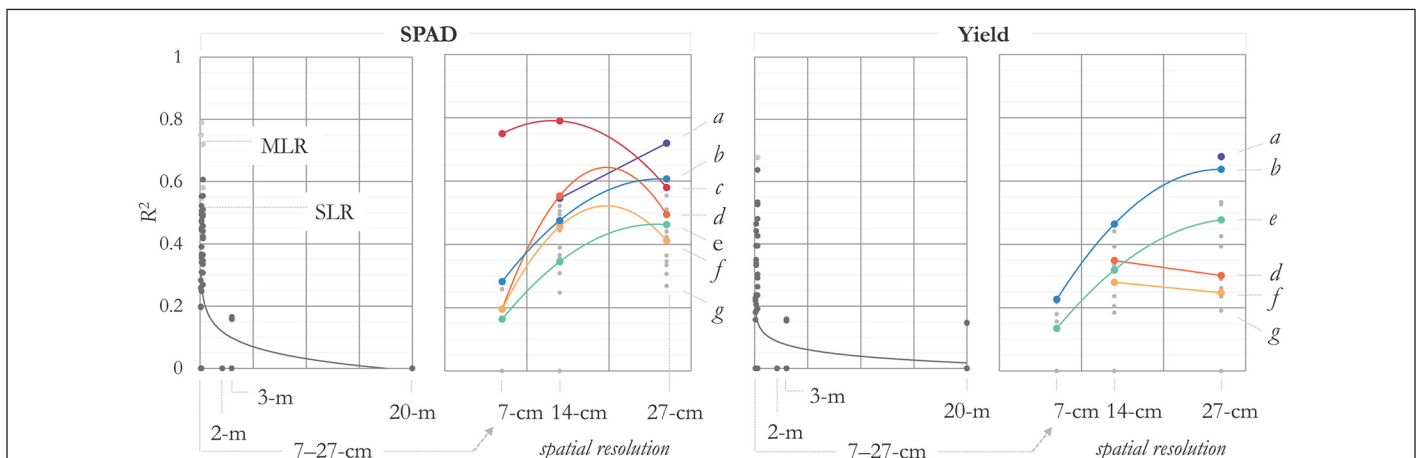


Figure 11. Comparing linear regression correlations of spectral indices and on-farm measurements across spatial resolutions. (a) Nyambi top performing MLR models (depicted in purple), (b) Nyambi top performing SLR models (depicted in blue), (c) Ntubwi top performing MLR models (depicted in red), (d) Ntubwi top performing SLR models (orange), (e) Nyambi mean SLR models (depicted in green), (f) Ntubwi mean SLR models (depicted in yellow), and (g) all SLR models (depicted in gray). Left panel: SPAD; right panel: yield. Only models with  $p < 0.05$  are included in this display.

were still significantly smaller than those of the 14 cm or 27 cm spatial resolution images. Therefore, for a generalizable methodology, imaging at a leaf-scale spatial resolution may not be more effective than imaging at a plant-scale spatial resolution. Outcomes of this study suggest that a GSD close to the plant dimensions is the optimal spatial resolution for relating spectral signatures to plant productivity. A recent study examining maize plant stands at different sUAS flight heights found evidence as well that the distance between maize plants was discerned more accurately when imaged at greater flight heights, producing a better resolved image in the presence of overlapping leaves among close-spaced plants (Zhang *et al.* 2018).

## Conclusions

This study examined a range of spatial resolution imagery over two smallholder farms in the central region of Malawi—Nyambi and Ntubwi in the district of Machinga. The imagery under analysis was Sentinel-2 (20 m), SPOT 6 (6 m), Planet (3 m), Pléiades (2 m), and sUAS (7 cm, 14 cm, and 27 cm). A heuristic was developed to generate a collection of precision agriculture spectral indices from the initial set of spectral bands and evaluate MLR permutations of the selected indices and proximal measurements in the field (crop chlorophyll content and crop yield).

SLR and MLR were performed for all possible permutations of the indices selected. The results show that the correlation between on-farm measurements and remote sensing spectral signals decreases substantially at 2 m, 3 m, and 20 m spatial resolutions. For precision agriculture, the problems of clouds, satellite revisit rates, and spatial resolutions are hurdles that have not yet been overcome with governmental and commercial satellite imagery for the smallholder farming context. For larger fields, coarser spatial resolutions may be adequate, but they were insufficient for the size of the field experimented in this study. A novel insight from this study is that the top performing SPAD and yield models were associated with the 14 cm and 27 cm spatial resolution imagery, rather than the 7 cm spatial resolution. This is potentially a product of a fractal problem where more pixels in turn means a greater number of pixels contain mixed soil and shadow. One hypothesis in this regard is that initial image collection at the spatial resolution of the plant dimensions might be the most effective. In this case, 14–27 cm is closer to the maize plant size than 7 cm.

It was also determined that GNDVI and GSAVI were consistent indices for relating spectral images to proximal farm measurements. These findings suggest that green-band indices

are critical to test when monitoring crop production via sUAS. Outcomes of this research are consistent with other studies that have found that considering a broad range of indices may be more effective for monitoring crop health and productivity than selecting a single index; however, the specific set of indices appropriate for a given farm may vary. Finally, precision agriculture can add value to smallholder farming environments in semiarid Africa; however, there are substantial limitations to obtaining sUAS imagery across vast geographic extents and scaling these technologies may require institutional investments moving forward.

## Acknowledgments

This paper is made possible by the support of the American People provided to the Feed the Future Innovation Lab for Sustainable Intensification through the United States Agency for International Development (USAID). The contents are the sole responsibility of the authors and do not necessarily reflect the views of USAID or the United States Government. Program activities are funded by USAID under Cooperative Agreement No. AID-OAA-L-14-00006. The authors wish to thank the American Society for Photogrammetry and Remote Sensing and those affiliated with the Robert N. Colwell Memorial Fellowship for their support. The authors also wish to thank Africa RISING and the Lilongwe University of Agriculture and Natural Resources (LUANAR) for collaboration in on-farm research activities, as well as the Global Change Learning Lab in Sub-Saharan Africa at Michigan State University for their involvement. Additional gratitude is extended to Planet's Education and Research Program for supplying access to their imagery archive. At the time of research, Brad G. Peter and Joseph P. Messina were with Michigan State University, Department of Geography, Environment, and Spatial Sciences, East Lansing, Mich., Junjun Zhi was with Michigan State University, Center for Global Change and Earth Observations, East Lansing, Mich., and Vimbayi Chimonyo was with Michigan State University, Department of Plant, Soil, and Microbial Sciences, East Lansing, Mich.

## References

- Airbus Defence and Space. 2012a. SPOT 6. <<https://www.intelligence-airbusds.com/en/8693-spot-67>> Accessed 23 October 2019.
- Airbus Defence and Space. 2012b. Pléiades. <<https://www.intelligence-airbusds.com/en/8692-pleiades>> Accessed 23 October 2019.

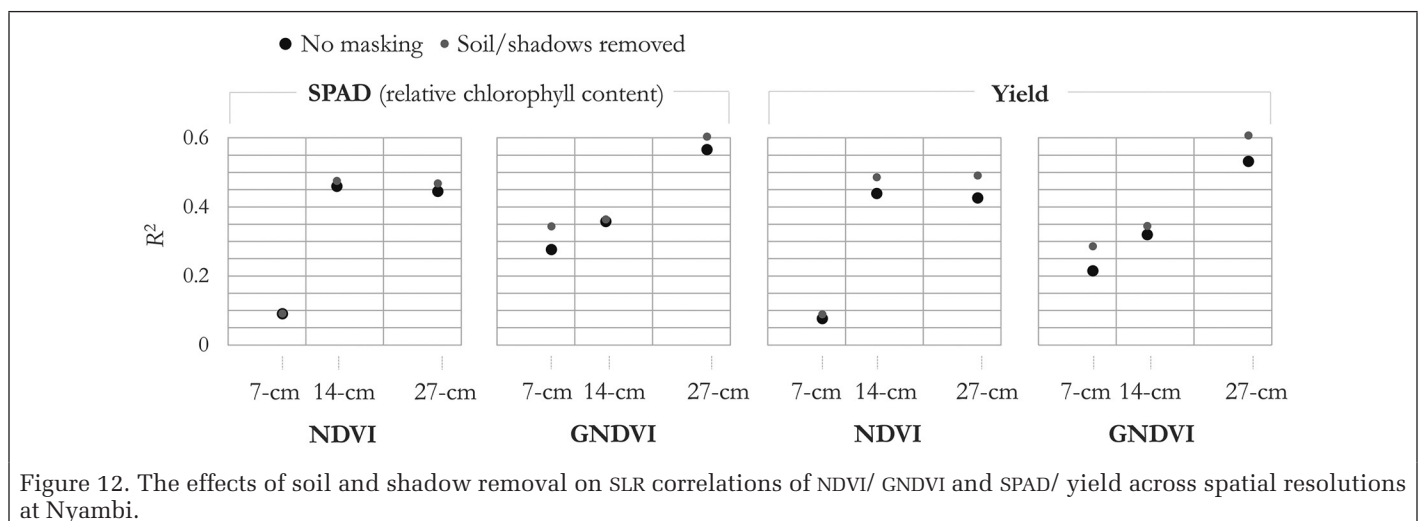


Figure 12. The effects of soil and shadow removal on SLR correlations of NDVI/ GNDVI and SPAD/ yield across spatial resolutions at Nyambi.

- Akaike, H. 1974. A new look at the statistical model identification. In *Selected Papers of Hirotugu Akaike*, edited by E. Parzen, K. Tanabe, and G. Kitagawa, 215–222. New York, N.Y.: Springer.
- Apollo Mapping. 2018. Apollo mapping: The image hunters. <apollomapping.com/> Accessed 12 September 2019.
- Babu, S. and P. Sanyal. 2018. Persistent food insecurity from policy failures in Malawi (7–2). In *Case Studies in Food Policy for Developing Countries: Domestic Policies for Markets, Production, and Environment*, edited by P. Pinstrup-Andersen and F. Cheng, vol. 2, 149–160. Ithaca, N.Y.: Cornell University Press..
- Barton, K. 2009. MuMIn: Multi-model inference. <<http://r-forge.r-project.org/projects/mumin/>> Accessed 12 September 2019.
- Basso, B., J. T. Ritchie, F. J. Pierce, R. P. Braga and J. W. Jones. 2001. Spatial validation of crop models for precision agriculture. *Agricultural Systems* 68 (2):97–112.
- Beene, D., S. Zhang and G. Paulus. 2019. Workflow for hydrologic modelling with sUAS-acquired aerial imagery. *Geocarto International* 1–19.
- Bonferroni, C. E. 1935. Il calcolo delle assicurazioni su gruppi di teste. *Studi in onore del professore salvatore ortu carboni*, 13–60.
- Bullock, D. G. and D. S. Anderson. 1998. Evaluation of the Minolta SPAD 502 chlorophyll meter for nitrogen management in corn. *Journal of Plant Nutrition* 21 (4):741–755.
- Candiago, S., F. Remondino, M. De Giglio, M. Dubbini and M. Gattelli. 2015. Evaluating multispectral images and vegetation indices for precision farming applications from UAV images. *Remote Sensing* 7 (4):4026–4047.
- Cassman, K. G., A. Dobermann and D. T. Walters. 2002. Agroecosystems, nitrogen-use efficiency, and nitrogen management. *AMBIO: A Journal of the Human Environment* 31 (2):132–141.
- Ceccato, P., S. Flasse, S. Tarantola, S. Jacquemoud and J. M. Grégoire. 2001. Detecting vegetation leaf water content using reflectance in the optical domain. *Remote Sensing of Environment* 77 (1):22–33.
- DigitalGlobe. 2009. WorldView-2. <<https://dgv4-cms-production.s3.amazonaws.com/uploads/document/file/130/WorldView2-DS-WV2-rev2.pdf>> Accessed 23 October 2019.
- Dlodlo, N. and J. Kalezhi. 2015. The internet of things in agriculture for sustainable rural development. Pages 13–18 in *Proceedings of the IEEE International Conference on Emerging Trends in Networks and Computer Communications (ETNCC)*.
- Eaton, R., J. Katupitiya, K. W. Siew and K. S. Dang. 2008. Precision guidance of agricultural tractors for autonomous farming. Pages 1–8 in *Proceedings of the 2008 2nd Annual IEEE Systems Conference*.
- ESA. 2015. Copernicus Sentinel: Sentinel-2 MSI: MultiSpectral instrument, level-1C. ASF DAAC. <<https://earth.esa.int/web/sentinel/user-guides/sentinel-2-msi/product-types/level-1c>> Accessed 12 September 2019.
- ESRI. 2018. ArcGIS Desktop: Release 10.6. Redlands, Calif.: Environmental Systems Research Institute.
- Farr, T. G., P. A. Rosen, E. Caro, R. Crippen, R. Duren, S. Hensley, M. Kobrick, M. Paller, E. Rodriguez, L. Roth, D. Seal, S. Shaffer, J. Shimada, J. Umland, M. Werner, M. Oskin, D. Burbank and D. Alsdorf. 2007. The shuttle radar topography mission. *Reviews of Geophysics* 45:RG2004.
- Floreano, D. and R. J. Wood. 2015. Science, technology and the future of small autonomous drones. *Nature* 521 (7553):460.
- Franke, A. C., G. J. van den Brand and K. E. Giller. 2014. Which farmers benefit most from sustainable intensification? An ex-ante impact assessment of expanding grain legume production in Malawi. *European Journal of Agronomy* 58:28–38.
- Gao, B. 1996. NDWI—A normalized difference water index for remote sensing of vegetation liquid water from space. *Remote Sensing of Environment* 58 (3):257–266.
- Giller, K. E., E. C. Rowe, N. de Ridder and H. van Keulen. 2006. Resource use dynamics and interactions in the tropics: Scaling up in space and time. *Agricultural Systems* 88 (1):8–27.
- Gitelson, A. A., Y. J. Kaufman and M. N. Merzlyak. 1996. Use of a green channel in remote sensing of global vegetation from EOS-MODIS. *Remote Sensing of Environment* 58 (3):289–298.
- Gitelson, A. A. and M. N. Merzlyak. 1998. Remote sensing of chlorophyll concentration in higher plant leaves. *Advances in Space Research* 22 (5):689–692.
- Gorelick, N., M. Hancher, M. Dixon, S. Ilyushchenko, D. Thau and R. Moore. 2017. Google Earth Engine: Planetary-scale geospatial analysis for everyone. *Remote Sensing of Environment* 202:18–27.
- Gyssels, G. and J. Poesen. 2003. The importance of plant root characteristics in controlling concentrated flow erosion rates. *Earth Surface Processes and Landforms: The Journal of the British Geomorphological Research Group* 28 (4):371–384.
- Haboudane, D., J. R. Miller, E. Pattey, P. J. Zarco-Tejada and I. B. Strachan. 2004. Hyperspectral vegetation indices and novel algorithms for predicting green LAI of crop canopies: Modeling and validation in the context of precision agriculture. *Remote Sensing of Environment* 90 (3):337–352.
- Hatfield, J. L. and J. H. Prueger. 2010. Value of using different vegetative indices to quantify agricultural crop characteristics at different growth stages under varying management practices. *Remote Sensing* 2 (2):562–578.
- Hengl, T. 2006. Finding the right pixel size. *Computers & Geosciences* 32 (9):1283–1298.
- Huete, A. R. 1988. A soil-adjusted vegetation index (SAVI). *Remote Sensing of Environment* 25 (3):295–309.
- Hunt Jr., E. R. and C. S. Daughtry. 2018. What good are unmanned aircraft systems for agricultural remote sensing and precision agriculture? *International Journal of Remote Sensing* 39 (15–16):5345–5376.
- Jain, M., P. Mondal, G. Galford, G. Fiske and R. DeFries. 2017. An automated approach to map winter cropped area of smallholder farms across large scales using MODIS imagery. *Remote Sensing* 9 (6):566.
- Jayne, T. S., J. Chamberlin, L. Traub, N. Sitko, M. Muyanga, F. K. Yeboah, W. Anseeuw, A. Chapoto, A. Wineman, C. Nkonde and R. Kachule. 2016. Africa's changing farm size distribution patterns: The rise of medium-scale farms. *Agricultural Economics* 47 (S1):197–214.
- Jiang, Z., A. R. Huete, J. Chen, Y. Chen, J. Li, G. Yan and X. Zhang. 2006. Analysis of NDVI and scaled difference vegetation index retrievals of vegetation fraction. *Remote Sensing of Environment* 101 (3):366–378.
- Lippitt, C. D. and S. Zhang. 2018. The impact of small unmanned airborne platforms on passive optical remote sensing: A conceptual perspective. *International Journal of Remote Sensing* 39 (15–16):4852–4868.
- Lowder, S. K., J. Skoet and T. Raney. 2016. The number, size, and distribution of farms, smallholder farms, and family farms worldwide. *World Development* 87:16–29.
- Macdonald, R. 1984. A summary of the history of the development of automated remote sensing for agricultural applications. *IEEE Transactions on Geoscience and Remote Sensing* 6:473–482.
- Matese, A., P. Toscano, S. Di Gennaro, L. Genesio, F. Vaccari, J. Primicerio, C. Belli, A. Zaldei, R. Bianconi and B. Gioli. 2015. Intercomparison of UAV, aircraft and satellite remote sensing platforms for precision viticulture. *Remote Sensing* 7 (3):2971–2990.
- McFeeters, S. K. 1996. The use of the normalized difference water index (NDWI) in the delineation of open water features. *International Journal of Remote Sensing* 17 (7):1425–1432.
- Mesas-Carrascosa, F. J., J. Torres-Sánchez, I. Clavero-Rumbao, A. García-Ferrer, J. M. Peña, I. Borra-Serrano and F. López-Granados. 2015. Assessing optimal flight parameters for generating accurate multispectral orthomosaics by UAV to support site-specific crop management. *Remote Sensing* 7 (10):12793–12814.
- Mulla, D. J. 2013. Twenty five years of remote sensing in precision agriculture: Key advances and remaining knowledge gaps. *Biosystems Engineering* 114 (4):358–371.

- NASA LP DAAC. 2015a. VIIRS vegetation indices (VNP13A1) version 1. NASA EOSDIS Land Processes DAAC, USGS Earth Resources Observation and Science (EROS) Center, Sioux Falls, S.D.. <<https://lpdaac.usgs.gov/products/vnp13a1v001/>> Accessed 12 September 2019.
- NASA LP DAAC. 2015b. MODIS normalized difference vegetation index (MOD13Q1) version 006. NASA EOSDIS Land Processes DAAC, USGS Earth Resources Observation and Science (EROS) Center, Sioux Falls, S.D.. <<https://lpdaac.usgs.gov/products/mod13q1v006/>> Accessed 12 September 2019.
- National Statistical Office of Malawi (NSO). 2012. Malawi integrated household survey (2010–2011) (IHS3) Report—Household socio-economic characteristics report. Zomba, Malawi, Republic of Malawi.
- Ngcoya, M. and N. Kumarakulasingam. 2017. The lived experience of food sovereignty: Gender, indigenous crops and small-scale farming in Mtubatuba, South Africa. *Journal of Agrarian Change* 17 (3):480–496.
- Pajares, G. 2015. Overview and current status of remote sensing applications based on unmanned aerial vehicles (UAVs). *Photogrammetric Engineering & Remote Sensing* 81 (4):281–330.
- Panda, S. S., D. P. Ames and S. Panigrahi. 2010. Application of vegetation indices for agricultural crop yield prediction using neural network techniques. *Remote Sensing* 2 (3):673–696.
- Parrot Drones SA. 2017. Parrot Sequoia technical specifications. <<https://www.parrot.com/business-solutions-us/parrot-professional/parrot-sequoia/>> Accessed 27 October 2019.
- Peña, J. M., J. Torres-Sánchez, A. I. de Castro, M. Kelly and F. López-Granados. 2013. Weed mapping in early-season maize fields using object-based analysis of unmanned aerial vehicle (UAV) images. *PLoS One* 8 (10):e77151.
- Pineux, N., J. Lisein, G. Swerts, C. L. Biélders, P. Lejeune, G. Colinet and A. Degré. 2017. Can DEM time series produced by UAV be used to quantify diffuse erosion in an agricultural watershed? *Geomorphology* 280:122–136.
- Pix4D SA. 2017. Pix4Dmapper 4.1 user manual. Lausanne, Switzerland: Pix4D SA.
- Planet Team. 2017. Planet application program interface: In space for life on Earth. San Francisco, Calif. <<https://developers.planet.com/docs/api/>> Accessed 12 September 2019.
- Saari, H., A. Akujärvi, C. Holmlund, H. Ojanen, J. Kaivosoja, A. Nissinen and O. Niemeläinen. 2017. Visible, very near IR and short wave IR hyperspectral drone imaging system for agriculture and natural water applications. *International Archives of the Photogrammetry, Remote Sensing and Spatial Information Science* 42:165–170.
- Sawyer, J. E. 1994. Concepts of variable rate technology with considerations for fertilizer application. *Journal of Production Agriculture* 7 (2):195–201.
- senseFly. 2014. eBee classic—The professional mapping drone. Lausanne, Switzerland: senseFly Parrot Group. <<https://www.sensefly.com/drone/ebee-mapping-drone/>> Accessed 27 October 2019.
- Shanahan, J. F., J. S. Schepers, D. D. Francis, G. E. Varvel, W. W. Wilhelm, J. M. Tringe, M. R. Schlemmer and D. J. Major. 2001. Use of remote-sensing imagery to estimate corn grain yield. *Agronomy Journal* 93 (3):583–589.
- Spectrum Technologies Inc. 2019. SPAD 502 plus chlorophyll meter. <<https://www.specmeters.com/nutrient-management/chlorophyll-meters/chlorophyll/spad502p/>> Accessed 12 September 2019.
- Sripada, R. P., R. W. Heiniger, J. G. White and A. D. Meijer. 2006. Aerial color infrared photography for determining early in-season nitrogen requirements in corn. *Agronomy Journal* 98 (4):968–977.
- Stark, B., M. McGee and Y. Chen. 2015. Short wave infrared (SWIR) imaging systems using small Unmanned Aerial Systems (sUAS). Pages 495–501 in the *Proceedings of the 2015 International Conference on Unmanned Aircraft Systems (ICUAS)*.
- Tucker, C. J. 1979. Red and photographic infrared linear combinations for monitoring vegetation. *Remote Sensing of Environment* 8 (2):127–150.
- USGS. 2013. Landsat 8 surface reflectance tier 1. USGS Earth Resources Observation and Science (EROS) Center, Sioux Falls, S.D.. <<https://www.usgs.gov/land-resources/nli/landsat/landsat-surface-reflectance>> Accessed 12 September 2019.
- Vermote, E., C. Justice, I. Csiszar, J. Eidenshink, R. Myneni, F. Baret, E. Masuoka, R. Wolfe, M. Claverie and NOAA CDR Program. 2014. NOAA climate data record (CDR) of normalized difference vegetation index (NDVI), version 4. NOAA National Climatic Data Center.
- Vincini, M., E. Frazzi and P. D'Alessio. 2008. A broad-band leaf chlorophyll vegetation index at the canopy scale. *Precision Agriculture* 9 (5):303–319.
- Wall, L., D. Larocque and P. M. Léger. 2008. The early explanatory power of NDVI in crop yield modelling. *International Journal of Remote Sensing* 29 (8):2211–2225.
- Williams, P. A., O. Crespo, M. Abu and N. P. Simpson. 2018. A systematic review of how vulnerability of smallholder agricultural systems to changing climate is assessed in Africa. *Environmental Research Letters* 13 (10):103004
- Zhang, X., L. Shi, X. Jia, G. Seielstad and C. Helgason. 2010. Zone mapping application for precision-farming: a decision support tool for variable rate application. *Precision Agriculture* 11 (2):103–114.
- Zhang, C. and J. M. Kovacs. 2012. The application of small unmanned aerial systems for precision agriculture: A review. *Precision Agriculture* 13 (6):693–712.
- Zhang, J., B. Basso, R. F. Price, G. Putman and G. Shuai. 2018. Estimating plant distance in maize using unmanned aerial vehicle (UAV). *PLoS One* 13 (4):e0195223.
- Zhu, Y., W. Wang and X. Yao. 2012. Estimating leaf nitrogen concentration (LNC) of cereal crops with hyperspectral data. In *Hyperspectral Remote Sensing of Vegetation*, edited by P. S. Thenkabali and J. G. Lyon, 187–206. Boca Raton, Fla.: CRC Press.

# SUSTAINING MEMBERS

## **ACI USA Inc.**

Weston, Florida  
acicorporation.com  
*Member Since: 1/2018*

## **Aerial Services, Inc.**

Cedar Falls, Iowa  
www.AerialServicesInc.com  
*Member Since: 5/2001*

## **Ayres Associates, Inc.**

Madison, Wisconsin  
www.AyresAssociates.com  
*Member Since: 1/1953*

## **Bohannon Huston, Inc.**

Albuquerque, New Mexico  
www.bhinc.com  
*Member Since: 11/1992*

## **Cardinal Systems, LLC**

Flagler Beach, Florida  
www.cardinalsystems.net  
*Member Since: 1/2001*

## **Dewberry**

Fairfax, Virginia  
www.dewberry.com  
*Member Since: 1/1985*

## **Environmental Research Incorporated**

Linden, Virginia  
www.eri.us.com  
*Member Since: 8/2008*

## **Extensis**

Seattle, Washington  
www.extensis.com  
*Member Since: 1/1997*

## **GeoBC**

Victoria, Canada  
www.geobc.gov.bc.ca  
*Member Since: 12/2008*

## **GeoCue Group**

Madison, Alabama  
info@geocue.com  
*Member Since: 10/2003*

## **GeoJano**

Pleasanton, California  
https://geojango.com/  
*Member Since: 05/2019*

## **Geomni, Inc.**

Lehi, Utah  
Geomni.net/psm  
*Member Since: 03/2018*

## **Global Science & Technology, Inc.**

Greenbelt, Maryland  
www.gst.com  
*Member Since: 10/2010*

## **GPI Geospatial Inc.**

formerly **Aerial Cartographics of America, Inc. (ACA)**  
Orlando, Florida  
www.aca-net.com  
*Member Since: 10/1994*

## **Keystone Aerial Surveys, Inc.**

Philadelphia, Pennsylvania  
www.keystoneaerialsurveys.com  
*Member Since: 1/1985*

## **Kucera International**

Willoughby, Ohio  
www.kucerainternational.com  
*Member Since: 1/1992*

## **L3Harris Corporation**

Broomfield, Colorado  
www.harris.com  
*Member Since: 6/2008*

## **Martinez Geospatial, Inc. (MTZ)**

Eagan, Minnesota  
www.mtzgeo.com  
*Member Since: 1/1979*

## **Merrick & Company**

Greenwood Village, Colorado  
www.merrick.com/gis  
*Member Since: 4/1995*

## **PixElement**

Columbus, Ohio  
www.pixelement.com  
*Member Since: 1/2017*

## **Quantum Spatial, Inc.**

Sheboygan Falls, Wisconsin  
www.quantumspatial.com  
*Member Since 1/1974*

## **Robinson Aerial Survey, Inc. (RAS)**

Hackettstown, New Jersey  
www.robinsonaerial.com  
*Member Since: 1/1954*

## **Routescene, Inc.**

Durango, Colorado  
www.routescene.com/  
*Member Since: 12/2007*

## **Sanborn Map Company**

Colorado Springs, Colorado  
www.sanborn.com  
*Member Since: 10/1984*

## **Teledyne Optech**

Toronto, Canada  
www.teledyneoptech.com  
*Member Since: 1/1999*

## **Towill, Inc.**

San Francisco, California  
www.towill.com  
*Member Since: 1/1952*

## **Trimble**

Munich, Germany  
www.trimble.com/geospatial  
*Member Since: 4/1994*

## **U.S. Geological Survey**

Reston, Virginia  
www.usgs.gov  
*Member Since: 4/2002*

## **Woolpert LLP**

Dayton, Ohio  
www.woolpert.com  
*Member Since: 1/1985*

# Quintuple Local Coordinate Images for Local Shape Description

Wuyong Tao, Xianghong Hua, Ruisheng Wang, and Dong Xu

## Abstract

Owing to poor descriptiveness, weak robustness, and high computation complexity of local shape descriptors (LSDs), point-cloud registration in the case of partial overlap and object recognition in a cluttered environment are still challenging tasks. For this purpose, an LSD is developed in this article by proposing a new local reference frame (LRF) method and designing a novel feature representation. In the LRF method, two weighting methods are applied to obtain robustness to noise, point-density variation, and incomplete shape. Additionally, a vector representation is calculated to disambiguate the sign of the  $x$ -axis. The feature representation encodes the local information by generating the local coordinate images from five views. Thus, more geometric and spatial information is included in the descriptor. Finally, the performance of the LRF method and the LSD is evaluated on several popular data sets. The experimental results demonstrate well that the LRF is robust to noise, point-density variation, and incomplete shape, and the LSD holds strong robustness, superior descriptiveness, and high computational efficiency.

## Introduction

In computer vision and computer graphics, local shape description has been extensively researched and proven to be very successful. A wide variety of applications are implemented by means of local shape description, such as registration of point clouds (Guo *et al.* 2014; Dong *et al.* 2018; Yang, Xiao and Cao 2019), object recognition (Johnson and Hebert 1999; Zhong 2009; Aldoma *et al.* 2012), and simultaneous localization and mapping (Tong and Barfoot 2013; Zhang and Singh 2014). With the advent of laser scanning devices, 3D point-cloud data became increasing popular. The attention of scholars has been moved from 2D descriptors to 3D ones (Knopp *et al.* 2010; Darom and Keller 2012). In comparison with 2D descriptors, 3D descriptors are not influenced by illumination condition or shadow, by which more accurate rigid transformation (i.e., translation and rotation) could be obtained. Nevertheless, 3D descriptors still need to be further studied for point-cloud registration in the case of partial overlap and object recognition in cases with occlusion and clutter.

---

Wuyong Tao is with the School of Geodesy and Geomatics, Wuhan University, Wuhan 430079, China; and the Department of Geomatics Engineering, University of Calgary, Calgary T2N 1N4, Canada.

Xianghong Hua is with the School of Geodesy and Geomatics, Wuhan University, Wuhan 430079, China (xhhua@sgg.whu.edu.cn).

Ruisheng Wang is with the School of Geographical Sciences, Guangzhou University, Guangzhou 510006, China; and the Department of Geomatics Engineering, University of Calgary, Calgary T2N 1N4, Canada (ruiswang@ucalgary.ca).

Dong Xu is with the State Key Laboratory of Information Engineering in Surveying, Mapping and Remote Sensing, Wuhan University, Wuhan 430079, China.

The existing 3D descriptors can be broadly classified into two categories: global and local. A limitation of global shape descriptors is that the object needs to be separated from a cluttered scene beforehand, because they encode the geometric information of the entire object. Therefore, they cannot be used for incomplete objects, due to their sensitivity to occlusion and clutter. By contrast, local shape descriptors (LSDs) encode the geometric information of the local neighborhood around the key point into a feature vector representation, so they are robust to clutter and occlusion. Consequently, LSDs are suitable for point-cloud registration with partial overlap and object recognition in chaotic scenes.

LSDs are computed on the key points extracted from point clouds. Through comparison of the similarity of the LSDs, the key points in the model point cloud are then paired with those in the scene point cloud. If the descriptors of two key points from different point clouds are similar (the same in principle), the correspondence between the two key points is established. Therefore, LSDs should be invariant to rigid transformation. However, owing to the effect of different kinds of nuisances (including noise, outliers, varying point density, occlusion, clutter, and missing regions), the calculated LSDs are hard-pressed to keep the invariance. This requires that the LSDs have the ability to resist these nuisances (i.e., robustness). Another important characteristic is descriptiveness. A good LSD should describe as much information of the local surface as possible to obtain high descriptiveness. This is helpful to improve descriptor matching performance, which directly influences the accuracy of estimated transformation parameters and the computational time in verification and refinement phases. A large number of LSDs have been devised for different purposes. Examples contain snapshots (Malassiotis and Strintzis 2007), spin images (SI; Johnson and Hebert 1998), fast point feature histograms (FPFH; Rusu, Blodow and Beetz 2009), rotational projection statistics (RoPS; Guo *et al.* 2013), triple orthogonal local depth images (TOLDI; Yang *et al.* 2017c), and signature of histograms of orientations (SHOT; Tombari, Salti and Di Stefano 2010b). These descriptors can be generally divided into two classifications, in light of whether a local reference frame (LRF) method is employed or not. The descriptors without LRF—such as SI, FPFH, and local surface patch (Chen and Bhanu 2007)—use only the local geometric information to form feature vectors. This kind of descriptor takes geometric information into account but discards spatial information; hence, they have limited descriptiveness (Tombari *et al.* 2010a). In contrast, the descriptors with LRF (e.g., RoPS, SHOT, and Tri-Spin-Image; Guo *et al.* 2015) have higher descriptiveness because both spatial and geometric information are encoded into feature vectors with respect to the LRF. A comparative analysis of LSDs can be found in Guo *et al.* (2016).

---

Photogrammetric Engineering & Remote Sensing  
Vol. 86, No. 2, February 2020, pp. 121–132.  
0099-1112/20/121–132

© 2020 American Society for Photogrammetry  
and Remote Sensing  
doi: 10.14358/PERS.86.2.121

For the descriptors with LRF, the LRF and feature representation are two important components. An LRF is a 3D coordinate system constructed by using neighboring points around a key point, which is independent of the scanning coordinate system. Therefore, the descriptors with LRF are also independent of the scanning coordinate system. This makes them invariant to rigid transformation. In addition, the LRF provides a way to divide the local neighborhood into several parts, leading to encoding of the spatial information. A study of the effect of spatial information was performed by Yang, Zhang, and Cao (2017b). Several geometric features have been used to design the feature representation—e.g., point density (Guo *et al.* 2013), local depth (Yang *et al.* 2017c), and their combination (Yang *et al.* 2017a). A good feature representation should provide an effective and efficient manner to characterize the local information. However, most of the existing LSDs still suffer from poor descriptiveness due to either single-view information encoding or loss of information.

In this article, a highly descriptive, robust, and efficient LSD is formulated. At first, a novel LRF method is proposed, in which the Gaussian function (Levin 2004) is introduced to determine the weights for the points in the radius neighborhood. The Gaussian function can be adjusted to obtain robustness by varying the Gaussian parameter. When the Gaussian parameter is set at a proper value, a balanced robustness against noise and shape incompleteness (i.e., missing regions, clutter, and occlusion) can be obtained. The weighting method of Dong *et al.* (2017) is also applied to obtain robustness to point-density variation. Additionally, a vector representation, which is the weighted sum of the vectors from the key point to the neighbors, is calculated to disambiguate the sign of the  $x$ -axis. The projection distances from the neighbors to the tangent plane are used to determine the weights for the vectors. The weighting strategy helps improve the robustness to occlusion, clutter, and missing regions, because the projection distances are distinctive cues (Petrelli and Di Stefano 2012) and thus provide robustness to shape incompleteness (Yang *et al.* 2018). Thus, our LRF method has the advantage of robustness to noise and point-density variation, and absorbs the advantage of robustness to incomplete shape. For the feature representation, after the points in the local surface are transformed with respect to the LRF, the coordinates of the points in the local coordinate system (i.e., the LRF) can be achieved. We call these coordinates local coordinates, which are regarded as the geometric feature in our feature representation. The reasons for using the local coordinates are at least threefold. First, the local coordinates are invariant to rigid transformation, which ensures that the descriptor is invariant to rigid motion. Second, the local coordinates are computationally cheap, because after transformation they can be directly obtained without any computation. Third, the local coordinates are projected on planes to form local coordinate images (LCIs). A single point is enough to calculate the value of a bin in the LCI, so the effect of point-density variation is pretty weak. The maximum or minimum local coordinate value of the points falling in a bin is treated as the value of the bin, so noise is of little effect as well.

In the TOLDI descriptor, the LDIs are calculated from three views. This will result in loss of geometric information (see The Feature Representation). Therefore, our descriptor calculates the LCIs from five views, and because of this, we refer to quintuple local coordinate images (QLCIs). In addition, many of the existing descriptors are designed for triangle mesh data, but triangulation is often erroneous for data in practice projects, which are usually affected by noise and surface discontinuity (Dong *et al.* 2017). In contrast, our method can be directly used on point-cloud data. The main contributions of our research are summarized as follows:

- A novel LRF method is proposed. Two weighting methods are applied to obtain robustness to noise and point-density variation. A vector representation is used to reorient the direction of the  $x$ -axis for enhancing robustness to shape incompleteness.
- Based on the proposed LRF, a new LSD (i.e., QLCI) is designed which calculates the LCIs from five views. Thus, our descriptor is more distinctive because more local geometric and spatial information is encoded. Our descriptor also exhibits high robustness and computational efficiency.

The remainder of this article is organized as follows. In the next section, the related work on LRF and LSDs is briefly reviewed. Then we present the proposed QLCI descriptor in detail. Next, comprehensive experiments are undertaken to demonstrate the performance of our LRF method and descriptor. Finally, the conclusion and outlook are presented.

## Related Work

A large amount of work on local shape description has been done in the literature. We first review some LRF methods, then present a brief overview of the existing LSDs.

### Methods of Building an LRF

A thorough assessment of several state-of-the-art LRF methods has been performed by Yang *et al.* (2018). They classify the LRF methods into two types: those based on covariance analysis (CA) and those based on geometric attribution (GA). All of the points in the local neighborhood are applied to calculate the covariance matrix in the CA-based methods. After eigen-value decomposition on the covariance matrix, three eigen vectors can be obtained, which are treated as the three axes of the LRF. For the GA-based methods, the  $z$ -axis is first computed by a subset of the neighboring points, and then the  $x$ -axis is determined according to the geometric attribution. Finally, the  $y$ -axis is computed by the cross product of the  $x$ - and  $z$ -axes. In general, the CA-based methods have better robustness to noise, while the GA-based methods have better robustness to occlusion, clutter, and missing regions; and the GA-based methods are computationally more expensive than the CA-based methods in general.

We discuss several CA-based methods first. In work by Mian, Bennamoun, and Owens (2010), after the eigen vectors were achieved only the sign of the  $z$ -axis was disambiguated. Later, Tombari *et al.* (2010b) removed all the sign ambiguities of the LRF axes for the first time, a weighting strategy was developed to enhance repeatability under clutter, and the key point was used to replace the barycenter of the neighborhood, to reduce the computational complexity. The method is rather robust to noise, but sensitive to point-density variation. Guo *et al.* (2013) formulated a method for triangle mesh data, in which the covariance matrix was calculated for each triangle. Then all the covariance matrices were aggregated into a whole one. Two weighting methods were applied, one for alleviating the effect of point-density variation and the other for improving the robustness to occlusion and clutter. The sign ambiguities of all LRF axes were also removed, but the method is time consuming. Dong *et al.* (2017) applied two weighting methods to boost the robustness of the LRF to shape incompleteness and point-density variation. The difference is that this LRF method is designed for point-cloud data. However, the authors did not verify the performance of their method by experiment.

For the GA-based methods, Petrelli and Di Stefano (2011) used only the points with distances to the key point of smaller than  $5mr$  ( $mr$  denotes the mesh resolution) to calculate the  $z$ -axis, so as to achieve repeatability in the case with incomplete shape. The sign ambiguity of the  $z$ -axis was removed by making its direction consistent with the average normal over

the points in the neighborhood. Then the points in the marginal area—i.e., the points whose distances to the key point are larger than  $0.85 \times r$  ( $r$  is the neighborhood radius)—were used to determine the  $x$ -axis according to the normal deviation angle. The point with the largest normal deviation angle was selected. In addition, the method includes a step for detecting missing regions. Subsequently, Petrelli and Di Stefano (2012) found that the signed distance was steadier compared to the normal deviation. Therefore, the point with the largest signed distance was chosen from the points in the border region to calculate the  $x$ -axis. A drawback is that the method is sensitive to noise and outliers. Yang *et al.* (2017c) used a subset of neighboring points (i.e., the points whose distances to the key point are smaller than  $1/3 \times r$ ) to calculate the  $z$ -axis. Then the projection vectors of these neighbors were obtained by projecting them on the tangent plane. The weighted sum of these projection vectors was defined as the  $x$ -axis. Two weighting strategies were developed to determine the weights for the projection vectors. One is designed for increasing robustness to clutter, occlusion, and incomplete border regions by using the distances from the key point to neighbors; the other is designed using the projection distances. The sum operation of the projection vectors was proven to be useful to improve robustness to noise. The drawback of the method is that it is easily influenced by key-point localization error. Akizuki and Hashimoto (2015) developed two LRF methods, called dominant projected normal LRF. One was designed for triangle mesh data, and the other was designed for point-cloud data, because the LRF without triangle meshes is preferable in practice. In the two methods, the  $z$ -axis was calculated by using the points with a distance of  $10mr$  to the key point. In order to generate the  $x$ -axis, a polar histogram with 36 bins was constructed. The voted value for each bin was calculated by multiplication of three weighting factors. The dominant orientation of the polar histogram was defined as the  $x$ -axis. The difference between the two methods is that the weighting factors are calculated according to different methods. The two LRF methods obtain good performance under point-density variation, clutter, and occlusion, but they are computationally expensive, especially the method for triangle mesh data.

### LSDs

One of the most frequently cited descriptors is SI (Johnson and Hebert 1998). It first defined the oriented point with 3D coordinates and the surface normal. Each neighboring point of the key point was characterized by two geometric features. Then the number of neighbors was accumulated into a 2D accumulator indexed by the two geometric features, generating a gray image. Chen and Bhanu (2007) proposed the local surface patch descriptor. A local surface patch around the key point was represented by centroid, surface type, and 2D histogram, with the 2D histogram generated by encoding the shape indices and normal deviations of the neighbors. Flint, Dick, and van den Hengel (2008) proposed the ThrIFT descriptor, which is an extension of the 2D scale-invariant feature transform descriptor. It was generated by calculating the weighted feature vector that is formed according to the deviation between normals. Rusu *et al.* (2008) formulated the point feature histograms (PFH) descriptor by encoding the difference between the normals of any two points in the local neighborhood. A limitation is that the PFH has high computational complexity. Therefore, the FPFH descriptor was later constructed by using a simplified PFH (Rusu *et al.* 2009). Yang, Cao, and Zhang (2016) integrated multiple geometric features into a feature vector, forming the local feature statistics histograms descriptor, which is fast but suffers from low descriptiveness. All of these descriptors are without LRF. Because spatial information is discarded, they have limited descriptiveness.

As for LRF-based descriptors, Sun and Abidi (2001) used the normal of the key point and a random neighboring point to construct the LRF, proposing a descriptor called the point's fingerprint. In this method, geodesic circles were projected on the tangent plane to form a set of 2D contours. One major limitation is that the LRF of this descriptor is nonunique. Frome *et al.* (2004) formulated the 3D shape context (3DSC) descriptor by extending the 2D counterpart. They partitioned the local neighborhood into several bins according to the azimuth, elevation, and radius. The value of each bin is the weighted number of points in it. The drawback of 3DSC is that it lacks the definition of a repeatable LRF on the key point. Therefore, Tombari *et al.* (2010a) employed the LRF method proposed by Tombari *et al.* (2010b) to produce the repeatable LRF for improving the 3DSC descriptor, thus introducing the unique shape context descriptor. In order to give the 3DSC descriptor invariance to rotations, Sukno, Waddington, and Whelan (2013) developed the asymmetry patterns shape context descriptor. Malassiotis and Stryntzis (2007) assumed that a virtual camera was installed in front of the local surface to take "snapshots," and therefore named the descriptor snapshots. Because only the information from a single view is encoded, the descriptor still exhibits low descriptiveness. Zhong (2009) developed the intrinsic shape signature descriptor. The base octahedron was used as the elemental unit of the spherical grids. Thus, the angular space was split into some number of bins. The weights of all the points falling in a bin were summed to form the shape feature vector. Tombari *et al.* (2010b) presented the SHOT descriptor. The local neighborhood was divided into 3D volumes; then, in the light of the deviation angles between the normal vectors, a local histogram was produced for each volume by counting the number of points. The SHOT descriptor is highly descriptive, but it is susceptible to point-density variation. Guo *et al.* (2013) designed the RoPS descriptor, in which the local point cloud was first transformed with respect to the LRF. Then the transformed point cloud was rotated around the three axes of the LRF to get a certain number of rotated point clouds. Each rotated point cloud was projected on the three planes defined by the LRF to achieve 2D distribution matrices, which were then represented by five statistics (four central moments and one Shannon entropy). Finally, all the statistics of the rotated point clouds were grouped into a feature vector. A limitation of the RoPS descriptor is its susceptibility to the nonuniformity of points. Dong *et al.* (2017) proposed the binary shape context descriptor by encoding the weighted projection density and distance. The descriptor was generated by the difference test. The experiment showed that the descriptor has high descriptiveness and requires a smaller memory footprint. Guo *et al.* (2015) considered that encoding the local information from a single view will result in loss of information in the SI descriptor. The Tri-Spin-Image descriptor was developed by calculating the spin images from three views. Similarly, Yang *et al.* (2017c) considered that a single view is not enough to make the utmost of the shape information of the local surface. The TOLDI descriptor was proposed by calculating the LDIs from three views. This descriptor exhibits very good performance in terms of descriptiveness, robustness, and computational efficiency.

### QLCI Descriptor

In this section, we present in detail the QLCI descriptor. The proposed LRF method is first described, and then the feature representation is given. Eventually, the related parameters are quantitatively analyzed.

#### The Proposed LRF Method

The repeatability of the LRF directly influences the descriptor's matching performance, so a unique, robust, and repeatable

LRF plays an important role in the local shape description. Our method belongs to CA-based methods. The points in the local neighborhood are used to construct the covariance matrix. Then the eigen-value decomposition is implemented on the covariance matrix to achieve the three axes of the LRF. Our method has two differences from previous methods. First, the Gaussian function is introduced to determine the weights for the neighbors. Second, a vector representation is calculated to disambiguate the sign of the x-axis.

A local point cloud  $Q = \{\mathbf{q}_1 \ \mathbf{q}_2 \ \dots \ \mathbf{q}_k\}$  is extracted by a sphere with radius  $r$  centered at a key point  $\mathbf{p}$ . The local point cloud is used to construct the covariance matrix  $\mathbf{M}$ , and the key point is applied to replace the centroid, for reducing computational time. The covariance matrix is calculated as

$$\mathbf{M} = \frac{1}{\sum \omega_{i1}\omega_{i2}} \sum \omega_{i1}\omega_{i2} (\mathbf{q}_i - \mathbf{p})(\mathbf{q}_i - \mathbf{p})^T. \quad (1)$$

The weights  $\omega_{i1}$  are determined by the Gaussian function (Levin 2004), computed as

$$\omega_{i1} = e^{-\left(\frac{\|\mathbf{q}_i - \mathbf{p}\|}{\kappa \cdot r}\right)^2}, \quad (2)$$

where  $\kappa$  is the Gaussian parameter and  $\|\cdot\|$  denotes the Euclidean distance. The Gaussian parameter controls the contribution of the neighbors to the covariance matrix. Both too much and too little contribution would reduce the robustness of the LRF to noise and thus degrade the descriptor's matching performance (as will be shown under Analysis of QLCI Parameters). Therefore, the Gaussian parameter should be set at a proper value to get the best robustness to noise. Furthermore, we can observe that the weights decrease as the distance increases. Hence, the weighting method can be used to enhance the robustness in the presence of clutter, occlusion, and incomplete border regions.

For the weights  $\omega_{i2}$ , the method of Dong *et al.* (2017) is applied:

$$\omega_{i2} = \frac{1}{\#\{\mathbf{t}_n : \|\mathbf{t}_n - \mathbf{q}_i\| < r_d\}}, \quad (3)$$

where  $\mathbf{t}_n$  are the neighboring points of  $\mathbf{q}_i$ ,  $\#$  denotes the number of points, and  $r_d$  is the radius for estimating point density. We set  $r_d = 0.4r$  in this article. The aim of this weighting strategy is to increase robustness to point-density variation, because points with low density contribute more to the covariance matrix.

By implementing the eigen-value decomposition on  $\mathbf{M}$ , we obtain three eigen values ( $\lambda_1 > \lambda_2 > \lambda_3$ ) and the corresponding three eigen vectors ( $\mathbf{v}_1, \mathbf{v}_2, \mathbf{v}_3$ ). The latter are regarded as the

unit vectors of the LRF. In order to disambiguate the sign of the axes, the z-axis is defined as

$$\mathbf{z} = \begin{cases} \mathbf{v}_3 & \text{if } \mathbf{v}_3 \cdot \sum_{i=1}^k \mathbf{q}_i \mathbf{p} \geq 0, \\ -\mathbf{v}_3 & \text{otherwise,} \end{cases} \quad (4)$$

where  $k$  is the number of the points in the local point cloud and  $\mathbf{q}_i \mathbf{p}$  represents the vector from  $\mathbf{q}_i$  to  $\mathbf{p}$ .

The x-axis is defined as

$$\mathbf{x} = \begin{cases} \mathbf{v}_1 & \text{if } \mathbf{v}_1 \cdot \mathbf{v}_{\text{res}} \geq 0, \\ -\mathbf{v}_1 & \text{otherwise,} \end{cases} \quad (5)$$

where  $\mathbf{v}_{\text{res}}$  is the vector representation

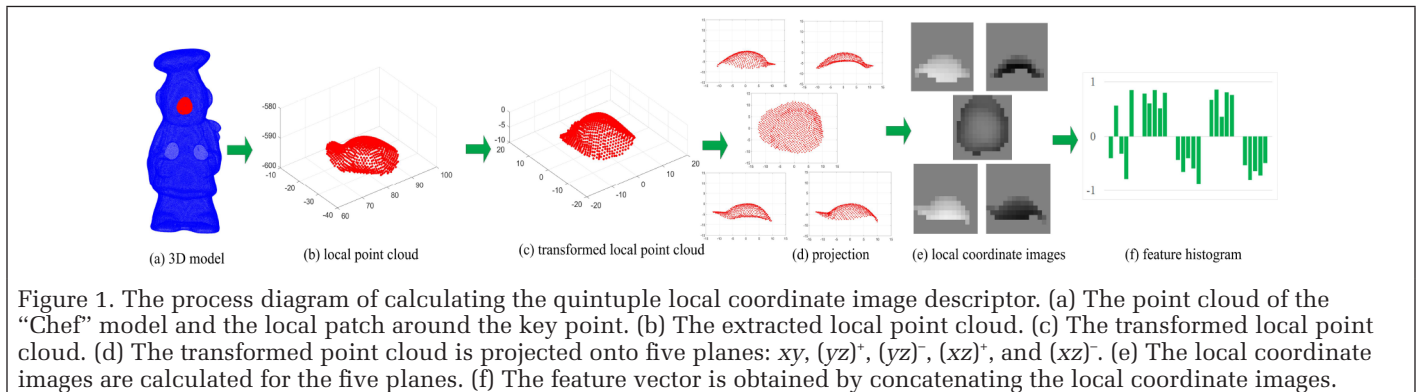
$$\mathbf{v}_{\text{res}} = \sum_{i=1}^k \omega_{i1}^x \mathbf{p} \mathbf{q}_i, \quad (6)$$

with  $\omega_{i1}^x$  determined by the projection distance. That is,  $\omega_{i1}^x = (\mathbf{p} \mathbf{q}_i \cdot \mathbf{z})^2$ . Thus, the points with larger projection distances contribute more to the vector representation. Because the projection distances are distinctive cues (Petrelli and Di Stefano 2012), they are helpful in enhancing the robustness of the LRF to shape incompleteness, as shown by Yang *et al.* (2018). Eventually the y-axis is obtained by the cross product of the x- and z-axes. We also used the projection vector of  $\mathbf{p} \mathbf{q}_i$  to calculate  $\mathbf{v}_{\text{res}}$ , whereas the repeatability of the LRF is the same. Therefore, the vector  $\mathbf{p} \mathbf{q}_i$  is applied in order not to increase computational time. In addition, we tested using the vector from the key point to the point with the largest signed distance rather than the sum of vectors as the representation vector. The results showed that the LRF is sensitive to noise.

### The Feature Representation

With the LRF, we can start to describe the local shape by encoding the neighborhood information (spatial and geometric information). To achieve invariance to rigid transformation, the local point cloud is first transformed with respect to the LRF. Then the feature vector is calculated to encode the local information for the transformed point cloud  $Q' = \{\mathbf{q}'_1 \ \mathbf{q}'_2 \ \dots \ \mathbf{q}'_k\}$ . The process diagram of calculating the QLCI descriptor is shown in Figure 1.

In our method, the local coordinates ( $x_{q'_i}, y_{q'_i}, z_{q'_i}$ ) are used to calculate the feature vector. The most similar descriptor to ours is TOLDI, in which the local depths ( $r-x_{q'_i}, r-y_{q'_i}, r-z_{q'_i}$ ) are used. The value of the neighborhood radius  $r$  is fixed, so the local coordinates are equivalent to the local depths. Therefore, the local coordinates—the same as the local depths—preserve most of the information of the local shape. Furthermore, local coordinates are more computationally efficient than local depths.



In addition, the TOLDI descriptor encodes the geometric information from three views. To speak precisely, the three views are the positive directions of the  $x$ -,  $y$ -, and  $z$ -axes, respectively. This will result in loss of information. We take the positive direction of the  $x$ -axis as an example to illustrate this, as shown in Figure 2. When the LDI is generated from the positive direction of the  $x$ -axis (i.e., the point cloud is projected onto the  $yz$  plane), for the points falling in the same bin the points on the right side always have a smaller local depth value. Therefore, only the right side of the local shape is encoded, because the smallest local depth value is treated as the pixel value in the TOLDI descriptor. This means that the left geometric information is lost. We can also consider this as self-occlusion (the right local surface occludes the left local surface). Similarly, when the LDI is generated from the positive direction of the  $y$ -axis, the corresponding left geometric information is also lost. Regarding the  $z$ -axis, because there is no (or sometimes slight) self-occlusion, the projected point clouds from the positive and negative directions have the same distribution. Hence, encoding the local surface from the positive and negative directions of the  $z$ -axis will generate redundant information. This will not enhance the descriptor's descriptiveness but will increase the dimensionality. Consequently, the positive direction of the  $z$ -axis is enough to encode the local shape from this view without loss of information. Motivated by these reasons, we generate the LCIs from five views—i.e., the positive and negative direction of the  $x$ -axis, the positive and negative direction of the  $y$ -axis, and the positive direction of the  $z$ -axis. Accordingly, the local point cloud is projected onto the  $(yz)^+$ ,  $(yz)^-$ ,  $(xz)^+$ ,  $(xz)^-$ , and  $xy$  planes. For the  $(yz)^+$  plane, only the points with  $x$ -coordinate values larger than 0 are projected onto the plane, and for the  $(yz)^-$  plane, only those with  $x$ -coordinate values smaller than 0. The same operation is used for the  $(xz)^+$  and  $(xz)^-$  planes, with respect to  $y$ -coordinate values. For the  $xy$  plane, all the points are projected on the plane at once. Thus, more geometric and spatial information is included in the descriptor. Moreover, applying the multiview mechanism could provide complementary and relatively nonredundant information, as suggested by Guo *et al.* (2015).

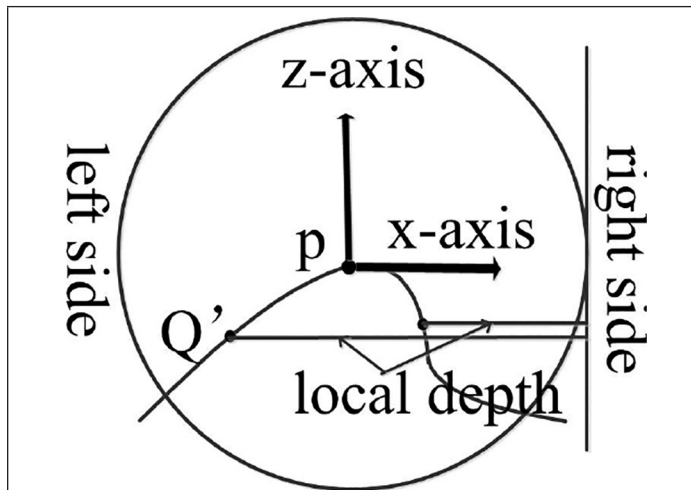


Figure 2. The transformed local point cloud  $Q'$ . The point  $p$  is the key point and the arrows are the  $x$ - and  $z$ -axes.

Then, on each plane, an LCI is generated using 2D array accumulator. The local coordinates of the neighbors are used to calculate the features. That is,

$$\begin{cases} f_i^{xy} = z_{q'_i} \\ f_i^{(yz)^+} = x_{q'_i} \\ f_i^{(yz)^-} = x_{q'_i} \\ f_i^{(xz)^+} = y_{q'_i} \\ f_i^{(xz)^-} = y_{q'_i} \end{cases} \quad (7)$$

The values of these features are in the range of  $[-r \ r]$ . Dividing by  $r$  normalizes these features into the range of  $[-1 \ 1]$ . For the LCIs on the  $(yz)^+$ ,  $(xz)^+$ , and  $xy$  planes, the largest local coordinate value of all points in a pixel is treated as the pixel value. However, for those on the  $(yz)^-$  and  $(xz)^-$  planes, the smallest local coordinate value of all points in a pixel is treated as the pixel value. Additionally, if a pixel contains no point, its value is 0. The side length of an image is  $2r$  and the number of its pixels is  $w \times w$ . The pixel values of each image are arranged into a subvector and then all the subvectors are concatenated into a 1D histogram, forming the QLCI descriptor with dimension of  $5 \times w \times w$ .

#### Analysis of QLCI Parameters

The larger the neighborhood radius  $r$ , the more information the local surface contains; hence, the descriptor is more descriptive. However, a large neighborhood radius will also increase the computational time. We set the neighborhood radius as  $15pr$  ( $pr$  represents the point-cloud resolution—i.e., the mean value of shortest distances among the neighboring points) to achieve a trade-off between the descriptor's descriptiveness and computational efficiency. The reason for using  $pr$  as the unit is that our method is designed for point-cloud data. The balanced robustness to noise and incomplete shape is achieved by varying the Gaussian parameter  $\kappa$ . The value of  $\kappa$  controls the contributions of the neighbors to the covariance matrix. A large  $\kappa$  makes the distant points—which have a higher possibility of being affected by clutter, occlusion, and missing border regions—contribute more to the covariance matrix; this decreases the robustness of the LRF to these nuisances. In contrast, a small  $\kappa$  will reduce the contributions of the distant points to the covariance matrix, leading to the LRF being sensitive to noise. The benefit of varying the Gaussian parameter is that increasing the value of  $\kappa$  will not introduce new clutter, occlusion, and missing border regions and increase the computational time. However, increasing  $r$  will cause these problems. The value of  $\kappa$  can be adjusted to get the best descriptor matching performance. Another important parameter is the number of partition bins  $w$ . A large  $w$  will make the descriptor more distinctive, and therefore increase the descriptiveness, but it will also make the descriptor susceptible to noise and point-density variation. As a consequence, the value of  $w$  should be set to achieve the balance between the descriptor's descriptiveness and robustness. In addition, in our method  $w$  is set to an odd number to increase robustness to perturbations of the LRF, as suggested by Dong *et al.* (2017).

In order to determine the proper values of  $\kappa$  and  $w$ , we check the performance of the QLCI descriptor on the Bologna Retrieval (BR) data set (see details under Data Sets) under different values of  $\kappa$  and  $w$ . The sampling rate is set as  $7/10$  to down-sample the scene point clouds. Then the Gaussian noise with standard deviation of  $0.3pr$  is injected to them as well. The recall-versus-1-precision (RP) curves (see details under RP Curve) are plotted to analyze the matching performance of the proposed descriptor under various parameters.

With five different values of  $\kappa$  and six of  $w$ , 30 experiments are performed. The main and useful results are shown in

Figure 3. When the number of partition bins is 19 (Figure 3a), the value of  $\kappa$  is increased from 0.4 to 0.8. We observe that the performance becomes better and better as  $\kappa$  increases from 0.4 to 0.6, and then it declines. Therefore, when the value of  $\kappa$  is 0.6, the performance is the best. This indicates that the contributions of the distant points should be controlled properly. Both contributing too much and too little would degrade the robustness to noise. Considering that the performance improvement is slight when  $\kappa$  increases from 0.5 to 0.6, we choose the value of the Gaussian parameter as  $\kappa = 0.5$  so as to decrease the effect of shape incompleteness. Thus, a balanced robustness to noise and incomplete shape can be obtained.

When the value of the Gaussian parameter is set to  $\kappa = 0.5$ , the value of  $w$  is increased from 5 to 29. As shown in Figure 3b, performance improves as  $w$  increases from 5 to 19 and then degrades as  $w$  continues to increase. The best performance is achieved when the value of  $w$  is 19, so we set the number of partition bins to  $w = 19$ .

## Experiments

Both the repeatability of the proposed LRF and the matching performance of the designed descriptor are verified by comparison with several previously proposed methods. MATLAB is used to implement the experiments. The experimental environment is a PC with an Intel Core i7-7500U 2.7-GHz CPU and 20 GB of RAM, without parallel computing or GPU implementation.

### Data Sets

The experiments involve testing on four public data sets: BR (Tombari 2013), UWAOR (Mian *et al.* 2006b), Kinect (Tombari 2010b), and Space Time (Tombari 2013). They were acquired by different devices, which results in different modalities. The BR data set contains six noise-free model point clouds from the Stanford 3D Scanning Repository,<sup>1</sup> which were acquired by a Cyberware 3030 MS scanner. These model point clouds are transformed to get six scene point clouds by setting a true transformation. Then Gaussian noise with standard deviations of 0.1pr, 0.2pr, 0.3pr, 0.4pr, and 0.5pr is successively added to the six scene point clouds to create noisy versions with different levels of noise, and the six scene point clouds are also down-sampled to 9/10, 7/10, and 5/10 of their original points to create simplified versions. The total final number of scene point clouds is 60. This data set is used to test the performance under noise and point-density variation.

1. <http://www.graphics.stanford.edu/data/3Dscanrep>.

The UWAOR data set<sup>2</sup> includes five model point clouds and 50 real scene point clouds. Each scene point cloud is generated by scanning four or five models randomly placed together using a Minolta Vivid 910 scanner. In this data set, the main nuisances are clutter and occlusion. The Kinect data set<sup>3</sup> was acquired by a Microsoft Kinect sensor and is composed of six model point clouds and 16 real scene point clouds. Besides the clutter and occlusion, this data set is also noisy and sparse. The Space Time data set<sup>3</sup> contains eight model point clouds and 15 real scene point clouds, acquired by the Space Time Stereo technique. The main nuisances in this data set are clutter, occlusion, noise, and outliers.

The four data sets face different challenges, making our experiments more comprehensive. They also involve different applications: the BR data set was created for shape retrieval, whereas the other three were created for object recognition. Some exemplar model and scene point clouds in these data sets are shown in Figure 4. In each panel, the model point cloud is on the left and the scene point cloud is on the right.

### Evaluation Criteria

#### Repeatability of the LRF

In theory, if two LRFs  $L(\mathbf{p}^m)$  and  $L(\mathbf{p}^s)$  are computed on two corresponding key points  $\mathbf{p}^m$  and  $\mathbf{p}^s$ , they should conform to the relationship  $L(\mathbf{p}^s) = \mathbf{R}_{\text{true}} L(\mathbf{p}^m)$ , where  $\mathbf{R}_{\text{true}}$  is the true rotation matrix. Therefore, the error between the two LRFs can be calculated (Mian *et al.* 2006a; Yang *et al.* 2018) as

$$\text{error}_{\text{LRF}} = a \cos \left( \frac{\text{trace} \left( L(\mathbf{p}^s) \tilde{L}(\mathbf{p}^m)^{-1} \right) - 1}{2} \right) \frac{180}{\pi}, \quad (8)$$

where  $\tilde{L}(\mathbf{p}^m) = \mathbf{R}_{\text{true}} L(\mathbf{p}^m)$ . A value of  $\text{error}_{\text{LRF}} = 0$  means there is no rotation error between  $L(\mathbf{p}^m)$  and  $L(\mathbf{p}^s)$ .

In a model-scene pair, after the errors of all pairs of corresponding LRFs are computed, the ratio of the corresponding LRF pairs whose errors are smaller than  $10^\circ$  is calculated to assess the repeatability of the LRF:

$$\text{repeatability} = \frac{n_{10}}{n_t}, \quad (9)$$

2. <http://staffhome.ecm.uwa.edu.au/~00053650/recognition.html>.

3. <http://www.vision.deis.unibo.it/research/80-shot>.

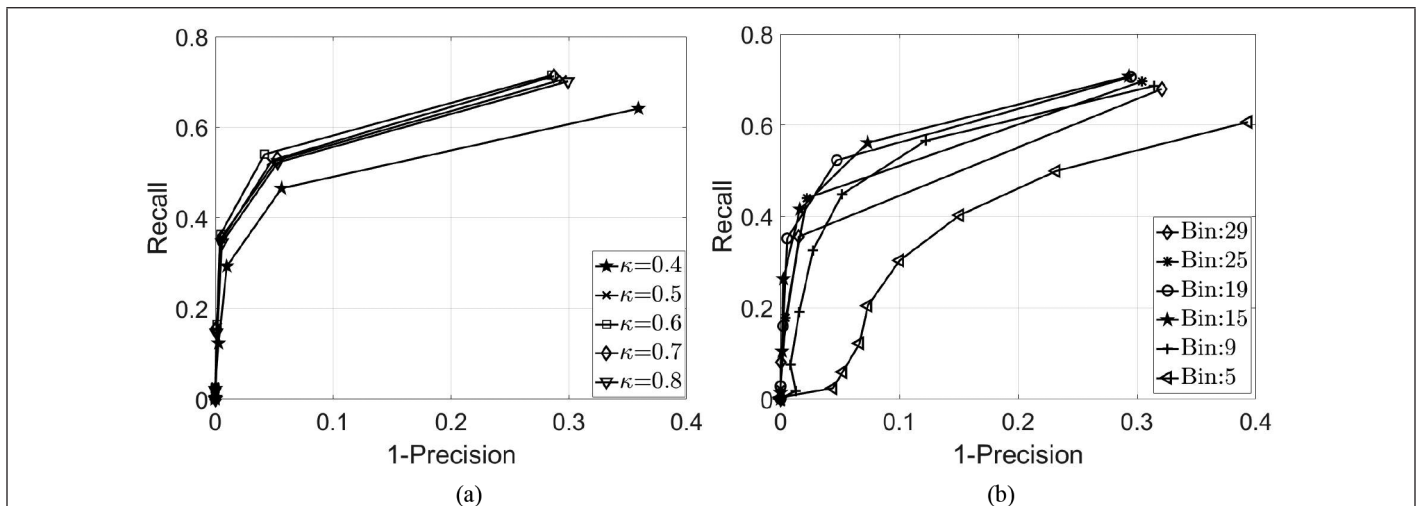


Figure 3. The effect of the quintuple local coordinate image parameters. (a) The recall-versus-1-precision curves under different Gaussian parameters  $\kappa$ . (b) The curves under different numbers of partition bins  $w$ .

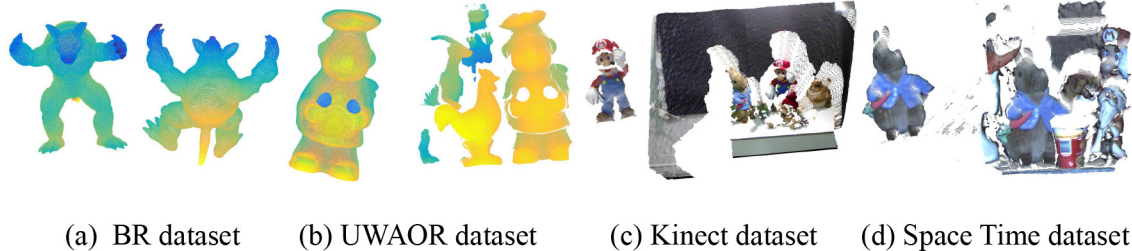


Figure 4. Some exemplar model and scene point clouds taken from the BR, UWAOR, Kinect, and Space Time data sets.

where  $n_{10}$  denotes the number of the corresponding LRF pairs with errors smaller than  $10^\circ$  and  $n_i$  denotes the total number of corresponding LRF pairs.

### RP Curve

The descriptor matching performance is usually evaluated by the RP curve. After the descriptors are calculated for the key points in both the model point cloud and the scene point cloud, each model descriptor  $f_i^M$  is compared with all the scene descriptors to find the two closest scene descriptors  $f_i^S$  and  $f_j^S$ , where  $f_i^S$  is more similar to  $f_i^M$  than  $f_j^S$ . In this step, the k-d tree can be applied to facilitate fast search of the closest descriptors in Euclidean space. If the ratio  $\|f_i^S - f_i^M\| / \|f_j^S - f_i^M\|$  between the two distances is smaller than a preset threshold, the model descriptor  $f_i^M$  is paired with the scene descriptor  $f_i^S$  and the key points associated with them are considered a match. A match is then considered correct if the distance between the two key points  $\tilde{p}^m$  and  $p^s$ , where  $\tilde{p}^m$  is the transformed model key point using the true transformation, is smaller than  $1/2 \times r$ ; otherwise it is considered incorrect. The RP curve is obtained by calculating the recall and 1-precision under different thresholds. The two indexes are defined as

$$\text{recall} = \frac{\text{number of correct matches}}{\text{total number of corresponding key-point pairs}} \quad (10)$$

and

$$1\text{-precision} = \frac{\text{number of incorrect matches}}{\text{total number of matches}}. \quad (11)$$

A good descriptor should have high recall and precision. This means the RP curve should fall in the top left of the plot.

### Implementation Details

In our experiments, we randomly extract 1000 key points from a model point cloud and transform them using the true transformation. The nearest points of the transformed key points are treated as the corresponding key points in the scene point cloud. The aim is to eliminate the effect of key-point localization errors, as inspired by Guo *et al.* (2013). For point clouds with incomplete shape (UWAOR, Kinect, and Space Time data sets), the key points in the overlap surface between the model and scene point clouds are extracted. The LRFs and descriptors are only calculated on the key points in the overlap surface. The true transformations of the BR data set are artificially set; those of the other data sets are provided by the publishers. For each data set, the RP curve is calculated for each model-scene pair. Then the average RP curve of all the model-scene pairs is exhibited in the experimental results.

### Performance Assessment of the LRF Proposal

In this section, the methods developed by Mian *et al.* (2010), Petrelli and Di Stefano (2012), and Yang *et al.* (2017c) are used to assess our method. The method of Mian *et al.* is frequently used to perform comparison. The method of Petrelli and Di Stefano has been demonstrated to be robust to shape

incompleteness. And the method of Yang *et al.* is a recently proposed one that achieves good performance in each aspect in their experiments. The experimental results are illustrated in Figure 5 and a quantitative evaluation presented. Repeatability performance is tested on the BR, UWAOR, Kinect, and Space Time data sets. The neighborhood radii of all the methods are set to 15pr for a fair comparison. The time-efficiency performance is tested on the ‘‘Armadillo’’ model of the BR data set. The time for computing the LRFs of 1000 key points is recorded under different neighborhood radii.

As can be seen from Figure 5a and b, in terms of robustness to noise and point-density variation, our method obtains the best performance. The method of Yang *et al.* (2017c) achieves the second best performance. The poorest method is the one proposed by Mian *et al.* (2010). Our method pertains to the CA-based methods. All the neighbors are used to construct the covariance matrix, and the two weighting methods are applied, so our method has relatively good robustness to noise and point-density variation. The method of Petrelli and Di Stefano (2012) is sensitive to noise, because the single point with the greatest signed distance is used to determine the x-axis. For the method of Yang *et al.*, the vector-sum operation indeed compensates the drawback that GA-based methods are sensitive to noise, so it has better performance than the method of Petrelli and Di Stefano. However, in comparison with CA-based methods it is still relatively sensitive to noise. The method of Mian *et al.* removes the sign ambiguity of only the z-axis. The sign of the x-axis is still ambiguous, so this method exhibits the poorest performance.

In order to illustrate that the projection distances are useful for improving robustness to incomplete shape, we do not use them to determine the weights (i.e., the weights are set at 1) when calculating the vector representation. This method is denoted as ‘‘proposed-b.’’ From Figure 5c, we can see that our method achieves better performance on the UWAOR data set compared to proposed-b. This indicates that our method has better robustness to clutter and occlusion. As expected, our method has robustness to noise and point-density variation and absorbs the advantage of robustness to incomplete shape.

The methods of Petrelli and Di Stefano (2012) and Yang *et al.* (2017c) achieve better performance on the UWAOR data set. Because only a subset of neighbors are applied to calculate the z-axis, these methods are more robust to clutter and occlusion. Furthermore, the UWAOR data set is less contaminated by noise. In general, GA-based methods are robust to incomplete shape but sensitive to noise and outliers. As shown in Figure 5c, on the Kinect and Space Time data sets they exhibit relatively poor performance due to the noise and outliers.

In terms of time efficiency, as shown in Figure 5d, our method obtains comparable performance with the method of Yang *et al.* (2017c). The method of Petrelli and Di Stefano (2012) requires the most computational time, due to the calculation of the average normal of the points in the neighborhood. The method of Mian *et al.* (2010) is the most computationally efficient, but it always gets the poorest repeatability

performance. Therefore, the proposed LRF method obtains relatively good time efficiency.

### Performance Assessment of the QLCI Descriptor

In this section our descriptor is compared with several existing descriptors: SI (Johnson and Hebert 1998), FPFH (Rusu *et al.* 2009), RoPS (Guo *et al.* 2013), and TOLDI (Yang *et al.* 2017c). The SI and FPFH descriptors are the most frequently cited ones and are usually used to perform comparison. The RoPS descriptor is a recently developed one, which achieves outstanding descriptor matching performance on numerous public data sets. The TOLDI descriptor is the most similar to ours, and is therefore used to compare with our descriptor. It is worth noting that for the RoPS and TOLDI descriptors, the proposed LRF method is applied to replace the original methods. Thus, we can remove the effect of the LRF and independently compare the performance of the feature representations. Furthermore, a good feature representation is easily combined with a good LRF method. Developers can simultaneously choose a good feature representation and a good LRF method, and thus derive a better LSD. The performance of these descriptors is evaluated by RP curve, and their parameter settings are listed in Table 1.

The RP curves of the five descriptors under different nuisances are shown in Figure 6. On the BR data set, the SI and FPFH descriptors always perform the poorest. The two descriptors are not based on the LRF, so spatial information

is discarded; therefore, they have low descriptiveness. In contrast, the RoPS, TOLDI, and QLCI descriptors use LRF, so all of them achieve good performance. In terms of robustness to noise (Figure 6a–c), the QLCI descriptor performs the best, followed by TOLDI and RoPS. With an increase in noise level, the margin between QLCI and TOLDI becomes larger and larger. In terms of robustness to point-density variation (Figure 6d–f), our descriptor also obtains the best performance. The difference between the QLCI and TOLDI descriptors gets larger at higher sampling rates (e.g., 5/10). Under the combination of noise and down-sampling (Figure 6g), our descriptor also achieves superior performance relative to the other descriptors. RoPS suffers from loss of information in the process of representing 3D information by feature vector (Yang *et al.* 2017c), and TOLDI encodes the local information from three views, which also results in loss of information. Therefore, these two descriptors exhibit inferior performance.

For robustness to clutter and occlusion (Figure 6h–j), our descriptor again achieves the best descriptor matching performance. On the UWAOR data set, QLCI outperforms the others by a large margin; FPFH performs second best. On the Kinect data set, QLCI and TOLDI obtain comparable performance, with RoPS exhibiting rather poor performance. This is because it is sensitive to the nonuniformity of points, and the Kinect-scanned point cloud is irregularly distributed. For the Space Time data set, QLCI and TOLDI are obviously better than the others. FPFH

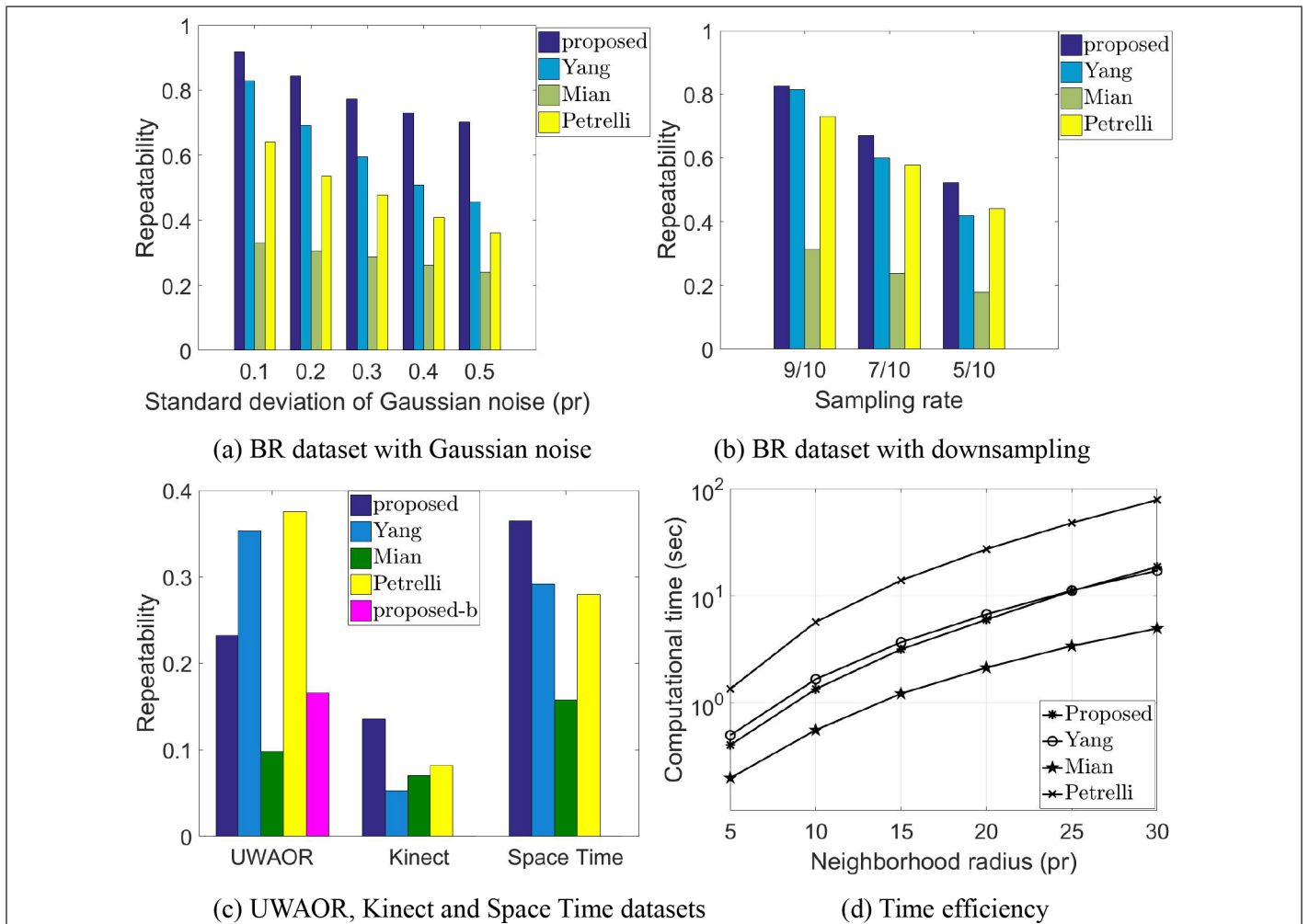


Figure 5. Performance of the four local reference frame (LRF) methods. (a) Repeatability performance under different levels of noise tested on the BR data set. (b) Repeatability performance under different sampling rates tested on the BR data set. (c) Repeatability performance tested on the UWAOR, Kinect, and Space Time data sets. (d) Time efficiency (the y-axis is logarithmic, for the best view).

Table 1. Parameter settings of the five local shape descriptors.

Name	Neighborhood radius (pr)	Parameters	Dimensionality
SI	15	Number of bins for radial distance: 15 Number of bins for signed distance: 15	$15 \times 15 = 225$
FPFH	15	Number of angular variation features: 3 Number of bins for each feature: 11	$3 \times 11 = 33$
RoPS	15	Number of rotation axes: 3 Number of projection planes: 3 Number of statistics: 5 Number of rotations around each axis: 3	$3 \times 3 \times 5 \times 3 = 135$
TOLDI	15	Number of projection planes: 3 Number of partition bins: 20	$3 \times 20 \times 20 = 1200$
QLCI	15	Number of projection planes: 5 Number of partition bins: 19 Gaussian parameter: 0.5	$5 \times 19 \times 19 = 1805$

Note: SI = spin images; FPFH = fast point feature histograms; RoPS = rotational projection statistics; TOLDI = triple orthogonal local depth images; QLCI = quintuple local coordinate images.

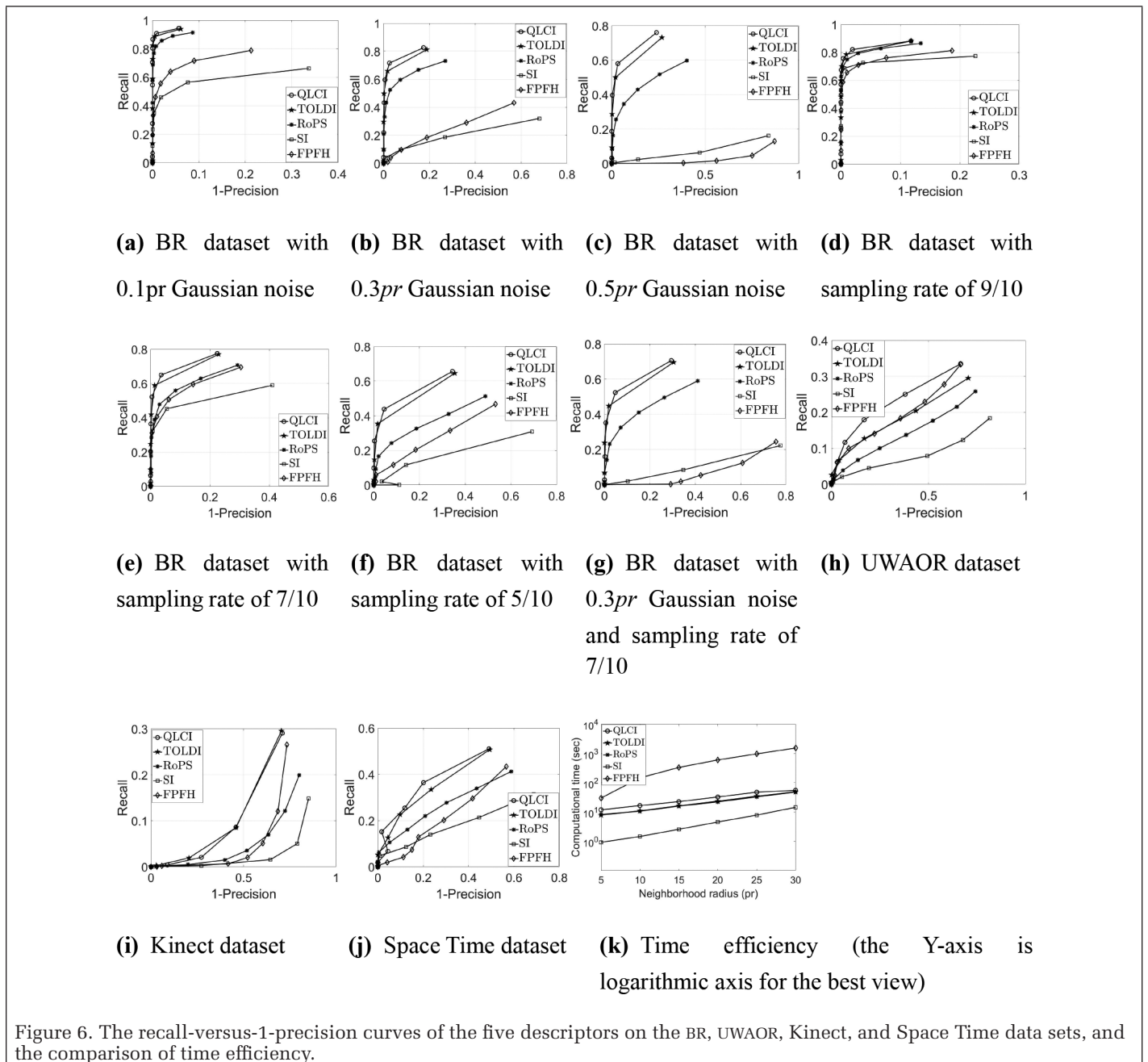


Figure 6. The recall-versus-1-precision curves of the five descriptors on the BR, UWAOR, Kinect, and Space Time data sets, and the comparison of time efficiency.

exhibits good performance on the UWAOR data set but poor performance on the Kinect and Space Time data sets. This is because the normal characteristics used in the FPFH descriptor are susceptible to noise and outliers, where the Kinect data set is noisy and the Space Time data set is affected by outliers.

At least three explanations can be given for the high descriptiveness and strong robustness of our QLCI descriptor. First, the local information is encoded from five views. In particular, we encode the local shape from the positive and negative directions of the x-axis and the positive and negative directions of the y-axis, which reduces the effect of self-occlusion. Thus, more geometric and spatial information is characterized in the descriptor. Second, the local coordinate feature is equivalent to the local depth feature, so it can better encode the neighborhood information around the key point and reduce loss of information in the process of going from 3D to 2D or 1D representations. Third, the 2D projection planes are sparsely divided into many bins, and only the maximum or

minimum local coordinate value is treated as the bin value. Thus, the effect of noise and point-density variation is faint, boosting the stability of the QLCI descriptor.

The time-efficiency performance is illustrated in Figure 6k, tested on the “Armadillo” model of the BR data set. The time required for calculating the descriptors of 1000 key points is recorded. The FPFH descriptor has a high computation complexity, and SI is computationally the fastest. However, the SI descriptor has pretty poor descriptor matching performance. Our descriptor is slightly more time consuming than TOLDI and RoPS. In comparison with local depth, the local coordinate is computationally cheaper, but our descriptor needs to calculate five LCIs. Therefore, it needs more time than TOLDI. Yang *et al.* (2017c) proved the RoPS descriptor to be computationally more expensive than the FPFH descriptor. This is because the original LRF method of RoPS is time consuming. However, in this article our LRF method is applied, so RoPS also exhibits high computational efficiency. Overall,

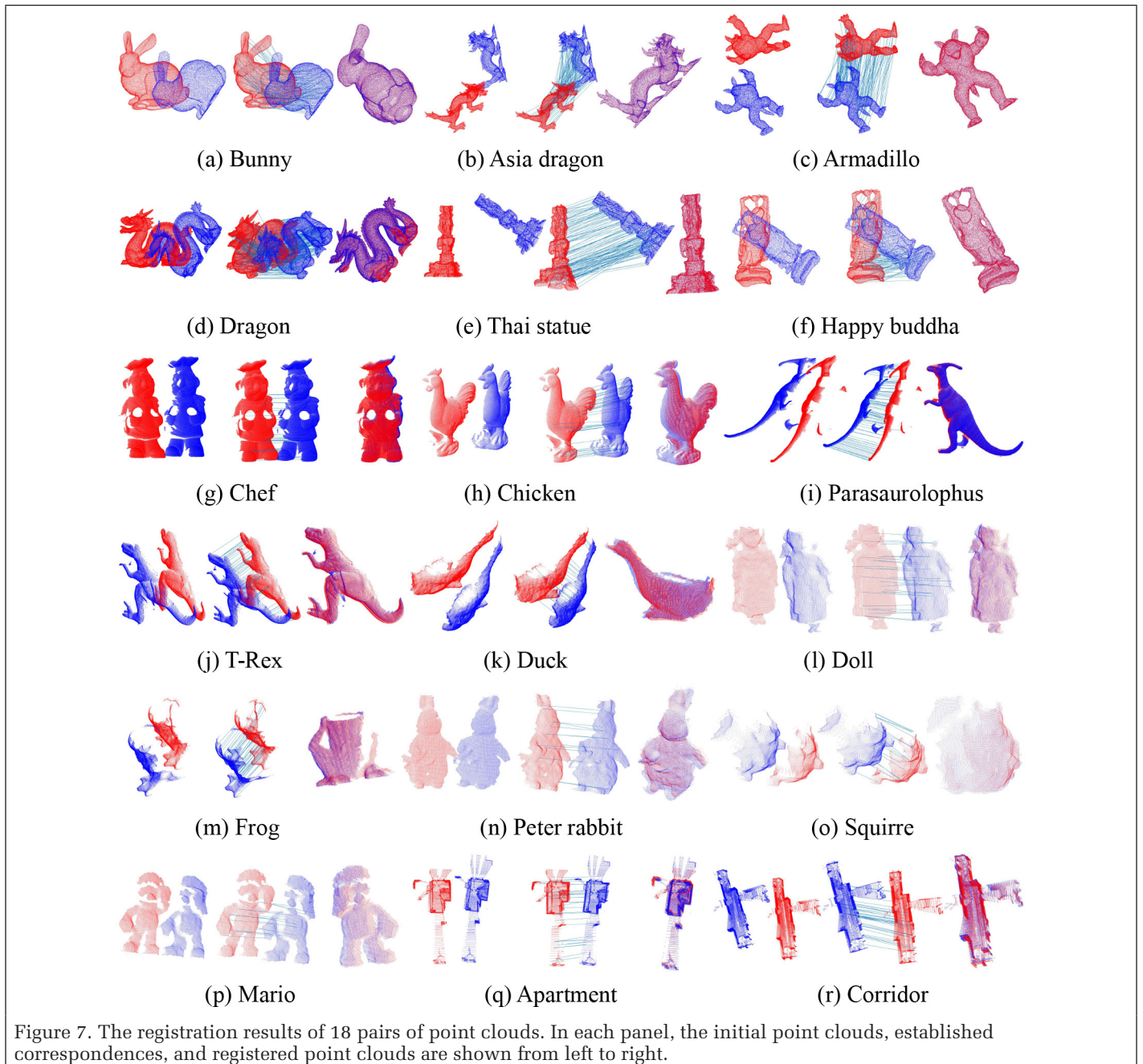


Figure 7. The registration results of 18 pairs of point clouds. In each panel, the initial point clouds, established correspondences, and registered point clouds are shown from left to right.

our descriptor is better than RoPS (based on the original LRF method) and PPFH in terms of time efficiency. In comparison with TOLDI, our descriptor is slightly more time consuming but more descriptive.

### Application to Point-Cloud Registration

In order to represent a complete object, the point clouds from different views need to be aligned into a common coordinate system. The LSD can be used to perform the coarse registration, and then the iterative closest point algorithm (Besl and McKay 1992) and its variants (Grant, Bethel and Crawford 2012; Tao *et al.* 2018) can be applied to implement the fine registration. In this application scenario, missing border regions (i.e., partial overlap) are the main nuisance. In this experiment, in addition to the BR data set (Figure 7a–f) we use the UWA3M dataset (Figure 7g–j; Mian *et al.* 2006b), the Kinect registration data set (Figure 7k–p; Tombari *et al.* 2010b), and the point clouds of buildings (Figure 7q–r; Pomerleau *et al.* 2012). The aim is to make our experiments cover a wide variety of objects. These objects exhibit different geometric properties. For example, the point clouds of the Apartment and Corridor mainly contain line and plane features, whereas the point clouds of other objects (the Bunny, Chicken, and Mario) mainly contain free-form surfaces. These data were also acquired by different devices, such as a lidar scanner and Kinect, creating different data modalities.

The registration pipeline is as follows. The key points are first extracted from the model and scene point clouds by the intrinsic shape signatures detector (Zhong 2009). Then the QLCI descriptor is calculated on each key point. Each model descriptor is matched with all the scene descriptors to find the  $\kappa$  (in this article,  $\kappa = 5$ ) nearest descriptors, and the key point associated with the model descriptor is paired with the key points associated with the  $\kappa$  scene descriptors. Thus, the point-to-point correspondences are established. Eventually, the random sample consensus algorithm (Fischler and Bolles 1981) is used to eliminate incorrect correspondences and calculate the rigid transformation. The number of trials is uniformly set to 1000, though only the Kinect registration data set needs so many trials (due to its low quality). The registration results are presented in Figure 7.

From the registration results, we can see that all the point-cloud pairs are automatically and well registered based on our QLCI descriptor. Even for the Kinect registration data set, the results are enough to provide a good initial pose for the fine registration, though only a few correspondences are established. On the data with poor shape geometry (the Apartment and Corridor), the two point clouds of each object are also well aligned together.

### Conclusion and Outlook

In this article, an LRF method is proposed, based on the covariance matrix, with which an LSD was formulated. The Gaussian function is introduced to determine weights for the points in the neighborhood. Balanced robustness to noise and shape incompleteness is obtained by setting a proper Gaussian parameter. Another weighting strategy is used to decrease the effect of point-density variation. A vector representation is calculated to remove the sign ambiguity of the x-axis, which enhances robustness to shape incompleteness. In the feature representation of our descriptor, the LCIs are calculated from five views. This leads to encoding more information. In each LCI, the local coordinates are selected to calculate the pixel values. Thus, the majority of the local shape information is preserved.

Experiments were performed to validate the performance of the LRF method and LSD. As shown in the experiments, the proposed LRF method possesses high robustness to noise and

point-density variation, and absorbs the robustness to shape incompleteness. The LSD's descriptiveness and robustness are demonstrated as well. Additionally, both the LRF method and the descriptor exhibit good computational efficiency.

A drawback of our descriptor is that its dimensionality is too high. In the future, we plan to find a method to reduce the dimensionality or formulate a binary version, creating a more compact descriptor. This will help to reduce the memory footprint and the computational time of the descriptor matching phase.

### Acknowledgments

The authors would like to acknowledge the Stanford 3D Scanning Repository, the University of Western Australia, the Computer Vision Lab in the University of Bologna, and the Autonomous Systems Lab of the Institute of Robotics and Intelligent Systems at the Eidgenössische Technische Hochschule Zürich for publishing their data sets on the Internet. This work was partly supported by the National Natural Science Foundation of China (.Nos. 41674005 and 41374011) and partly supported by the China Scholarship Council Scholarship (No. 201906270179).

### References

- Akizuki, S. and M. Hashimoto. 2015. DPN-LRF: A local reference frame for robustly handling density differences and partial occlusions. Pages 878–887 in ISVC 2015: Advances in Visual Computing, held in Las Vegas, Nev., 14–16 December 2015. Edited by G. Bebis, R. Boyle, B. Parvin, D. Koracin, I. Pavlidis, R. Feris, T. McGraw, M. Elendt, R. Kopper, E. Ragan, Z. Ye and G. Weber. *Lecture Notes in Computer Science* vol. 9474. Cham, Switzerland: Springer.
- Aldoma, A., Z.-C. Marton, F. Tombari, W. Wohlkinger, C. Potthast, B. Zeisl, R. B. Rusu, S. Gedikli and M. Vincze. 2012. Tutorial: Point Cloud Library: three-dimensional object recognition and 6 DOF pose estimation. *IEEE Robotics & Automation Magazine* 19 (3):80–91.
- Besl, P. J. and N. D. McKay. 1992. A method for registration of 3-D shapes. *IEEE Transactions on Pattern Analysis and Machine Intelligence* 14 (2):239–256.
- Chen, H. and B. Bhanu. 2007. 3D free-form object recognition in range images using local surface patches. *Pattern Recognition Letters* 28 (10):1252–1262.
- Darom, T. and Y. Keller. 2012. Scale-invariant features for 3-D mesh models. *IEEE Transactions on Image Processing* 21 (5):2758–2769.
- Dong, Z., B. Yang, F. Liang, R. Huang and S. Scherer. 2018. Hierarchical registration of unordered TLS point clouds based on binary shape context descriptor. *ISPRS Journal of Photogrammetry and Remote Sensing* 144:61–79.
- Dong, Z., B. Yang, Y. Liu, F. Liang, B. Li and Y. Zang. 2017. A novel binary shape context for 3D local surface description. *ISPRS Journal of Photogrammetry and Remote Sensing* 130:431–452.
- Fischler, M. A. and R. C. Bolles. 1981. Random Sample Consensus: A paradigm for model fitting with applications to image analysis and automated cartography. *Communications of the ACM* 24 (6):381–395.
- Flint, A., A. Dick and A. van den Hengel. 2008. Local 3D structure recognition in range images. *IET Computer Vision* 2 (4):208–217.
- Frome, A., D. Huber, R. Kolluri, T. Bülow and J. Malik. 2004. Recognizing objects in range data using regional point descriptors. Pages 224–237 in Computer Vision—ECCV 2004, held in Prague, Czech Republic, 11–14 May 2004. Edited by T. Pajdla and J. Matas. *Lecture Notes in Computer Science* vol. 3023. Berlin: Springer.
- Grant, D., J. Bethel and M. Crawford. 2012. Point-to-plane registration of terrestrial laser scans. *ISPRS Journal of Photogrammetry and Remote Sensing* 72:16–26.

- Guo, Y., M. Bennamoun, F. Sohel, M. Lu, J. Wan and N. M. Kwok. 2016. A comprehensive performance evaluation of 3D local feature descriptors. *International Journal of Computer Vision* 116:66–89.
- Guo, Y., F. Sohel, M. Bennamoun, M. Lu and J. Wan. 2013. Rotational projection statistics for 3D local surface description and object recognition. *International Journal of Computer Vision* 105:63–86.
- Guo, Y., F. Sohel, M. Bennamoun, J. Wan and M. Lu. 2014. An accurate and robust range image registration algorithm for 3D object modeling. *IEEE Transactions on Multimedia* 16 (5):1377–1390.
- Guo, Y., F. Sohel, M. Bennamoun, J. Wan and M. Lu. 2015. A novel local surface feature for 3D object recognition under clutter and occlusion. *Information Science* 293:196–213.
- Johnson, A. E. and M. Hebert. 1998. Surface matching for object recognition in complex three-dimensional scenes. *Image and Vision Computing* 16:635–651.
- Johnson, A. E. and M. Hebert. 1999. Using spin images for efficient object recognition in cluttered 3D scenes. *IEEE Transactions on Pattern Analysis and Machine Intelligence* 21 (5):433–449.
- Knopp, J., M. Prasad, G. Willems, R. Timofte and L. Van Gool. 2010. Hough transform and 3D SURF for robust three dimensional classification. Pages 589–602 in *Computer Vision—ECCV 2010*, held in Heraklion, Greece, 5–11 September 2010. Edited by K. Daniilidis, P. Maragos and N. Paragios. Lecture Notes in Computer Science vol. 6313. Berlin: Springer.
- Levin, D. 2004. Mesh-independent surface interpolation. In *Geometric Modeling for Scientific Visualization*, edited by G. Brunnett, B. Hamann, H. Müller and L. Linsen, 37–49. Berlin: Springer.
- Malassiotis, S. and M. G. Strintzis. 2007. Snapshots: A novel local surface descriptor and matching algorithm for robust 3D surface alignment. *IEEE Transactions on Pattern Analysis and Machine Intelligence* 29 (7):1285–1290.
- Mian, A. S., M. Bennamoun and R. A. Owens. 2006a. A novel representation and feature matching algorithm for automatic pairwise registration of range images. *International Journal of Computer Vision* 66:19–40.
- Mian, A. S., M. Bennamoun and R. Owens. 2006b. Three-dimensional model-based object recognition and segmentation in cluttered scenes. *IEEE Transactions on Pattern Analysis and Machine Intelligence* 28 (10):1584–1601.
- Mian, A., M. Bennamoun and R. Owens. 2010. On the repeatability and quality of keypoints for local feature-based 3D object retrieval from cluttered scenes. *International Journal of Computer Vision* 89:348–361.
- Petrelli, A. and L. Di Stefano, 2011. On the repeatability of the local reference frame for partial shape matching. Pages 2244–2251 in *2011 International Conference on Computer Vision*, held in Barcelona, Spain, 6–13 November 2011. Edited by J. Editor. Location: Institute of Electrical and Electronics Engineers.
- Petrelli, A. and L. Di Stefano. 2012. A repeatable and efficient canonical reference for surface matching. Pages 403–410 in *2012 Second International Conference on 3D Imaging, Modeling, Processing, Visualization & Transmission*, held in Zurich, Switzerland, 13–15 October 2012. Edited by J. Editor. Location: Institute of Electrical and Electronics Engineers.
- Pomerleau, F., M. Liu, F. Colas and R. Siegwart. 2012. Challenging data sets for point cloud registration algorithms. *The International Journal of Robotics Research* 31 (14):1705–1711.
- Rusu, R. B., N. Blodow and M. Beetz, 2009. Fast Point Feature Histograms (FPFH) for 3D registration. Pages 3212–3217 in *2009 IEEE International Conference on Robotics and Automation*, held in Kobe, Japan, 12–17 May 2009. Edited by J. Editor. Location: Institute of Electrical and Electronics Engineers.
- Rusu, R. B., Z. C. Marton, N. Blodow and M. Beetz. 2008. Persistent point feature histograms for 3D point clouds. Pages 119–128 in *Intelligent Autonomous Systems 10: IAS-10*, held in Baden Baden, Germany, DD–DD Month YYYY. Edited by W. Burgard, R. Dillmann, C. Plagemann and N. Vahrenkamp. Amsterdam: IOS Press.
- Sukno, F. M., J. L. Waddington and P. F. Whelan. 2013. Rotationally invariant 3D shape contexts using asymmetry patterns. Pages 7–17 in *Proceedings of the International Conference on Computer Graphics Theory and Applications and International Conference on Information Visualization Theory and Applications*, held in Barcelona, Spain, 21–24 February 2013. Edited by S. Coquillart, C. Andujar, J. Braz, R. S. Laramee and A. Kerren. Setúbal, Portugal: Science and Technology Publications.
- Sun, Y. and M. Abidi. 2001. Surface matching by 3D point's fingerprint. Pages 263–269 in *Proceedings Eighth IEEE International Conference on Computer Vision*, held in Vancouver, Canada, 7–14 July 2001. Edited by B. Buxton and R. Cipolla. Piscataway, N.J.: Institute of Electrical and Electronics Engineers.
- Tao, W., X. Hua, K. Yu, X. He and X. Chen. 2018. An improved point-to-plane registration method for terrestrial laser scanning data. *IEEE Access* 6:48062–48073.
- Tombari, F., S. Salti, and L. Di Stefano. 2010a. Unique shape context for 3D data description. Pages 57–62 in *Proceedings of the ACM Workshop on 3D Object Retrieval*, held in Firenze, Italy, 25 October 2010. Edited by J. Editor. New York: Association for Computing Machinery.
- Tombari, F., S. Salti and L. Di Stefano. 2010b. Unique signatures of histograms for local surface description. Pages 356–369 in *Computer Vision—ECCV 2010*, held in Heraklion, Greece, 5–11 September 2010. Edited by K. Daniilidis, P. Maragos and N. Paragios. Lecture Notes in Computer Science vol. 6313. Berlin: Springer.
- Tombari, F., S. Salti and L. Di Stefano. 2013. Performance evaluation of 3D keypoint detectors. *International Journal of Computer Vision* 102:198–220.
- Tong, C. H. and T. D. Barfoot. 2013. Gaussian Process Gauss-Newton for 3D laser-based visual odometry. Pages 5204–5211 in *2013 IEEE International Conference on Robotics and Automation*, held in Karlsruhe, Germany, 6–10 May 2013. Edited by J. Editor. Location: Institute of Electrical and Electronics Engineers.
- Yang, J., Z. Cao and Q. Zhang. 2016. A fast and robust local descriptor for 3D point cloud registration. *Information Sciences* 346–347:163–179.
- Yang, J., Y. Xiao and Z. Cao. 2018. Toward the repeatability and robustness of the local reference frame for 3D shape matching: An evaluation. *IEEE Transactions on Image Processing* 27 (8):3766–3781.
- Yang, J., Y. Xiao and Z. Cao. 2019. Aligning 2.5D scene fragments with distinctive local geometric features and voting-based correspondences. *IEEE Transactions on Circuits and Systems for Video Technology* 29 (3):714–729.
- Yang, J., Q. Zhang and Z. Cao. 2017a. Multi-attribute statistics histograms for accurate and robust pairwise registration of range images. *Neurocomputing* 251:54–67.
- Yang, J., Q. Zhang and Z. Cao. 2017b. The effect of spatial information characterization on 3D local feature descriptors: A quantitative evaluation. *Pattern Recognition* 66:375–391.
- Yang, J., Q. Zhang, Y. Xiao and Z. Cao. 2017c. TOLDI: An effective and robust approach for 3D local shape description. *Pattern Recognition* 65:175–187.
- Zhang, J. and S. Singh. 2014. LOAM: Lidar odometry and mapping in real-time. Pages 109–111 in *Robotics: Science and Systems X*, held in Berkeley, Calif., 12–16 July 2014. Edited by D. Fox, L. E. Kavradi and H. Kurniawati. Location: Publisher.
- Zhong, Y. 2009. Intrinsic shape signatures: A shape descriptor for 3D object recognition. Pages 689–696 in *2009 IEEE 12th International Conference on Computer Vision Workshops*, held in Kyoto, Japan, 27 September–4 October 2009. Edited by J. Editor. Location: Institute of Electrical and Electronics Engineers.

# ASPRS BOOKSTORE

visit [asprs.org](http://asprs.org)

available at  
**amazon**

## Digital Elevation Model Technologies & Applications, 3rd Ed

Co-Editors: David F. Maune, PhD, CP, CFM, PSM, PS, GS, SP and Amar Nayegandhi, CP, CMS-Remote Sensing  
**List Price:** \$100 | **ASPRS Members:** \$80  
**ASPRS Student Members:** \$50<sup>†</sup>  
*Also available for Amazon Kindle*  
**Amazon Kindle Price\*\*:** \$85

## Landsat's Enduring Legacy: Pioneering Global Land Observations From Space

Landsat Legacy Project Team  
ISBN: ISBN 1-57083-101-7 · Hardcover · 586 pages · 2017 · Stock #4958  
**List Price:** \$95 | **ASPRS Members:** \$65  
**Student Members:** \$60  
**Amazon Price\*:** \$100

## Manual of Airborne Topographic Lidar

Editor: Michael S. Renslow  
ISBN: 1-57083-097-5 · Hardcover · 528 pages · 2012 · Stock #4587  
**List Price:** \$150 | **ASPRS Members:** \$95  
**Student Members:** \$75  
**Amazon Price (hardcover)\*:** \$135  
*Also available for Amazon Kindle*  
**AmazonKindle Price\*\*:** \$110

## Manual of Photogrammetry, Sixth Edition

Editor: J. Chris McGlone  
ISBN: 1-57083-099-1 · Hardcover · 1372 pages · 2013 · Stock #4737  
**List Price:** \$175 | **ASPRS Members:** \$125  
**Student Members:** \$98  
**Amazon Price\*:** \$175

## Glossary of the Mapping Sciences

Co-published by ASPRS, ACSM and ASCE  
ISBN: 1-57083-011-8  
563 pp · Paperback · 1994 · Stock #5021  
**List Price:** \$50 | **ASPRS Members:** \$35  
**Student Members:** \$25 | **Amazon Price\*:** \$50

## Hyperspectral Remote Sensing for Forestry

Paul Treitz, Valerie Thomas, Pablo J. Zarco-Tejada, Peng Gong, and Paul J. Curran  
ISBN: 1-57083-093-2  
107 pp · Softcover · 2010 · Stock #4584  
**List Price:** \$26 | **ASPRS Members:** \$21  
**Student Member:** \$21 | **Amazon Price\*:** \$26

## Manual of Geographic Information Systems

Editor: Marguerite Madden, PhD  
Foreword: Jack Dangermond, Esri  
ISBN: 1-57083-086-X · Hardcover · 1352 pages + DVD · July 2009 · Stock #4650  
**List Price:** \$53 | **ASPRS Members:** \$40  
**Student Members:** \$40  
**Amazon Price\*:** \$55

## Meeting Environmental Challenges with Remote Sensing Imagery

Editors: Rebecca Dodge & Russ Congalton  
Published by American Geosciences Institute; Publishing Partners: AmericaView, USGS Land Remote Sensing Program, ASPRS  
ISBN: 978-0-922152-94-0 · 82 pp · Softcover · 2013 · Stock #4589  
**List Price:** \$7.50 | **ASPRS Members:** \$6  
**Bulk Orders (3 or more copies):** \$4.50 each  
**Amazon Price\*:** \$9.95

## MANUAL OF REMOTE SENSING, 3<sup>RD</sup> EDITION (A SERIES)

### Earth Observing Platforms & Sensors

Volume 1.1  
Volume Editor: Mark Jackson  
ISBN: 1-57083-089-4  
550 pp · Hardcover · 2009 · Stock #4582  
**List Price:** \$95 | **ASPRS Members:** \$75  
**Student Members:** \$55 | **Amazon Price\*:** \$95

### Remote Sensing of Human Settlements

Volume 5  
Editor-in-Chief: Andrew B. Rencz  
Volume Editors: Merril K. Ridd & James D. Hipple  
ISBN: 1-57083-077-0  
747+ pp · Hardcover · 2005 · Stock # 4576  
**List Price:** \$99 | **ASPRS Members:** \$80  
**Student Members:** \$60  
**Amazon Price\*:** \$69.99

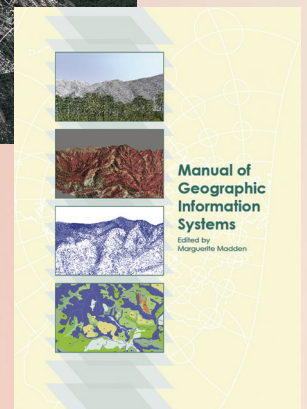
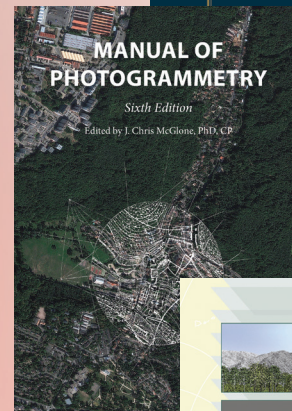
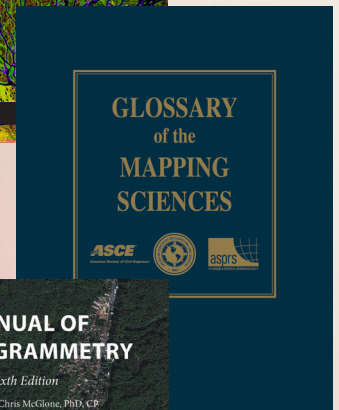
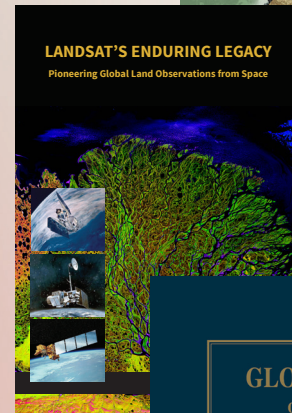
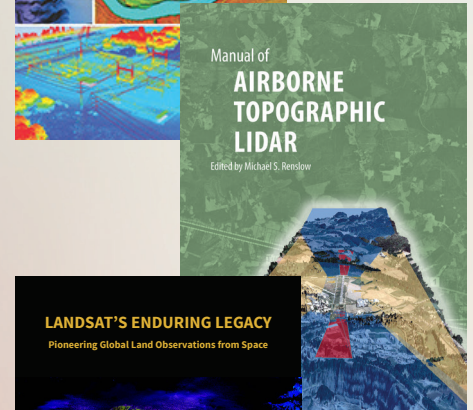
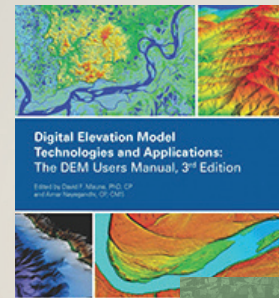
### Remote Sensing of the Marine Environment

Volume 6  
Editor-in-Chief: Andrew B. Rencz  
Volume Editor: James F.R. Gower  
ISBN: 1-57083-080-0 · 360 pp · Hardcover · 2006 · Stock # 4578  
**List Price:** \$95 | **ASPRS Members:** \$75  
**Student Members:** \$50 | **Amazon Price\*:** \$95

\*Member discounts are not available when ordering directly from Amazon.

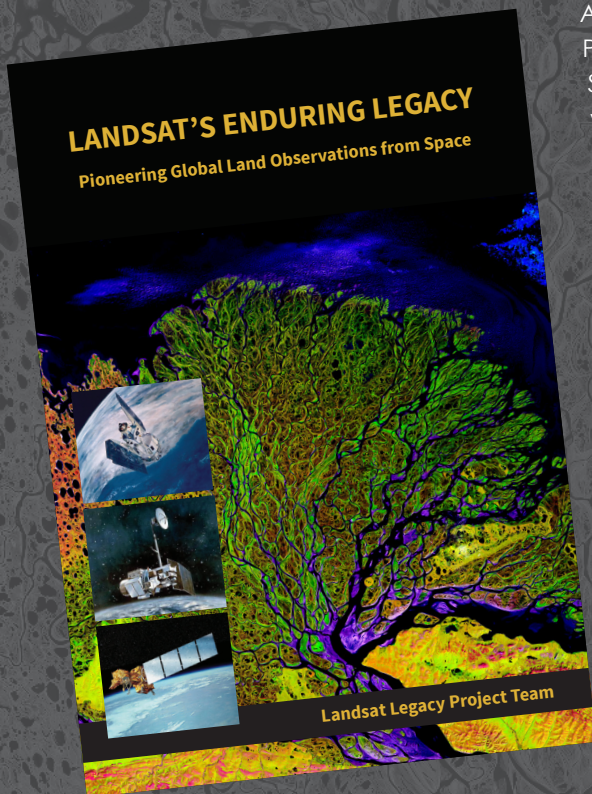
\*\*Member discounts are not available on Amazon Kindle e-books,

<sup>†</sup>Students must order via the ASPRS Bookstore & a copy of your valid student ID must be submitted to be eligible for student pricing.



# LANDSAT'S ENDURING LEGACY

PIONEERING GLOBAL LAND OBSERVATIONS FROM SPACE



After more than 15 years of research and writing, the Landsat Legacy Project Team is about to publish, in collaboration with the American Society for Photogrammetry and Remote Sensing (ASPRS), a seminal work on the nearly half-century of monitoring the Earth's lands with Landsat. Born of technologies that evolved from the Second World War, Landsat not only pioneered global land monitoring but in the process drove innovation in digital imaging technologies and encouraged development of global imagery archives. Access to this imagery led to early breakthroughs in natural resources assessments, particularly for agriculture, forestry, and geology. The technical Landsat remote sensing revolution was not simple or straightforward. Early conflicts between civilian and defense satellite remote sensing users gave way to disagreements over whether the Landsat system should be a public service or a private enterprise. The failed attempts to privatize Landsat nearly led to its demise. Only the combined engagement of civilian and defense organizations ultimately saved this pioneer satellite land monitoring program. With the emergence of 21st century Earth system science research, the full value of the Landsat concept and its continuous 45-year global archive has been recognized and embraced. Discussion of Landsat's future continues but its heritage will not be forgotten.

The pioneering satellite system's vital history is captured in this notable volume on Landsat's Enduring Legacy.

## Landsat Legacy Project Team

Samuel N. Goward  
Darrel L. Williams  
Terry Arvidson  
Laura E. P. Rocchio  
James R. Irons  
Carol A. Russell  
Shaïda S. Johnston

## Landsat's Enduring Legacy

Hardback, 2017, ISBN 1-57083-101-7  
Student \$60\*  
Member \$80\*  
Non-member \$100\*

\* Plus shipping

Order online at  
[www.asprs.org/landsat](http://www.asprs.org/landsat)